METHOD TO PREDICT ROTOR OUTPUTS OF VAWT CLUSTER BY USING WAKE MODEL MIMICKING THE CFD-CREATED FLOW FIELD

（数値流体力学解析(CFD)により生成された流れ場を模擬する後流モデルを用いた垂直軸風車群のロータ出力を予測する方法）

JIRAROTE BURANAROTE

(D18T1105K)

DEPARTMENT OF MECHANICAL AND AEROSPACE ENGINEERING

TOTTORI UNIVERSITY

2022

Table of Contents

List of Figures

List of Tables

Nomenclature

$C1_{\mathrm{fg\_}i}$ = Fitting parameter in f_{G} , [$i = 1$ to 4]

$C2_{\mathrm{fg\_}i}$ = Fitting parameter in f_{G} , [$i = 1$ to 4]

$C3_{\mathrm{fg\_}i}$ = Fitting parameter in f_{G} , [$i = 1$ to 4]

$C1_{\mathrm{fr\_}i}$ = Fitting parameter in f_{R} , [$i = 1$ to 4]

$C2_{\mathrm{fr\_}i}$ = Fitting parameter in f_{R} , [$i = 1$ to 4]

$C3_{\mathrm{fr\_}i}$ = Fitting parameter in f_{R} , [$i = 1$ to 4]

C_{N0} = Fitting parameter in f_{COR}

C_{N1} = Fitting parameter in f_{COR}

C_{N2} = Fitting parameter in f_{COR}

C_{N3} = Fitting parameter in f_{COR}

C_{P0} = Fitting parameter in f_{COR}

C_{P1} = Fitting parameter in f_{COR}

C_{P2} = Fitting parameter in f_{COR}

C_{P3} = Fitting parameter in f_{COR}

CV = Control volume

C_w = f_{USG} coefficient

d_j = Distance between the center of the *j*-th rotor and the stream-wise center line through the *k*-th rotor

du = Velocity deficit function

dv = Correction function in the perpendicular to the mainstream direction

dx = Small boundary element in *x*-direction

dy = Small boundary element in *y*-direction

d_{w} = wake expansion

D = Diameter of rotor, m

f_{COR} = Correction function in the mainstream direction

f_{G} = Gaussian-type function

F_{net_x} = Total force in CV

Fp = Pressure force

gap = Space between the edge of the rotor

f_{p} = Fitting parameter in f_{SG}

f_p = Correction function of Fp

f_{R} = Resonance-type function

f_{SG} = Super-Gaussian function

f_{USG} = Ultra-super-Gaussian function

I = Interaction function

k_{w} = Wake expansion coefficient (fitting parameter)

$\dot{m}$ = Mass flowrate

N = Number of rotor

N_{int} = Number of rotor in circular region

P = Power, mW

p = Pressure, Pa

$p(x_{\mathrm{n}})$ = Function in f_{SG}

Q = Torque, mN

R_{int} = Circular region of the radius around a rotor (k)

r = Distance from the rotor center, m

t = Time, s

u = Velocity component in the mainstream direction (x), m/s

$\boldsymbol{u}$ = Velocity vector

u_{ind} = Induced velocity in the mainstream direction (x), m/s

U_{∞} = Uniform upstream velocity, m/s

v = Velocity component in the perpendicular to the mainstream direction (y), m/s

v_{ind} = Induced velocity in the perpendicular to the mainstream direction (y), m/s

W = Complex velocity potential

x = Coordinate in the mainstream direction

x_k = Center coordinate of the main rotor in the mainstream direction

x_{n} = normalized relative coordinate in the perpendicular to the mainstream direction, $x_{\mathrm{n}} = (x - x_k)/D$

y = Coordinate in the perpendicular to the mainstream direction

y_k = Center coordinate of the main rotor in the perpendicular to the mainstream direction

y_{n} = Normalized relative coordinate in the perpendicular to the mainstream direction, $y_{\mathrm{n}} = (y - y_k)/D$

$y_{\mathrm{n}\delta}$ = Normalized relative coordinate with wake shift, $y_{\mathrm{n}\delta} = \frac{y - y_k - \delta}{D}$

Greek Symbols

Γ = Circulation, m^2/s

μ = Dipole (blockage) of the rotor, m^3/s

μ_{ref} = Reference value of the blockage effect of the rotor, m^3/s

δ = Wake shift, m

ν = Kinematic viscosity, m^2/s

ρ = Density, kg/m^3

β_1 = Wake shift factor 1

β_2 = Wake shift factor 2

β_3 = Wake width factor

β_3 = Wake width factor

ω = Angular velocity (rad/s)

φ = Rotor angle (degree)

α = The variable to define the wake width which consists of the effect of u_{ind}

α_1 = Interaction function factor for CO layout (fitting parameter)

α_2 = Interaction function factor for CD layout (fitting parameter)

α_3 = Interaction function factor for CU layout (fitting parameter)

α_4 = Interaction function factor for TD layout (fitting parameter)

γ_1 = Wake angle (degree)

γ_2 = Angle to divided searching range

θ = Wind direction (degree)

ϕ = Induced velocity angle (degree)

Subscripts

ep = Evaluation position

int = Interaction region

j = Index of the counterpart rotor

k = Index of the main rotor

p = Potential flow

ref = Reference

SI = Single rotor

w = Wake flow

Chapter 1

Introduction

1.1 Background

Wind energy is a natural energy. Humans have, from a long time ago, been utilizing wind energy to sail ships to transport goods or to rotate windmills for milling or to irrigate lands. Nowadays, wind energy is being used to generate electricity. Wind power generation is one of the most prolific renewable energies, which needs no fossil fuel. In other words, wind power is a clean energy with no carbon dioxide emission and it has almost no pollution causing to the environment [1]. Due to the cost reduction by technology development, wind energy has become the main power supply in the world. To realize carbon neutrality, a large amount of renewable energy is expected to be introduced [2, 3]. Therefore, wind power generators are becoming increasingly larger in size, and their application to offshore generation is increasing [4, 5]. However, the efficiency of a wind farm can be reduced owing to the wake effects [6–8]. One of the challenges in the wind power sector is to evaluate the influence of the wakes to improve the efficiency of a wind farm [9–15]. Additionally, to maximize the power output from a wind farm, it is necessary to deploy wind turbines with the optimal layout for the wind condition of the planned site [16–20]. The wake control methods using the blade's pitch [21] or the yaw [22, 23] of the horizontal-axis wind turbines (HAWTs) were studied to optimize the wind farm.

The wake effects can be modeled by studying the characteristics of the flow behind the rotor. One of the physical phenomena of the wake is the momentum (or velocity) deficit, which causes a reduction in the power output of the downstream rotors [11]. Shapiro et al. [24] proposed a wake model, which can reproduce the output of wind farms consisting of HAWTs, by linking the wake expansion rate to a top-down model [9] and by using a super-Gaussian wake profile that can smoothly transition from a top-hat shape to a Gaussian shape. Yuan et al. [25] recently proposed a wake model for a vertical-axis wind turbine (VAWT) array by combining two semi-Gaussian functions with different deviations. This model can better reflect the asymmetric characteristic of the VAWT wakes.

According to the studies by Whittlesey et al. [26] and Dabiri [27], the output per unit land area of a wind farm consisting of small-size VAWTs with a high aspect ratio (rotor height/diameter), which are closely arranged using a unit of counter-rotating paired rotors, can be much greater than that of a conventional wind farm consisting of large-size HAWTs, which are deployed with the inter-rotor intervals of several multiples of the rotor diameter (in general, the interval in the dominant wind direction is about 10 times as long as the diameter). Since then, many researchers have been interested in the closely arranged VAWT wind farms and, especially, the interaction effects between two VAWT rotors. For example, Zanforlin and Nishino [28] performed a two-dimensional (2D) computational fluid dynamics (CFD) analysis of a pair of inversely rotating VAWTs to show the greater averaged output than the output of an isolated single VAWT. De Tavernier et al. [29] carried out the 2D-CFD based on the panel vortex method of a closely arranged VAWT pair, each of which had a 10 m rotor radius, to show the effects of the load and rotor spacing on the paired rotor

performance. Bangga et al. [30] proposed two layouts of a VAWT array based on their CFD study of rotor pairs arranged side by side. Sahebzadeh et al. [31] numerically analyzed the output performance of a co-rotating rotor pair by widely changing the rotor spacing and the relative angle to the mainstream. Peng et al. [32] investigated the effects of configuration parameters such as airfoil section, solidity, pitch angle, rotational direction, and turbine spacing on twin VAWTs by CFD analysis. The effects of a three-rotor cluster of VAWTs were also numerically studied by Hezaveh et al. [33] and Silva and Danao [34].

As examples of experimental studies of paired VAWTs, Vergaerde et al. [35] con-ducted the wind tunnel test using two H-type Darrieus rotors (rotor diameter: 0.5 m, rotor height: 0.8 m [36]). Their turbines were placed side-by-side against the main flow and were adequately controlled by DC motors. They observed the power increase up to 16% for the counter-rotating VAWTs and reported the stable synchronized operation of twin rotors. Brownstein et al. [37] examined, by wind tunnel experiments using five-bladed VAWT rotors with the diameter of 0.2 m, the three-dimensional, volumetric mean velocity fields around an isolated single rotor and paired rotors arranged at different angles to the main stream. They reported an average 14% increase in the power of the co-rotating rotors in the 50° wide angle range. Jodai and Hara [38] studied the interaction between two closely spaced VAWTs using miniature 3D printed rotors (diameter: 50 mm, low aspect ratio of 0.87, and high solidity of 0.382) arranged side-by-side. Their experimental results showed a maximum 15% increase in power in the case of the counter-down layout when the inter-rotor space became the shortest (gap space: 10% of the rotor diameter).

Hara et al. [39] applied the dynamic fluid body interaction (DFBI) model to the CFD analysis to simulate the closely arranged paired 2D rotors corresponding to the equator cross-section of the experimental model used in Ref. [38]. Their CFD analysis considered the time-varying rotor speed, for the first time, simulated the synchronization operation of twin rotors and showed the alternation in the angular velocities of two rotors. Furukawa et al. [40] developed an analytical model considering the pressure fluctuation (or increase in flow velocity) observed in the gap region between twin rotors in the above experiments and CFD analyses. The model successfully demonstrated the alternation in the angular velocities of two rotors and showed that the period of the variation in rotor speed depended on the strength of the interaction between the two rotors.

Although the increase in the averaged power of a closely spaced side-by-side VAWT pair is clear, the effects of the distribution of wind direction on the VAWT cluster consisting of many rotors must be investigated more extensively to search for the optimal layout of VAWTs. The CFD analysis, especially the DFBI model simulation, can give reliable results but needed a long calculation time. Although the experiments can also give useful information, the cost is high and the time for preparation is long. If the number of rotors in a target wind farm increases, the simulation by CFD or the experiment using a lot of rotors is non-realistic. Therefore, a method that can simulate precisely and in a short time the flow field of a wind farm, including a large number of VAWTs, is necessary.

1.2 Study Objective and Outline

This study proposed a new method to predict outputs of two-dimensional VAWT rotors by using a wake model mimicking the CFD-created flow field [41]. The method was based on the potential flow and includes the velocity deficit (or wake effects) artificially, like the method by Whittlesey et al. [26]. This study included the modification of the *y*-component (cross-flow) of the flow velocity, although Whittlesey et al. did not consider it. Moreover, in this study, the Biot-Savart law was introduced to consider the effects of the interaction between the rotors on the wake shift and width [42]. The proposed method used the circulation around each rotor to estimate the output of each rotor. The circulation was also used as the input value (or tentative value) for each rotor to calculate the potential flow in a wind farm. The decision on the appropriate flow and rotor conditions was conducted by evaluating the momentum balance, which was calculated using the momentum transports and the pressure forces at the boundaries of the control volume (CV) and thrust forces of rotors. The necessary CFD data, or the available and reliable experimental data, are the power performance of an isolated single VAWT and the averaged flow velocity distribution in the CV, the pressure distributions at the boundaries under several wind speed conditions. In addition, the power output data of closely spaced paired VAWTs in typical four layouts in the case of a specific inter-rotor distance were necessary. The interaction effects were considered by modifying the given pressure loss of the isolated single rotor, according to the relative layout of the selected two rotors and also considered the distance and the induced velocity.

The method will be validated with the CFD results for two or three rotors studied by Hara et al. [39] and Okinaga et al. [43], in which the rotor height was considered so as to correspond to the experimental rotor used in the experimental study by Jodai et al. [38]. The 2D-CFD analysis of an isolated single rotor is explained in this thesis. In this study, the CFD analysis of four-rotor arrays consisting of the same 2D-CFD rotor models is also conducted to evaluate the proposed method. The present method does not include the three-dimensional effects caused by the finite rotor height because the target in the future is a wind farm consisting of small-scale VAWTs of 14 m diameter with a low aspect ratio, which is now under development in a joint research project in Tottori University [44].

One of the final goals of the proceeding project in Tottori University was to provide a cost-effective and relatively short-time method to optimize the layout of VAWTs in an arbitrary wind farm. In this thesis, at the early stage of the project, the possibility to predict a reasonable condition of a VAWT cluster was shown. Therefore, the round robin, which needed a long calculation time when the number of rotors was large, was utilized in the search for adequate conditions. The maximum number of rotors in a VAWT cluster considered in this study was four due to the problem of calculation time. However, if any advanced optimization method is adopted in the next stage, the problem of the computation time would be mitigated. This thesis is divided into five chapters as follows:

Chapter 1, introduction, this chapter aims to introduce the background, the objective, and the outline of this study.

Chapter 2, a method to predict outputs of VAWT cluster, this chapter proposed a wake model used to simulate the flow distribution around the rotors in a VAWT wind farm. At first, the basic idea of the wake model was introduced and then the details of the functions used in the model are described. Next, the method and the procedure of finding parameters of the functions were explained. Then, the interaction model between the rotors in a wind farm was illustrated. After that, a method to find out an adequate combination of circulations of rotors that satisfy the conservation of momentum in the control volume was proposed. After the explanation of the paired rotor layouts, the correction functions of the pressure loss in the CV, which expressed the effects of superposition of the wake of the rotor at issue and that of the counterpart rotor, were introduced. Finally, the procedure to obtain the outputs of each rotor was described.

Chapter 3, CFD analysis, the wake model in this study was designed to mimic the flow field calculated by the computational fluid dynamics (CFD), and the results of CFD for specific arrangements of paired rotors were needed to predict the arbitrary configuration of rotors. In this chapter, the details (the governing equation, boundary conditions, the computational mesh, and so on) of the CFD analysis using the dynamic fluid/body interaction (DFBI) model conducted to prepare the data for the proposed method and to evaluate the results are described at first. Then, the CFD results of the flow field around an isolated single rotor and the circulation were illustrated. After that, the relations between the circulation and the rotor performances were formulated for the basic information of the proposed method.

Chapter 4, results and discussions, the method described in chapter 2 was validated in this section by applying it to several layouts. Firstly, in Section 4.1., the power dependency of the isolated single rotor on the wind speed was confirmed. Then, in Section 4.2., the power dependency of the paired rotors on the 16 wind directions was compared between the present method and the CFD analysis obtained in the previous study [39]. As the more complicated layouts, the power dependency of the three-rotor cluster on the 12 wind directions was investigated in Section 4.3 [43]. Finally, to show the applicability of the proposed method to VAWT wind farms, the power prediction in the four-rotor layouts arranged in a line were tried in Section 4.4 [41].

Finally, in chapter 5, all of the contents in the previous chapter were summarized. Possible improvement areas were also suggested in the form of recommendations.

References

[1] Wang, X.; Zhou, Y.; Tian, J.; Wang, J.; Cui, Y. Wind power consumption research based on green economic indicators. *Energies* 2018, 11, 2829.

[2] Barthelmie, R.J.; Pryor, S.C. Climate change mitigation potential of wind energy. *Climate* 2021, 9, 136.

[3] McKenna, R.; Pfenninger, S.; Heinrichs, H.; Schmidt, J.; Staffell, I.; Bauer, C.; Gruber, K.; Hahmann, N. A.; Jansen, M.; Klingler, M.; Landwehr, N.; Larsén, G. X.; Lilliestam, J.; Pickering, B.; Robinius, M.; Tröndle, T.; Turkovska, O.; Wehrle, S.; Weinand, M. J.; Wohland, J. High-resolution large-scale onshore wind energy assessments: A review of potential definitions, methodologies and future research needs. *Renewable Energy* 2022, 182, 659–684.

[4] Kou, L.; Li, Y.; Zhang, F.; Gong, X.; Hu, Y.; Quande, Y.; Ke, W. Review on monitoring, operation and maintenance of smart offshore wind farms. *Sensors* 2022, 22, 2822.

[5] Chen, J.; Kim, M.-H. Review of recent offshore wind turbine research and optimization methodologies in their design. *J. Mar. Sci. Eng.* 2022, 10, 28.

[6] Vermeer, L.J.; SΦrensen, J.N.; Crespo, A. Wind turbine wake aerodynamics. *Prog. Aerosp. Sci.* 2003, 39, 467–510.

[7] Fleming, P.; Sinner, M.; Young, T.; Lannic, M.; King, J.; Simley, E.; Doekemeijer, B. Experimental results of wake steering using fixed angles. *Wind Energy. Sci.* 2021, 6, 1521–1531.

[8] Porté-Agel, F.; Wu, Y.-T.; Chen, C.-H. A numerical study of the effects of wind direction on turbine wakes and power losses in a large wind farm. *Energies* 2013, 6, 5297–5313.

[9] Jensen, N.O. *A note on wind generator interaction*. Risø National Laboratory: Roskilde, Denmark, 1983.

[10] Niayifar, A.; Porté-Agel, F.; Diaz, A.P. Analytical modeling of wind farms: A new approach for power prediction. *Energies* 2016, 9, 741.

[11] Göçmen, T.; Laan, P.; Réthoré, P.E.; Diaz, A.P. Wind turbine wake models developed at the technical university of Denmark: A review. *J. Renew. Sustain. Energy* 2016, 60, 752–769.

[12] Zhang, Z.; Huang, P.; Sun, H. A novel analytical wake model with a cosine-shaped velocity deficit. *Energies* 2020, 13, 335.

[13] Gao, X.; Li, Y.; Zhao, F.; Sun, H. Comparisons of the accuracy of different wake models in wind farm layout optimization. *Energy Explor. Exploit*. 2020, 38, 1725–1741.

[14] Porté-Agel, F.; Bastankhah, M.; Shamsoddin, S. Wind-turbine and wind-farm flows: A review. *Bound. -Layer Meteorol*. 2020, 174, 1–59.

[15] Vahidi, D.; Porté-Agel, F. A physics-based model for wind turbine wake expansion in the atmospheric boundary layer. *J. Fluid Mech*. 2022, 943, A49.

[16] Mosetti, G.; Poloni, C.; Diviacco, B. Solving the wind farm layout optimization problem using random search algorithm. *J. Wind. Eng. Ind. Aerodyn.* 1994, 51, 105–116.

[17] Feng, J.; Shen, W.Z. Solving the wind farm layout optimization problem using random search algorithm. *Renew. Energy* 2015, 78, 182–192.

[18] Kirchner-Bossi, N.; Porté-Agel, F. Wind farm area shape optimization using newly developed multi-objective evolutionary algorithms. *Energies* 2018, 11, 3268.

[19] Rinker, J. M.; Soto Sagredo, E.; Bergami, L. The Importance of Wake Meandering on

Wind Turbine Fatigue Loads in Wake. *Energies* 2021, 14, 7313.

[20] Liang, Z.; Liu, H. Layout optimization of a modular floating wind farm based on the full-field wake model. *Energies* 2022, 15, 809.

[21] Serrano González, J.; López, B.; Draper, M. Optimal pitch angle strategy for energy maximization in offshore wind farms considering Gaussian wake model. *Energies* 2021, 14, 938.

[22] Munters, W.; Meyers, J. Dynamic strategies for yaw and induction control of wind farms based on large-eddy simulation and optimization. *Energies* 2018, 11, 177.

[23] Qian, G.-W.; Ishihara, T. A new analytical wake model for yawed wind turbines. *Energies* 2018, 11, 665.

[24] Shapiro, C. R.; Starke, G. M.; Meneveau, C.; Gayme, D. F. A wake modeling paradigm for wind farm design and control. *Energies* 2019, 12, 2956.

[25] Yuan, Z.; Sheng, Q.; Sun, K.; Zang, J.; Zhang, X.; Jing, F.; Ji, R. The array optimization of vertical axis wind turbine based on a new asymmetric wake model. *J. Mar. Sci. Eng.* 2021, 9, 820.

[26] Whittlesey, R. W.; Liska S.; Dabiri, J. O. Fish schooling as a basis for vertical axis wind turbine farm design. *Bioinspiration & Biomimetics.* 2010, 174, 1–59.

[27] Dabiri, J. O. Potential order-of-magnitude enhancement of wind farm power density via counter-rotating vertical-axis wind turbine arrays. *Journal of Renewable and Sustainable Energy* 2011, 3, 043104.

[28] Zanforlin, S.; Nishino, T. Fluid dynamic mechanisms of enhanced power generation by closely spaced vertical axis wind turbines. *Renewable Energy* 2016, 99, 1213–1226.

[29] De Tavernier, D.; Ferreira, C.; Li, A.; Paulsen, U. S.; Madsen, H. A. Towards the understanding of vertical-axis wind turbines in double-rotor configuration. *Journal of Physics*: Conf. Series 2018, 1037, 022015.

[30] Bangga, G.; Lutz, T.; Krämer, E. Energy assessment of two vertical axis wind turbines in side-by-side arrangement. *J. Renew. Sustain. Energy* 2018, 10, 033303.

[31] Sahebzadeh, S.; Rezaeiha, A.; Montazeri, H. Impact of relative spacing of two adjacent vertical axis wind turbines on their aerodynamics. *J. Phys*. 2020, 1618, 042002.

[32] Peng, H. Y.; Han, Z. D.; Liu, H. J.; Lin, K.; Lam, H. F. Assessment and optimization of the power performance of twin vertical axis wind turbines via numerical simulations, *Renewable Energy* 2020, 147, 43-54.

[33] Hezaveh, S. H.; Bou-Zeid, E.; Dabiri, J.; Kinzel, M.; Cortina, G.; Martinelli, L. Increasing the power production of vertical-axis wind-turbine farms using synergistic clustering. *Boundary-Layer Meteorol* 2018, 169, 275–296.

[34] Silva, J. E.; Danao, L. A. M. Varying VAWT cluster configuration and the effect on individual rotor and overall cluster performance. *Energies* 2021, 14, 1567.

[35] Vergaerde, A.; De Troyer, T.; Standaert, L.; Kluczewska-Bordier, J.; Pitance, D.; Immas, A.; Silvert, F.; Runacres, M.C. Experimental validation of the power enhancement of a pair of vertical-axis wind turbines, *Renewable Energy* 2020, 146, 181–187.

[36] Vergaerde, A.; De Troyer, T.; Molina, A. C.; Standaert, L.; Runacres, M. C. Design, manufacturing and validation of a vertical-axis wind turbine setup for wind tunnel tests, *Journal of Wind Engineering and Industrial Aerodynamics* 2019, 193, 103949.

[37] Brownstein, I. D.; Wei N. J.; Dabiri, J. O. Aerodynamically interacting vertical-axis

wind turbines: performance enhancement and three-dimensional flow. *Energies* 2019, 12, 2724.

[38] Jodai, Y.; Hara, Y. Wind tunnel experiments on interaction between two closely spaced vertical-axis wind turbines in side-by-side arrangement. *Energies*, 2021, 14, 7874.

[39] Hara, Y.; Jodai, Y.; Okinaga, T.; Furukawa, M. Numerical analysis of the dynamic interaction between two closely spaced vertical-axis wind turbines. *Energies* 2021, 14, 2286.

[40] Furukawa, M.; Hara, Y.; Jodai, Y. Analytical model for phase synchronization of a pair of vertical-axis wind turbines. *Energies* 2022, 15, 4130.

[41] Buranarote, J.; Hara, Y.; Furukawa, M.; Jodai, Y. Method to Predict Outputs of Two-Dimensional VAWT Rotors by Using Wake Model Mimicking the CFD-Created Flow Field. *Energies* 2022, 15, 5200.

[42] Buranarote, J.; Hara, Y.; Jodai, Y.; Furukawa, M. A wake model simulating the velocity profile of a two-dimensional vertical axis wind turbine. *In Proceedings of the 7th International Conference on Jets, Wakes and Separated Flows*, ICJWSF–2022, Tokyo, Japan, 15–17 March 2022.

[43] Okinaga, T.; Hara, Y.; Yoshino, K.; Jodai, Y. Numerical simulation considering the variation in rotational speed of three closely spaced vertical-axis wind turbines. *In Proceedings of the JWEA 43rd Wind Energy Utilization Symposium*, Tokyo, Japan, 18–19 November 2021.

[44] http://www.damp.tottori-u.ac.jp/~lab6/index.html

Chapter 2

A method to predict outputs of VAWT cluster

2.1 Introduction

This chapter proposed a method to simulate the flow distribution around the rotors in a wind farm resulting to predict the rotor powers. Following the description of the background of the wake model, the potential flow which gave the basic flow field in the wind farm was explained. Then the modification of the velocity distribution of an isolated single rotor in each direction (mainstream direction and perpendicular direction) to mimic the realistic flow field including the velocity deficit was introduced. After that, the interaction effects among the rotors, especially wake shift and wake broadening, were considered with showing examples of the co-rotating paired rotors. From Section 2.3, a method about how to find out an appropriate combination of the circulations that gives the adequate rotor powers to a specific layout was proposed. It is shown that the method can find out a resultant condition that satisfies the conservation of momentum in a control volume. In the sub-sections, the correction functions which expressed the effects of the superposition of the wakes of rotors were introduced to modify the pressure loss of an isolated single rotor. The correction functions, or interaction functions, were categorized according to the typical four layouts of a paired rotor. Finally, to avoid wrong results, an idea to limit the searching range of the circulation of a rotor at issue was proposed by considering the relative arrangement between the rotor at issue and a counterpart rotor.

2.2 Wake model

2.2.1 Background

In this study, the flow field around vertical-axis wind turbines (VAWTs) is assumed to be two-dimensional. The flow field is based on the potential-flow like the method proposed by Whittlesey et al. [1], in which the ideal flow without vorticity is modified by introducing the velocity deficit artificially. This study proposes a new wake model to express the averaged velocity deficit observed in the wake of a VAWT. The model is based on the super-Gaussian function proposed by Shapiro et al. [2] which can express the transformation of the wake profile from a top-hat shape to a Gaussian shape regarding the x-component (mainstream direction) distribution of the flow velocity. To express the typical acceleration regions observed in the wake of a VAWT and the wake deflection, the proposed wake model in this study modifies the super-Gaussian function. In addition, although the method by Whittlesey et al. [1] does not include the modification of the *y*-component (cross-flow direction) of the flow velocity, the proposed wake model modifies the *y*-component of the potential flow to mimic the realistic averaged flow obtained by experiments or computational fluid dynamics (CFD). Moreover, the Biot-Savart law is introduced to express the effects of the interaction between the rotors in this study.

2.2.2 Potential flow

Figure 2.1 shows a schematic image of a VAWT wind farm, where a circle shows a VAWT rotor, and this method does not need detailed information on the configuration of a

turbine, such as the number of blades and the cross-section. In this method, the VAWTs are dealt with as 2D-rotors with having each diameter of D. Here, the wind farm is assumed to consist of N VAWTs. In Fig. 2.1, the coordinate axis x is defined as parallel to the upstream wind speed U_∞; the coordinate axis y is perpendicular to the dominant wind direction. The center position (rotational axis) of the k-th rotor is expressed as (x_k, y_k). The circulation around the k-th rotor is shown by Γ_k, and the dipole μ_k expresses the blockage effect.

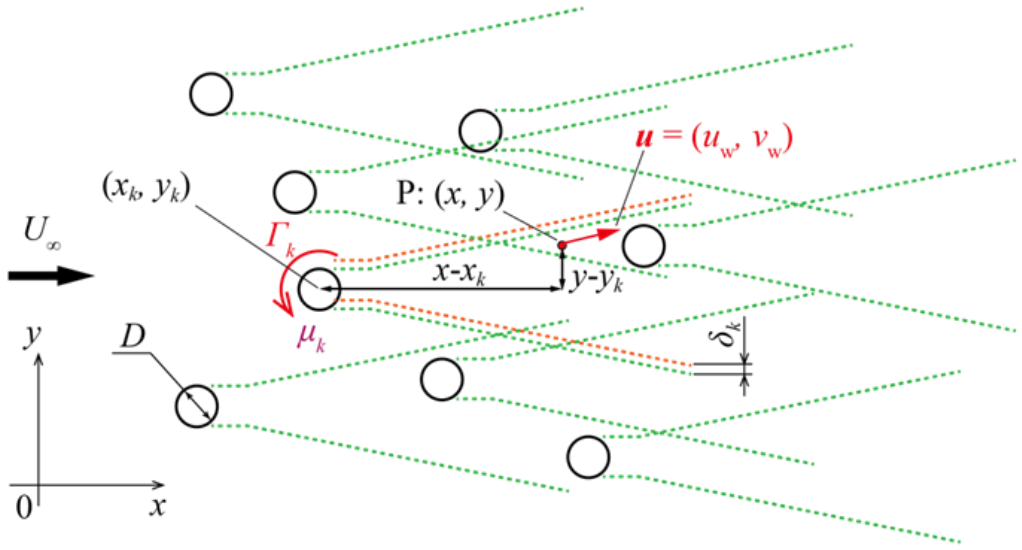

Fig. 2.1 Schematic image of wind farm of vertical-axis wind turbines (VAWTs)

If an arbitrary set of the conditions of circulation (Γ_k) and blockage effects (μ_k) is given for a wind farm, the complex velocity potential $W(z)$, where $z = x + iy$, is expressed by Eq. (2.1) [1]. Using the complex velocity potential $W(z)$, the potential flow (u_p, v_p) at an arbitrary position P: (x, y) in the wind farm can be calculated by Eq. (2.2) and Eq. (2.3).

$$W(z) = U_\infty z + \sum_{k=1}^{N} \left\{ -i \frac{\Gamma_k}{2\pi} ln(z - z_k) + \mu_k (z - z_k)^{-1} \right\} \tag{2.1}$$

$$u_{\mathrm{p}}(x, y) = U_\infty - \sum_{k=1}^{N} \left[\frac{\Gamma_k}{2\pi} \frac{(y - y_k)}{(x - x_k)^2 + (y - y_k)^2} + \mu_k \frac{(x - x_k)^2 - (y - y_k)^2}{\{(x - x_k)^2 + (y - y_k)^2\}^2} \right] \tag{2.2}$$

$$v_{\mathrm{p}}(x, y) = \sum_{k=1}^{N} \left[\frac{\Gamma_k}{2\pi} \frac{(x - x_k)}{(x - x_k)^2 + (y - y_k)^2} - \mu_k \frac{2(x - x_{\mathrm{k}})(y - y_k)}{\{(x - x_k)^2 + (y - y_k)^2\}^2} \right] \tag{2.3}$$

2.2.3 Wake model of the mainstream direction component (*x*-component: *u*)

The potential flow is an ideal flow and cannot express the actual velocity deficits or wakes generated by each rotor. Therefore, as Whittlesey et al. introduced [1], the component in the x-direction of the potential flow is modified by a wake function du_k showing the velocity deficit of each rotor; the resultant flow $u_{\mathrm{w}}(x, y)$ is expressed by Eq. (2.4). The wake function du_k is given by Eq. (2.5), which is based on the super-Gaussian function f_{SG_k} proposed by Shapiro et al. [2] expressing the wake profile transformation from a top-hat shape to a Gaussian shape. However, the proposed wake model by Eq. (2.5) includes the correction function $f_{\mathrm{COR\_k}}$ expressing the acceleration regions and the deflection δ_k of the wake. μ_{ref} is a reference value of the blockage effect and C_{w_k} is a fitting parameter to the prepared flow field of an isolated single rotor. In this study, the modified super-Gaussian function is named the ultra-super-Gaussian function f_{USG_k}.

$$u_{\mathrm{w}}(x,y) = u_{\mathrm{p}}(x,y)\left\{1 - \sum_{k=1}^{N} du_k\,(x,y)\right\} \tag{2.4}$$

$$du_k = C_{\mathrm{w\_}k}\frac{\mu_k}{\mu_{\mathrm{ref}}} f_{\mathrm{USG\_}k} = C_{\mathrm{w\_}k}\frac{\mu_k}{\mu_{\mathrm{ref}}}\{f_{\mathrm{SG\_}k} - f_{\mathrm{COR\_}k}\} \tag{2.5}$$

The super-Gaussian function [2] is expressed as follows:

$$f_{\mathrm{SG\_}k} = \exp\left[-\frac{D^2}{8{\sigma_0}^2}\left\{\frac{2\left|y_{\mathrm{n}\,\delta}\right|}{D d_{\mathrm{w}}(x_{\mathrm{n}})}\right\}^{p(x_{\mathrm{n}})}\right] \tag{2.6}$$

In the above, $\sigma_0 = D/4$. In our model, the function $p(x_{\mathrm{n}})$ is defined as follows:

$$p(x_{\mathrm{n}}) = 2\left(1 + f_{\mathrm{p}}/x_{\mathrm{n}}\right) \tag{2.7}$$

Here, $x_{\mathrm{n}} = (x - x_k)/D$ is the normalized coordinate. f_{p} is a fitting parameter that is not included in the original super-Gaussian function. Another function of x_{n} is defined in Eq. (2.8).

$$d_{\mathrm{w}}(x_{\mathrm{n}}) = 1 + k_{\mathrm{w}}\ln(1 + e^{2x_{\mathrm{n}}}) \tag{2.8}$$

In the above, k_{w} denotes the wake expansion coefficient of the original model. However, in the proposed model in this study, k_{w} is also a fitting parameter. The radial coordinate r of the original super-Gaussian function, Eq. (2.6) is replaced by the normalized coordinate $y_{\mathrm{n}\delta}$ including the wake shift δ_k in the model.

$$y_{\mathrm{n}\delta} = \frac{y - y_k - \delta_k}{D} \tag{2.9}$$

In general, the flow speed increases at the side edges of the wake region of a VAWT. To express the acceleration regions, the correction function is defined for $y_{\mathrm{n}\delta} \geq 0$ as follows:

$$f_{\mathrm{COR}} = 0 \qquad \text{for } \{0 \leq y_{\mathrm{n}\delta} < C_{\mathrm{P3}}\} \tag{2.10}$$

$$f_{\mathrm{COR}} = C_{\mathrm{P0}} \exp\left(-\frac{y_{\mathrm{n}\delta} - C_{\mathrm{P3}}}{C_{\mathrm{P1}}}\right)\left[\frac{1}{C_{\mathrm{P2}} - C_{\mathrm{P3}}}(y_{\mathrm{n}\delta} - C_{\mathrm{P3}})\right] \quad \text{for } \{C_{\mathrm{P3}} \leq y_{\mathrm{n}\delta} \leq C_{\mathrm{P2}}\} \tag{2.11}$$

$$f_{\mathrm{COR}} = C_{\mathrm{P0}} \exp\left(-\frac{y_{\mathrm{n}\delta} - C_{\mathrm{P3}}}{C_{\mathrm{P1}}}\right) \qquad \text{for } \{y_{\mathrm{n}\delta} > C_{\mathrm{P2}}\} \tag{2.12}$$

In the region $y_{\mathrm{n}\delta} < 0$, the correction function f_{COR} is defined as the following Eqs. (2.13)–(2.15):

$$f_{\mathrm{COR}} = 0 \qquad \text{for } \{-C_{\mathrm{N3}} < y_{\mathrm{n}\delta} < 0\} \tag{2.13}$$

$$f_{\mathrm{COR}} = C_{\mathrm{N0}} \exp\left(\frac{y_{\mathrm{n}\delta} + C_{\mathrm{N3}}}{C_{\mathrm{N1}}}\right)\left[\frac{-1}{C_{\mathrm{N2}} - C_{\mathrm{N3}}}(y_{\mathrm{n}\delta} + C_{\mathrm{N3}})\right] \quad \text{for } \{-C_{\mathrm{N2}} \leq y_{\mathrm{n}\delta} \leq -C_{\mathrm{N3}}\} \tag{2.14}$$

$$f_{\mathrm{COR}} = C_{\mathrm{N0}} \exp\left(\frac{y_{\mathrm{n}\delta} + C_{\mathrm{N3}}}{C_{N1}}\right) \qquad \text{for} \{y_{\mathrm{n}\delta} < -C_{\mathrm{N2}}\} \tag{2.15}$$

The parameters $C_{\mathrm{P0}}, C_{\mathrm{P1}}, C_{\mathrm{P2}}, C_{\mathrm{P3}}, C_{\mathrm{N0}}, C_{\mathrm{N1}}, C_{\mathrm{N2}}$, and C_{N3} in Eq. (2.11) to Eq. (2.15) are determined by fitting the model to the averaged flow obtained by CFD analysis of an isolated single rotor in this study. An example graph of f_{COR} is shown in Fig. 2.2. Figure 2.2 shows the wake profile in the mainstream direction (x-component: u) at $x_{\mathrm{n}} = 2.0$ of a single rotor. The horizontal axis is the non-dimensional relative coordinate in the y direction to the center of the rotor, that is, $y_{\mathrm{n}} = (y - y_k)/D$. The dotted curve in purple shows the profile of potential flow and the curve in green shows the super-Gaussian function. The profile shown in red is the results obtained by CFD analysis, the details of which will be explained in Chapter 3. As shown in Fig. 2.2, the velocity deficit predicted by the CFD can be fit well using the super-Gaussian function, however, the peaks indicating velocity acceleration on both sides of the velocity deficit cannot be reproduced by the super-Gaussian function. Therefore, the super-Gaussian function is corrected by using the correction function f_{COR} that combines the exponential function and the linear function as shown in Fig. 2.3. Figure 2.3 shows the region of $y_{\mathrm{n}\delta} \geq 0$, and $C_{\mathrm{P0}}, C_{\mathrm{P1}}, C_{\mathrm{P2}}$, and C_{P3} are the fitting parameters in that

positive region. Although the same correction is applied to the region of $y_{n\delta} < 0$, due to the asymmetric distribution, the fitting parameters in the negative region are defined as C_{N0}, C_{N1}, C_{N2}, and C_{N3}, and the fitting is independently carried out. The ultra-super-Gaussian function f_{USG_k} is illustrated by a dotted curve in blue in Fig. 2.2, which shows good agreement between the wake profiles created by the ultra-super-Gaussian function and the CFD analysis.

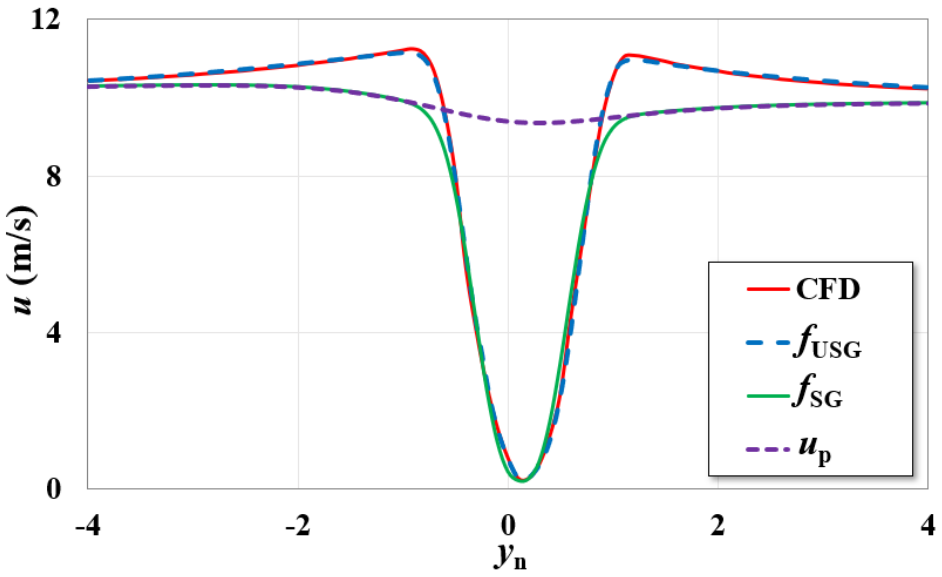

Fig. 2.2 Wake profile in the mainstream direction (x-component: u) at $x_n = 2.0$ of a single rotor

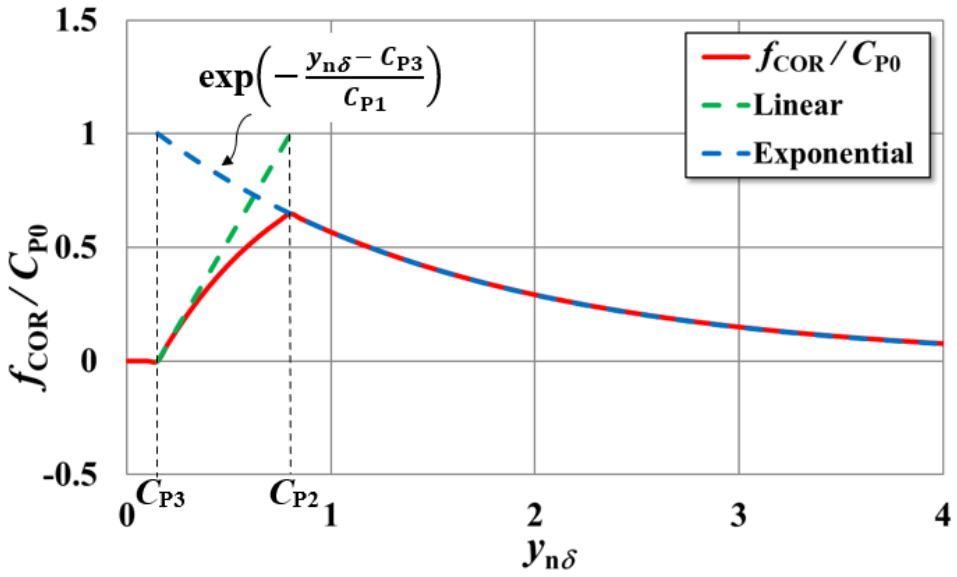

Fig. 2.3 Correction function for positive range in $y_{n\delta}$

2.2.4 Wake model of the cross-flow direction component (*y*-component: *v*)

The *y*-direction velocity component $v_w(x, y)$, which is the average of the unsteady flow calculated by CFD analysis for a VAWT wind farm, is different from that obtained by the potential flow. Therefore, in this study, the potential flow $v_p(x, y)$ is modified by adding the additional function $dv_k(x, y)$. The function $dv_k(x, y)$ is assumed to be proportional to the absolute value of the circulation Γ_k, which is obtained by integrating the flow velocity along a circle with a radius of $r = 0.75D$ (which is defined as the evaluation position or e.p.) around the *k*-th rotor. The circulation Γ_{SI} in Eq. (2.16) is obtained from the CFD simulation of an isolated single rotor at a reference wind speed U_∞. The nondimensional function dv_k is expressed by the superposition of four Gaussian-type functions f_{G_i} and four resonance-type functions f_{R_i}, as shown in Eq. (2.17). The Gaussian- and resonance-type functions are

defined by Eq. (2.18) and Eq. (2.19), respectively. The concrete examples of the *y*-component profiles are shown in the later (see Fig. 2.8).

$$v_{\mathrm{w}}(x,y) = v_{\mathrm{p}}(x,y) + U_{\infty}\sum_{\mathrm{k}=1}^{N}\frac{|\Gamma_k|}{|\Gamma_{\mathrm{SI}}|}dv_k\,(x,y) \tag{2.16}$$

$$dv_k = \sum_{i=1}^{4} f_{\mathrm{G}\_i} + \sum_{i=1}^{4} f_{\mathrm{R}\_i} \tag{2.17}$$

$$f_{\mathrm{G}\_i} = C1_{\mathrm{fg}\_i}\exp\left(-\frac{\left(y_{\mathrm{n}\delta} - C3_{\mathrm{fg}\_i}\right)^2}{C2_{\mathrm{fg}\_i}}\right) \tag{2.18}$$

$$f_{\mathrm{R}\_i} = \frac{C1_{\mathrm{fr}\_i}}{1 + C2_{\mathrm{fr}\_i}\left(y_{\mathrm{n}\delta} - C3_{\mathrm{fr}\_i}\right)^2} \tag{2.19}$$

2.2.5 Fitting parameters in the wake models

The wake flow prediction process starts by determining the values of the fitting parameters in the wake models of an isolated single rotor by mimicking the averaged flow velocity field obtained by the CFD simulation (see Fig. 3.6 in Section 3.3). In this study, the reference wind speed U_{∞} is set as 10 m/s, with which the CFD analysis is conducted.

There are 11 parameters required to calculate the velocity deficit du in Eq. (2.5) for a single rotor and 24 parameters to calculate the function dv in Eq. (2.17). Note that the subscript *k* is omitted because, here, an isolated single rotor is considered. The procedure for

determining the parameter values including the blockage μ is shown in Fig. 2.4. The first step is to set both the circulation Γ (assumed to be the strength of the circulation at the center of the rotor) and dipole μ as the input data for the calculation of the potential flow. In the second step, a parameter value set giving the smallest error in an appropriate parameter range is searched for at each of the 46 different relative positions in the mainstream direction from $x_{\mathrm{n}} = -10$ to 10. Subsequently, using the obtained parameter values, the flow velocity distribution is calculated using Eq. (2.4) and Eq. (2.16), without summation for the other rotors. The flow field is then integrated along the circle defined as the evaluation position to obtain the circulation value Γ_{ep}. The calculated circulation value Γ_{ep} from the integration is compared with the value $\Gamma_{\mathrm{ep\_CFD}}$ obtained by CFD result. If the difference between both circulations at the evaluation position is larger than a small value ε (assumed to be 0.0005 m^2/s in this study), other values of Γ and μ are selected. The same procedure is repeated with the new values, i.e., with the iterative method, to determine the rotor circulation Γ and the reference value of the blockage effect μ_{ref}. After the execution of this procedure, μ_{ref} is determined, as well as Γ and the other 35 parameters. There are 11 fitting parameters (C_w, k_w, f_{p}, C_{N0}, C_{N1}, C_{N2}, C_{N3}, C_{P0}, C_{P1}, C_{P2}, and C_{P3}) in f_{USG}, the values are shown in Table 2.1. There are 24 fitting parameters ($C1_{\mathrm{fg\_}i}$, $C2_{\mathrm{fg\_}i}$, $C3_{\mathrm{fg\_}i}$, $C1_{\mathrm{fr\_}i}$, $C2_{\mathrm{fr\_}i}$, and $C3_{\mathrm{fr\_}i}$; [i = 1 to 4]) in the function dv, the values are shown in Table 2.2 for the functions $f_{\mathrm{G\_}i}$ and Tables 2.3 for the functions $f_{\mathrm{R\_}i}$. The fitting parameters are determined at 46 positions between $x_{\mathrm{n}} = -10$ and $x_{\mathrm{n}} = 10$ in the x-direction by comparison between the velocity profiles of the model and the CFD result. At an arbitrary x-position in the flow field, the parameters are used for interpolation.

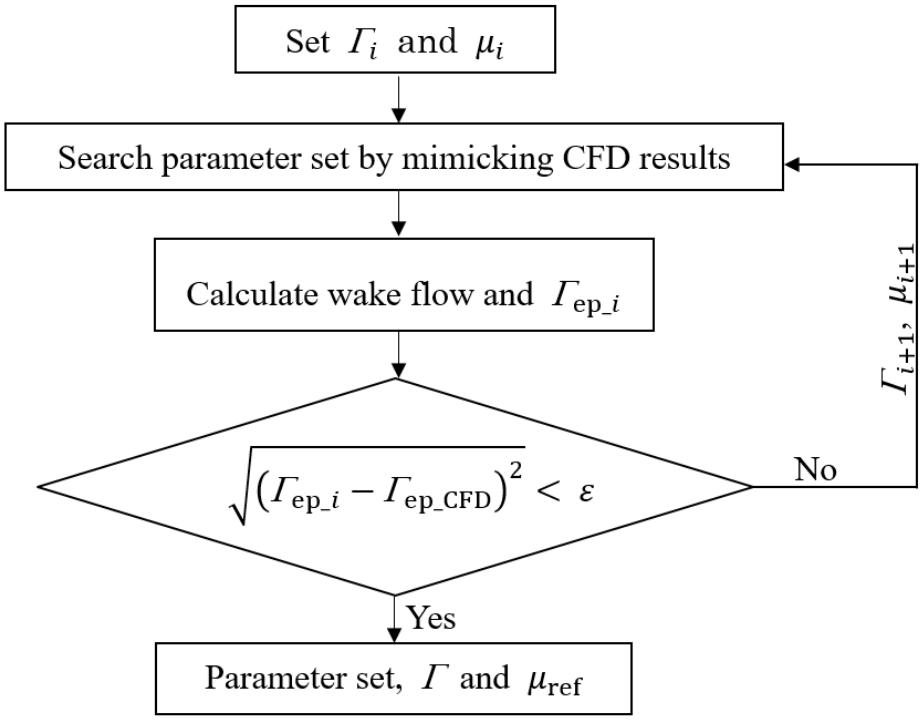

Fig. 2.4 Flowchart of determination of fitting parameters and blockage for the reference wind speed of an isolated single target rotor

Table 2.1 The fitting parameters in the ultra-super-Gaussian function, f_{USG}

x_n	C_w	k_w	f_p	C_{N0}	C_{N1}	C_{N2}	C_{N3}	C_{P0}	C_{P1}	C_{P2}	C_{P3}
−10	0.0091	0.6582	0.7010	0.2542	0.9057	0.2054	0.1845	0.4361	2.1068	0.2156	0.1880
−8	0.0114	0.6905	0.0993	−0.4745	4.7472	2.6759	1.1221	0.2326	0.7857	0.4652	0.1646
−6	0.0168	0.7932	1.3848	−0.5536	5.5377	3.1215	1.3090	0.1482	0.9012	0.5873	0.0326
−4	0.0274	0.9092	0.8591	−0.3956	7.7506	1.4080	0.5688	−0.0644	1.6639	3.3820	0.4386
−2	0.0768	0.7449	0.3266	−0.6307	1.8931	2.0142	0.7956	0.1582	15.5537	5.7160	2.4223
−1	0.1826	0.7898	0.0532	−0.2961	1.0724	1.4556	0.8866	0.1070	13.8469	3.3443	1.4025
−0.75	0.2772	0.5971	0.0423	−0.3472	0.7244	1.4133	0.7344	0.0878	9.8289	2.8971	1.5263
−0.7	0.3000	0.6001	0.0161	−0.4380	0.5724	1.6683	0.7654	0.0849	12.3316	3.0527	0.4652
−0.6	0.2882	0.6330	0.0552	−0.2869	0.6256	1.3519	0.7741	0.1008	9.7876	2.6759	0.5537
−0.5	0.3282	0.5557	0.0002	−0.3087	0.5715	1.2986	0.6040	0.1042	7.4638	2.5409	0.7335
−0.4	0.2887	0.5019	0.0501	−0.3079	0.4466	1.1460	0.6543	0.1325	6.5829	1.9413	0.8771
−0.3	0.4235	0.2310	0.0501	−0.2739	0.3718	0.9942	0.5110	0.1035	5.9861	1.6361	0.7088
−0.2	0.6754	0.2062	0.4530	−0.2698	0.3480	0.1711	0.1711	0.0797	5.2713	1.2941	0.3692
−0.1	0.6232	0.0334	0.1954	−0.0935	0.2087	0.5196	0.5196	0.1074	4.5032	0.2434	0.2433
0	0.5428	0.0002	0.0503	0.0376	3.2977	1.8589	0.4196	0.1575	3.6227	0.2587	0.2586
0.1	0.6577	0.0002	0.3936	0.0636	2.3979	1.7094	0.0005	0.1713	3.0411	0.2162	0.2161
0.2	0.7026	0.0002	0.8119	0.0569	2.7857	0.9608	0.0870	0.1869	2.7598	0.2382	0.2343
0.3	0.5986	0.2500	2.4680	0.0966	2.3364	0.1319	0.0618	0.2673	2.5117	0.4382	0.1426
0.4	0.7250	0.2348	2.5906	0.0879	2.0929	0.7942	0.4227	0.2282	2.4431	0.7059	0.2423
0.5	0.9100	0.2414	2.0028	0.0762	1.8844	0.7625	0.7146	0.2028	2.2853	0.5807	0.2810
0.6	0.9017	0.2699	1.4722	0.1082	1.9000	0.2629	0.2554	0.2149	2.0951	0.6432	0.4851
0.7	0.8632	0.2434	2.0263	0.1524	1.7128	0.4202	0.1218	0.2324	2.1085	0.6836	0.4465
0.75	0.8382	0.2401	2.2507	0.1566	1.7334	0.5260	0.1615	0.2393	2.1085	0.6402	0.4687
0.8	0.8504	0.2306	2.3917	0.1651	1.7208	0.5245	0.1327	0.2456	2.0862	0.6898	0.4399
0.9	0.8672	0.2166	2.4366	0.1739	1.7442	0.5439	0.0802	0.2452	2.1060	0.6962	0.4270
1	0.8762	0.2012	2.2059	0.2108	1.5943	0.8172	0.0553	0.2418	2.1336	0.7414	0.4284
1.1	0.8914	0.1931	2.1107	0.2157	1.6410	0.8202	0.0080	0.2379	2.1930	0.7759	0.3961
1.2	0.8879	0.1777	1.9914	0.2077	1.6346	0.8721	0.1508	0.2282	2.2008	0.8100	0.5021
1.3	0.9051	0.1636	1.8485	0.2067	1.7130	0.9247	0.0650	0.2064	2.2741	0.7501	0.6179
1.4	0.9128	0.1570	1.7436	0.2088	1.7008	0.9034	0.0864	0.2033	2.2947	0.7559	0.6180
1.5	0.9219	0.1498	1.6507	0.2090	1.7150	0.8972	0.0837	0.2025	2.3173	0.8285	0.5823
1.6	0.9303	0.1494	1.3965	0.2043	1.7353	0.8768	0.0966	0.1889	2.4271	0.7589	0.6133
1.7	0.9296	0.1336	1.4457	0.1977	1.7899	0.9275	0.1035	0.1875	2.4322	0.8566	0.6182
1.8	0.9378	0.1281	1.2945	0.1940	1.8314	0.9296	0.0805	0.1801	2.4907	0.8648	0.6216
1.9	0.9436	0.1284	1.1287	0.1920	1.8235	0.8183	0.0833	0.1748	2.5667	0.9122	0.5759
2	0.9740	0.1333	1.3191	0.1849	1.8677	0.3759	0.0424	0.1971	2.6559	0.9214	0.0583
2.1	0.9750	0.1277	1.1529	0.1757	1.9256	0.3570	0.0216	0.1867	2.7499	0.9503	0.0442
2.2	0.9441	0.1243	1.1448	0.1661	2.0006	0.4031	0.0826	0.1743	2.8841	0.9444	0.1459
2.3	0.9400	0.1194	1.0655	0.1572	2.0721	0.3583	0.0821	0.1666	2.9870	0.9797	0.1179
2.4	0.9266	0.1147	0.9121	0.1495	2.1548	0.3858	0.0739	0.1531	3.0981	0.9936	0.2387
2.5	0.9105	0.1129	0.8607	0.1441	2.2145	0.3849	0.0788	0.1480	3.2481	1.0166	0.1923
3	0.7977	0.1058	0.6963	0.1077	2.8396	0.3861	0.0758	0.1184	4.2106	1.1886	0.1689
4	0.5657	0.1063	0.4007	0.3131	2.1568	6.6251	0.1685	0.3866	2.6141	6.8336	0.3954
6	0.3571	0.1143	0.3388	0.1253	3.5691	7.9674	1.5521	0.2249	3.9554	7.7057	1.1499
8	0.3064	0.1051	0.0357	0.0941	4.8910	8.3139	0.8055	0.1531	5.3229	7.8979	1.2282
10	0.2920	0.0905	0.3596	0.1307	3.5955	8.6259	1.2900	0.1461	5.2149	7.7429	1.0662

Table 2.2 The fitting parameters in Gaussian-type functions, f_{G_i}

x_n	$C1_{fg1}$	$C2_{fg1}$	$C2_{fg1}$	$C1_{fg2}$	$C2_{fg2}$	$C2_{fg2}$	$C1_{fg3}$	$C2_{fg3}$	$C2_{fg3}$	$C1_{fg4}$	$C2_{fg4}$	$C3_{fg4}$
−10	0.0235	0.1686	−0.3653	−0.0231	0.1752	−0.3619	−0.0597	0.0938	1.5479	0.0597	0.0952	1.5486
−8	0.0108	0.1888	−0.2683	−0.0081	0.1372	−0.3694	−0.0103	0.1976	0.1644	0.0078	0.1417	0.2737
−6	0.0135	0.1554	−0.3257	−0.0159	0.1723	−0.2669	−0.0427	0.1721	0.1944	0.0448	0.1779	0.1726
−4	0.0229	0.4217	−1.3449	−0.0224	0.4184	−1.3278	−0.0531	0.0965	0.4337	0.0540	0.0973	0.4337
−2	0.0082	0.3241	−1.1351	−0.0044	0.3085	−1.0243	0.0142	0.2679	0.3599	−0.0101	0.7884	0.4118
−1	0.0250	0.4050	−1.2649	−0.0250	0.3950	−1.1774	0.0156	0.4366	0.2983	−0.0092	1.1056	0.5103
−0.75	−0.0212	0.2538	−0.5622	0.0362	0.1196	−0.2382	0.0133	0.1835	0.9382	−0.0112	0.4931	0.8562
−0.7	−0.0198	0.1009	−0.9601	−0.0194	0.0485	−0.5937	−0.0272	0.2134	0.5007	0.0221	0.7050	0.1507
−0.6	−0.0421	0.5509	−0.2054	0.0235	0.0507	−0.5007	0.0202	0.2292	0.7502	−0.0123	1.0304	0.4118
−0.5	−0.1213	1.1116	−0.4966	0.0780	1.1743	−0.7618	0.1627	0.1053	0.8753	−0.1438	0.1041	0.8753
−0.4	−0.1678	0.9429	−0.7003	0.1329	1.0688	−0.8001	0.0942	0.1765	0.3735	−0.1902	0.1649	0.2601
−0.3	−0.0451	0.6440	−0.7994	0.0202	1.1743	−1.0633	−0.0198	0.1237	0.5260	−0.0968	0.0549	0.4159
−0.2	−0.0870	0.3531	−0.4945	0.0488	0.1115	−0.6442	−0.0277	0.0174	0.4979	−0.1414	0.1458	0.2983
−0.1	−0.0111	0.1642	−1.1036	0.0371	0.0441	−0.5663	0.0461	0.2134	0.8890	−0.1499	0.5382	0.2635
0	−0.0282	0.2644	−0.7399	0.0321	0.2067	−0.5096	−0.0188	0.1606	0.6415	−0.1988	0.1055	0.3195
0.1	−0.0101	0.1185	−1.0749	0.0648	0.0471	−0.5048	−0.0347	0.0912	0.5759	−0.1326	0.1690	0.1507
0.2	−0.0086	0.1905	−0.8931	0.0829	0.0559	−0.4788	0.1798	0.0244	0.5212	−0.1983	0.0467	0.4911
0.3	−0.0207	0.4419	−0.3236	0.0560	0.1071	−0.4590	0.0998	0.1044	0.3243	−0.0432	0.0118	0.7140
0.4	−0.0301	0.2881	−0.8644	0.0458	0.5590	−0.4720	0.0930	0.0640	0.4118	−0.0321	0.0200	0.7194
0.5	−0.0782	0.4384	−0.6955	0.1074	0.5869	−0.4583	0.0617	0.1149	0.4528	−0.0458	0.0221	0.7659
0.6	−0.0075	0.1009	−0.8507	0.0620	0.1972	−0.3284	0.0980	0.0508	0.4549	−0.0153	0.1649	0.3134
0.7	−0.0116	0.2116	−0.5554	0.0341	0.0302	−0.4679	0.0823	0.6071	0.2744	−0.0290	0.8212	0.6627
0.75	−0.0559	0.4797	−0.5663	0.0822	0.6792	−0.2601	0.0606	0.8796	0.3729	−0.0480	1.1384	0.5431
0.8	−0.0641	0.4331	−0.5472	0.0928	0.5810	−0.2874	0.0702	0.8866	0.4494	−0.0569	1.0591	0.6319
0.9	−0.0324	0.2019	−0.6852	0.0464	0.5345	−0.4195	0.2196	0.8986	0.2774	−0.1847	1.1113	0.2855
1	−0.0195	0.0280	−0.6645	0.0231	0.0927	−0.3909	0.1242	0.8241	0.7064	−0.1016	0.6778	0.9532
1.1	−0.0107	0.2134	−0.5882	0.0321	0.0485	−0.3264	0.1567	0.9455	0.5062	−0.1289	1.0222	0.6326
1.2	−0.0219	0.1079	−0.4754	0.0590	0.0661	−0.3271	0.1216	0.9341	0.6162	−0.1017	0.9743	0.7481
1.3	−0.0558	0.0745	−0.5868	0.0794	0.1665	−0.3756	0.0442	0.1009	0.5868	−0.0063	1.0618	1.4181
1.4	−0.0680	0.0872	−0.5884	0.0808	0.1703	−0.4052	0.0379	0.0807	0.5984	−0.0082	0.8341	1.3434
1.5	−0.0694	0.0877	−0.5999	0.0810	0.1966	−0.4046	0.0406	0.0807	0.6152	−0.0074	1.1495	1.6060
1.6	−0.0722	0.0915	−0.5991	0.1011	0.2151	−0.3756	0.0540	0.1458	0.6705	−0.0273	0.7772	0.5111
1.7	−0.0551	0.0708	−0.5765	0.0867	0.1519	−0.3620	0.0340	0.0817	0.6651	−0.0060	1.3904	1.0672
1.8	−0.0155	0.0552	−0.5759	0.0634	0.0961	−0.2594	0.1763	0.0736	0.6538	−0.1443	0.0795	0.6524
1.9	−0.0372	0.0745	−0.5528	0.0779	0.1463	−0.2945	0.0737	0.2138	0.7138	−0.0492	0.4508	0.6401
2	−0.0160	0.0745	−0.5143	0.0693	0.0894	−0.2747	0.1489	0.0990	0.7382	−0.1203	0.1036	0.7424
2.1	−0.0602	0.0877	−0.5690	0.0880	0.1811	−0.3981	0.0455	0.3259	0.6873	−0.0301	0.8226	0.5003
2.2	−0.0496	0.0991	−0.5868	0.0715	0.2031	−0.3920	0.0619	0.1132	0.6155	−0.0466	0.1882	0.5007
2.3	−0.0718	0.1378	−0.5964	0.0937	0.2646	−0.4255	0.0416	0.1352	0.6401	−0.0276	0.5382	0.2819
2.4	−0.0469	0.1202	−0.5868	0.0655	0.2646	−0.3790	0.0355	0.1202	0.6436	−0.0234	0.4507	0.3257
2.5	−0.0363	0.1149	−0.6060	0.0529	0.2998	−0.3735	0.0284	0.1158	0.6360	−0.0172	0.5382	0.2382
3	−0.0111	1.4491	−1.3743	0.0219	0.8227	−0.7618	0.0533	0.3804	0.3011	−0.0405	0.7993	0.2054
4	0.0096	0.1062	−1.1569	−0.0037	0.2368	−1.0284	0.0125	0.1835	0.3284	−0.0099	0.2470	1.3101
6	0.0224	0.6458	−0.8438	−0.0217	0.7993	−0.8329	−0.0067	0.0921	0.2259	0.0139	0.1854	0.1944
8	0.0231	0.4278	−0.6121	−0.0225	0.3979	−0.6374	−0.0258	0.4929	0.5649	0.0301	0.4274	0.5417
10	0.0247	0.4050	−1.0838	−0.0246	0.3745	−1.0626	−0.0270	0.4929	0.4884	0.0312	0.4425	0.4774

Table 2.3 The fitting parameters in resonance-type functions, f_{R_i}

x_n	$C1_{fr1}$	$C2_{fr1}$	$C3_{fr1}$	$C1_{fr2}$	$C2_{fr2}$	$C3_{fr2}$	$C1_{fr3}$	$C2_{fr3}$	$C3_{fr3}$	$C1_{fr3}$	$C2_{fr3}$	$C3_{fr3}$
−10	0.2350	0.0101	−0.0006	−0.2396	0.0101	0.3111	1.6824	1.4410	−0.0001	−1.6824	1.4410	0.0001
−8	0.2405	0.0087	−0.2206	−0.2456	0.0087	0.2860	1.0335	1.3209	−0.0001	−1.0335	1.3209	0.0001
−6	0.2470	0.0161	−0.0988	−0.2538	0.0163	0.4355	1.2991	0.6408	−0.0004	−1.2991	0.6408	0.0004
−4	0.2460	0.0237	−0.4757	−0.2534	0.0237	0.2733	1.7798	0.8008	0.0007	−1.7798	0.8008	−0.0007
−2	0.3042	0.0648	−0.4639	−0.3168	0.0652	0.3341	2.6455	1.2809	0.0024	−2.6455	1.2809	−0.0024
−1	0.2864	0.0647	−0.6180	−0.3014	0.0660	0.1831	4.6927	0.6408	0.0159	−4.6927	0.6408	−0.0159
−0.75	0.2980	0.0607	−0.6671	−0.3132	0.0622	0.0819	5.0415	0.8016	0.0214	−5.0415	0.8016	−0.0214
−0.7	0.2742	0.0568	−0.2993	−0.2964	0.0632	0.4784	5.5835	0.8906	0.0209	−5.5835	0.8906	−0.0209
−0.6	0.2550	0.0575	−0.4743	−0.2768	0.0636	0.3882	6.0181	1.0445	0.0213	−6.0181	1.0445	−0.0213
−0.5	0.2636	0.0556	−0.5181	−0.2821	0.0600	0.3116	6.0327	1.1109	0.0240	−6.0327	1.1109	−0.0240
−0.4	0.2591	0.0565	−0.5181	−0.2791	0.0619	0.3062	6.0938	1.1992	0.0259	−6.0938	1.1992	−0.0259
−0.3	0.2593	0.0562	−0.4743	−0.2776	0.0613	0.3062	6.0913	1.0992	0.0268	−6.0913	1.0992	−0.0268
−0.2	0.2771	0.0544	−0.2200	−0.2958	0.0603	0.4757	6.1938	1.0992	0.0275	−6.1938	1.0992	−0.0275
−0.1	0.2784	0.0538	−0.1899	−0.2959	0.0594	0.4757	6.1182	0.9992	0.0273	−6.1182	0.9992	−0.0273
0	0.2802	0.0552	−0.1681	−0.2976	0.0613	0.4873	6.1572	0.9992	0.0267	−6.1572	0.9992	−0.0267
0.1	0.2839	0.0538	−0.3431	−0.2976	0.0577	0.3075	6.0498	0.9992	0.0267	−6.0498	0.9992	−0.0267
0.2	0.2344	0.0547	−0.4962	−0.2447	0.0578	0.3116	5.8423	1.0453	0.0269	−5.8423	1.0453	−0.0269
0.3	0.2285	0.0538	−0.5071	−0.2355	0.0557	0.3021	5.7690	0.9570	0.0257	−5.7690	0.9570	−0.0257
0.4	0.2608	0.0557	−0.2966	−0.2665	0.0575	0.3896	5.6689	0.9008	0.0244	−5.6689	0.9008	−0.0244
0.5	0.2589	0.0510	−0.2316	−0.2619	0.0519	0.4347	5.3271	0.8008	0.0244	−5.3271	0.8008	−0.0244
0.6	0.2679	0.0500	−0.1260	−0.2689	0.0505	0.5311	5.3979	0.8008	0.0214	−5.3979	0.8008	−0.0214
0.7	0.2399	0.0501	−0.0382	−0.2391	0.0505	0.7026	4.7998	0.8008	0.0217	−4.7998	0.8008	−0.0217
0.75	0.2698	0.0542	0.0493	−0.2668	0.0539	0.7136	4.1235	0.8039	0.0238	−4.1235	0.8039	−0.0238
0.8	0.2462	0.0580	0.0493	−0.2421	0.0575	0.7806	4.5215	0.8227	0.0196	−4.5215	0.8227	−0.0196
0.9	0.2860	0.0580	0.0518	−0.2794	0.0566	0.6763	4.8775	0.7918	0.0158	−4.8775	0.7918	−0.0158
1	0.2571	0.0519	0.0542	−0.2494	0.0501	0.7363	5.2356	0.7008	0.0131	−5.2356	0.7008	−0.0131
1.1	0.2719	0.0569	0.0542	−0.2620	0.0544	0.7061	4.3723	0.7208	0.0117	−4.3723	0.7208	−0.0117
1.2	0.1681	0.0445	0.0710	−0.1605	0.0426	1.0612	2.2775	0.5074	0.0210	−2.2775	0.5074	−0.0210
1.3	0.3056	0.0543	−0.2436	−0.2901	0.0497	0.3166	2.4834	0.6488	0.0115	−2.4834	0.6488	−0.0115
1.4	0.3011	0.0707	0.0688	−0.2866	0.0673	0.6694	3.0307	1.0250	0.0035	−3.0307	1.0250	−0.0035
1.5	0.3249	0.0551	−0.2494	−0.3071	0.0503	0.2907	2.3580	1.6010	0.0019	−2.3580	1.6010	−0.0019
1.6	0.2896	0.0539	−0.2406	−0.2722	0.0488	0.3316	2.5045	1.6788	−0.0028	−2.5045	1.6788	0.0028
1.7	0.2894	0.0482	−0.1825	−0.2739	0.0442	0.3709	2.3087	1.5857	−0.0061	−2.3087	1.5857	0.0061
1.8	0.2839	0.0425	−0.3007	−0.2681	0.0386	0.2556	1.9482	1.1992	−0.0108	−1.9482	1.1992	0.0108
1.9	0.3027	0.0386	−0.0691	−0.2893	0.0361	0.4328	2.6024	1.3038	−0.0101	−2.6024	1.3038	0.0101
2	0.2838	0.0284	−0.1701	−0.2721	0.0264	0.3567	2.1167	1.6008	−0.0142	−2.1167	1.6008	0.0142
2.1	0.2867	0.0319	−0.0874	−0.2739	0.0297	0.4251	4.2651	1.0992	−0.0097	−4.2651	1.0992	0.0097
2.2	0.2430	0.0313	−0.1366	−0.2300	0.0285	0.4306	4.7534	1.2008	−0.0100	−4.7534	1.2008	0.0100
2.3	0.2664	0.0291	−0.0942	−0.2542	0.0270	0.4251	5.3882	1.0398	−0.0098	−5.3882	1.0398	0.0098
2.4	0.2539	0.0294	−0.0901	−0.2412	0.0271	0.4306	5.8081	1.0281	−0.0100	−5.8081	1.0281	0.0100
2.5	0.2307	0.0250	−0.1487	−0.2185	0.0228	0.4444	5.9830	0.9945	−0.0104	−5.9830	0.9945	0.0104
3	0.2566	0.0226	−0.1334	−0.2425	0.0203	0.3124	4.3969	0.8562	−0.0176	−4.3969	0.8562	0.0176
4	0.2470	0.0164	0.0075	−0.2347	0.0147	0.3545	5.3616	0.5986	−0.0135	−5.3616	0.5986	0.0135
6	0.2499	0.0098	0.0062	−0.2410	0.0089	0.1392	2.5100	0.4103	−0.0108	−2.5100	0.4103	0.0108
8	0.2223	0.0098	0.0395	−0.2160	0.0094	0.1740	2.9275	0.4103	−0.0014	−2.9275	0.4103	0.0014
10	0.2540	0.0253	0.0462	−0.2489	0.0254	0.1833	3.1876	0.3155	0.0001	−3.1876	0.3155	−0.0001

2.2.6 Interaction model

The circulation deflects the wake and causes the interaction between the rotors. To take the effects into consideration, the Biot-Savart law is introduced, in this study, to consider the variations in the wake shift and the width owing to the interaction between the rotors. Figure 2.5 shows a schematic of a pair of rotors and the induced velocities $\Delta V_{\mathrm{ind}\_k}, \Delta V_{\mathrm{ind}\_j}$ at an arbitrary point caused by the *k*-th rotor and *j*-th rotor.

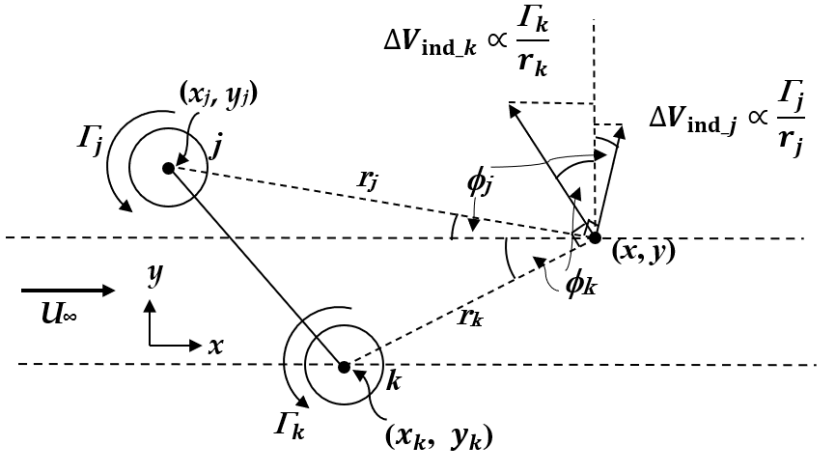

Fig. 2.5 Schematic image of the induced velocities of a rotor pair

The wake shift δ_k introduced in Eq. (2.9) can be expressed in the present wake model using Eq. (2.20). The function $(\Gamma_k/\Gamma_{\mathrm{SI}})\delta_{\mathrm{SI}}$ in front of the bracket on the right side of Eq. (2.20) is the wake deflection of a single rotor at an arbitrary upstream wind speed. The wake shift of the considered *k*-th rotor is assumed to be proportional to the circulation. As mentioned previously, Γ_{SI} is the circulation obtained from the CFD simulation of an isolated single rotor at the reference wind speed; δ_{SI} is the wake shift of the rotor in the reference

wind condition. The second term in the bracket expresses the effects of the interaction on the wake shift of the *k*-th rotor (δ_k), and is related to the *x*- and *y*-components of the induced velocity ($\Delta V_{\mathrm{ind}\_k}, \Delta V_{\mathrm{ind}\_j}$) at an arbitrary point (see Fig. 2.5). Factors β_1 and β_2 are correction constants for the wake shift in the case of the VAWT cluster. The sign of the second term in parenthesis in Eq. (2.20) depends on the rotational direction of the pair rotor, and is positive for a rotor pair rotating in the same direction. The sign before the induced velocity v_{ind} in the index of the exponential function in Eq. (2.20) is positive when the rotor rotates in the counterclockwise direction. The *x*-component of the induced velocity caused by the *j*-th rotor at an arbitrary point is given by Eq. (2.21). Similarly, the *y*-component of the induced velocity is expressed by Eq. (2.22).

$$\delta_k = \frac{\Gamma_k}{\Gamma_{\mathrm{SI}}}\delta_{\mathrm{SI}}\left[1 \pm (1-\beta_1 u_{\mathrm{ind}})|v_{\mathrm{ind}}|\left(1 - e^{-\frac{(x-x_k)}{\beta_2 D(1\pm v_{\mathrm{ind}})}}\right)\right] \tag{2.20}$$

$$u_{\mathrm{ind}} = \sum_j \frac{\Gamma_j}{r_j}\sin\phi_j \tag{2.21}$$

$$v_{\mathrm{ind}} = \sum_j \frac{\Gamma_j}{r_j}\cos\phi_j \tag{2.22}$$

In addition to its effect on the wake shift, the interaction also affects the wake width. Therefore, a factor $(1+\alpha)$ is added to the expression for $d_{\mathrm{w}}(x_{\mathrm{n}})$ in Eq. (2.8) to improve the prediction of the wake width, as expressed in Eq. (2.23). Equation (2.24) defines the variable

α, which consists of a constant β_3 and the summation of the effects of u_{ind} caused by all the rotors except for the k-th rotor.

$$d_{\mathrm{w}}(x_{\mathrm{n}}) = 1 + k_{\mathrm{w}}\ln\left(1 + e^{2(1+\alpha)x_{\mathrm{n}}}\right) \tag{2.23}$$

$$\alpha = \beta_3 \sum_{j \neq k} \frac{\Gamma_j}{r_j} \sin\phi_j \tag{2.24}$$

2.2.7 Flow field simulation

The rough procedure for simulating the flow field around VAWT cluster and the rotor performances is shown in Fig. 2.6. In the beginning, the calculation conditions (the upstream wind speed (U_∞), the center coordinates of rotors (x_k, y_k), and the rotational directions) and parameters set obtained by CFD analysis of an isolated single rotor are input. If the circulations Γ_k and blockages μ_k are given in some way, the potential flow ($u_p(x, y)$, $v_p(x, y)$) is calculated. Then, the wake flow ($u_w(x, y)$, $v_w(x, y)$) is obtained using the wake model in this study. The new circulation $\Gamma_{\mathrm{ep\_}k}$ of each rotor can be obtained by integration of the created flow field along a circle path of the radius equal to the evaluation position (e.p.). However, the calculated circulation in VAWT cluster tends to have large error due to the complication of the flow field near the rotor. Therefore, in this study, the rotor performances like the angular velocity ω_k, torque Q_k, and output power P_k are calculated using the initial circulation through the relations obtained by the CFD analysis of an isolated single rotor, which will be explained in Chapter 3

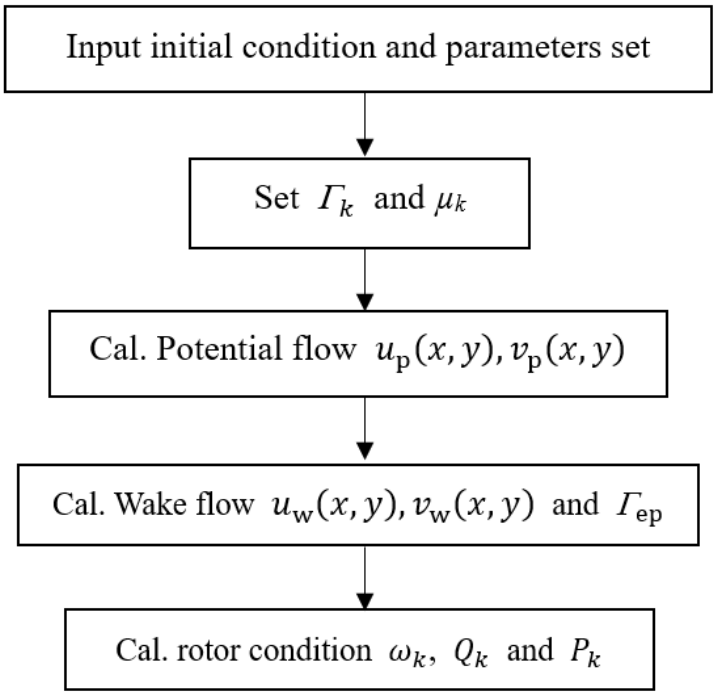

Fig. 2.6 Rough procedure for simulating the flow field and the rotor performances

2.2.8 Comparisons of the flow field of a Single rotor between the model and CFD

Figure 2.7 shows an example of the flow field obtained by the proposed wake model, which is compared with the averaged flow obtained by the CFD analysis. The rotor, the details will be explained in Chapter 3, is expressed by a circle in Fig. 2.7. The left-hand side in Fig. 2.7 shows the *x*-component distributions and the right-hand side the *y*-component distributions, which are calculated assuming the reference upstream flow speed of 10 m/s. The appearance of the distributions of both velocity components obtained by the model coincides that of the CFD analysis. The velocity profiles of the *x*- and *y*-components at x_n =

2 and 4 are compared between the model and CFD in Fig. 2.8a and Fig. 2.8b, respectively. It is clear that the proposed wake model can mimic the CFD-created flow filed very well in the case of an isolated single rotor. In addition to the flow velocity distributions, the rotational speed and output power of the single rotor can be predicted well: i.e., in this example, the wake model predicts the rotor speed of 3463 rpm and the power of 180.31 mW, which are almost the same as the CFD results of 3496 rpm and 177.62 mW.

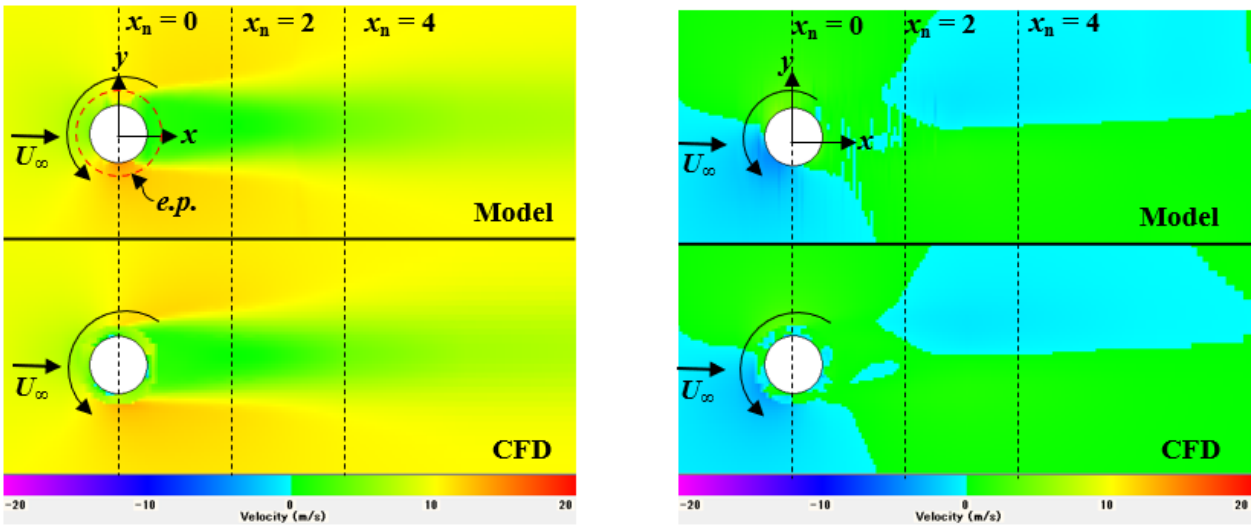

(a) x-component (u) (b) y-component (v)

Fig. 2.7 Distributions of the flow velocity around an isolated single rotor (U_∞ = 10 m/s)

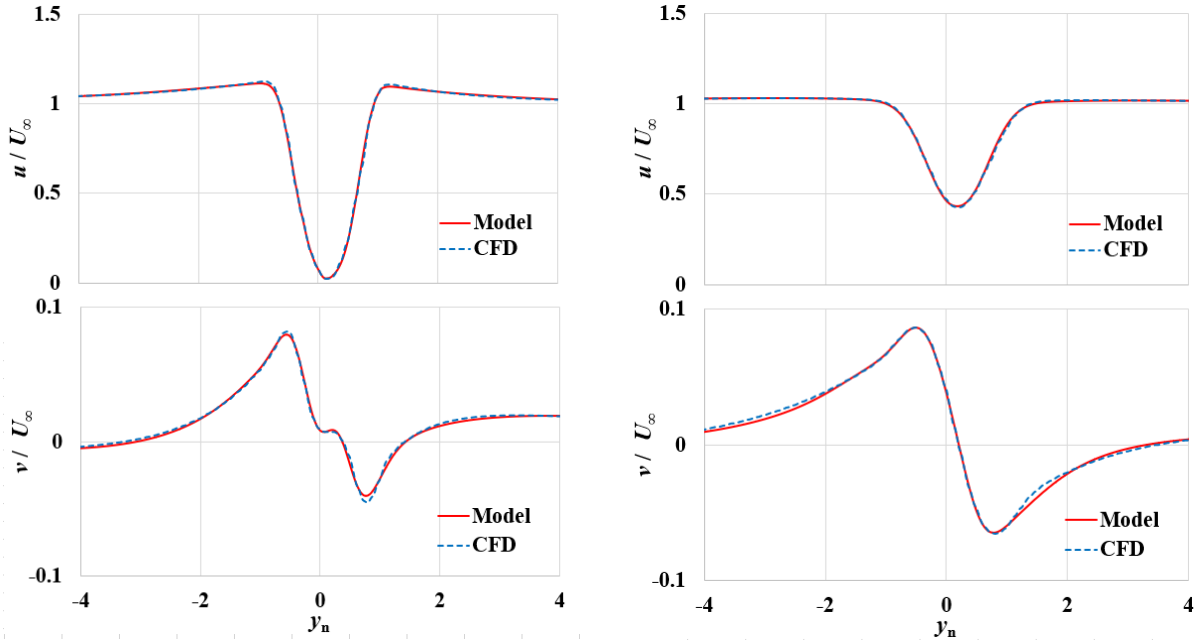

(a) $x_n = 2$ (b) $x_n = 4$

Fig. 2.8 Comparison of the velocity profiles in the wake of a single rotor between the proposed wake model and CFD

2.2.9 Comparisons of the flow field of a rotor pair between the model and CFD

In this section, the results of the flow field around a pair of co-rotating rotors are illustrated, as an example, to show the effects of the interaction model introduced in Section 2.2.6. All the results obtained by the present model shown in this section are calculated under the conditions of the upstream wind speed of 10 m/s and the same initial (or input) circulations as the circulations calculated from the compared CFD-created flow field. Figures 2.9 and 2.11 show the distributions of each component of the flow velocity which are obtained by

the wake model without interaction effects, including the CFD results for comparison. Figures 2.10a and 2.12a show the velocity profiles obtained by the model and CFD at $x_n = 2$ of x-component: u and y-component: v, respectively. Similarly, Figs 2.10b and 2.12b show the comparisons of the velocity profiles at $x_n = 4$ between the model and CFD. These comparisons shown in Figs. 2.9–2.12 make clear that the results obtained by the model without the interaction effects are very different from the CFD-created flow around a rotor pair.

With the same manner as Figs. 2.9–2.12, Figs. 2.13–2.16 show the results including the interaction effects when setting $\beta_1 = 0.5, \beta_2 = 2.0,$ and $\beta_3 = 0.15$. The wake shape and velocity profiles clearly approach the CFD results by including the interaction effects between the rotors, although some differences remain.

In addition, the circulation of each rotor, which is obtained by integrating the flow field created by the model considering the interaction effects, is different from that of the initial value or the CFD analysis. In this example, the circulations obtained from the model flow field are 0.288 for the upper rotor (R1) and 0.337 for the lower rotor (R2), which are –11.89 % and –3.74% of those of the CFD analysis, respectively.

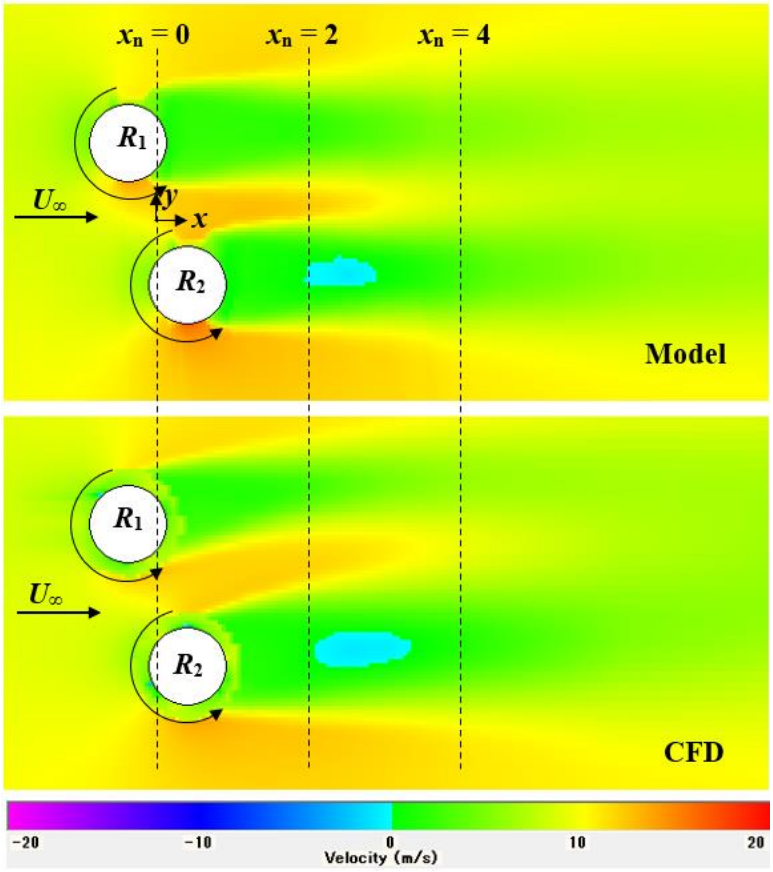

Fig. 2.9 Distributions of the flow velocity (x-component: u) around a pair of rotors (without interaction effects, U_∞ = 10 m/s)

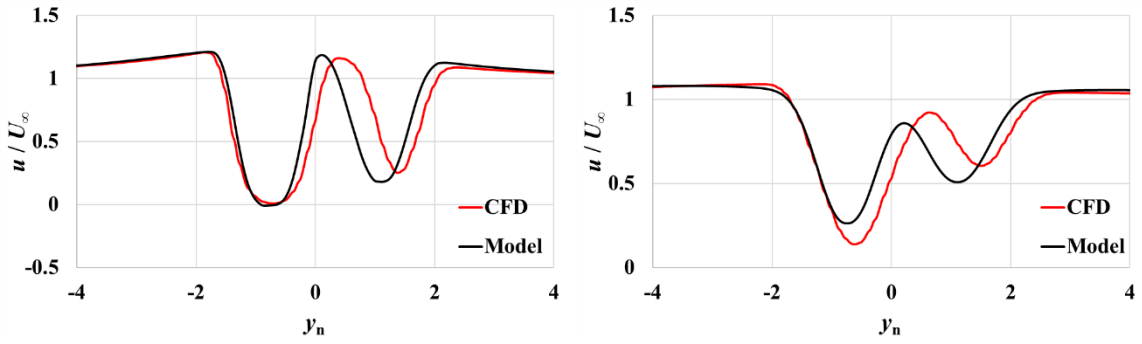

(a) $x_n = 2$ (b) $x_n = 4$

Fig. 2.10 Comparison of the velocity profiles (x-component: u) around a pair of rotors between the present model and CFD (without interaction effects, U_∞ = 10 m/s)

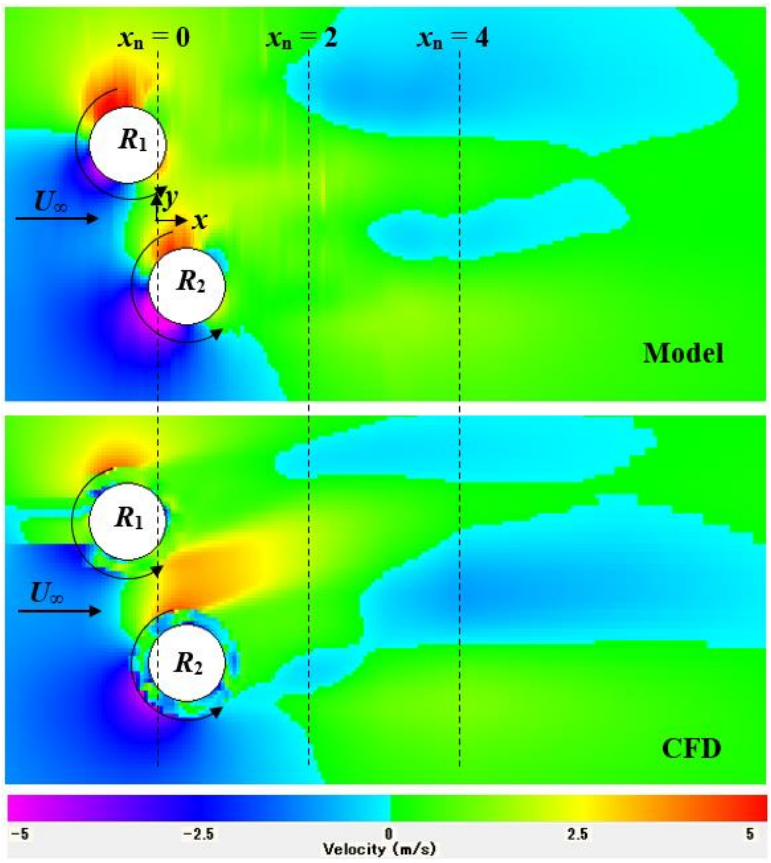

Fig. 2.11 Distributions of the flow velocity (y-component: v) around a pair of rotors (without interaction effects, U_∞ = 10 m/s)

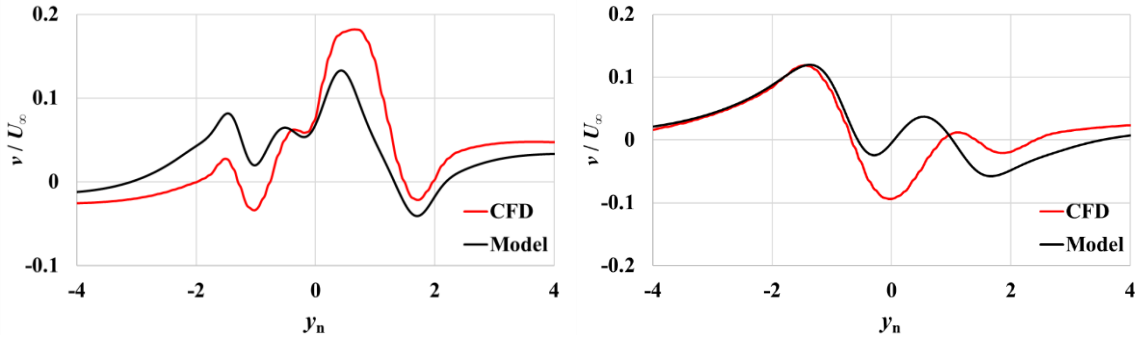

(a) $x_n = 2$ (b) $x_n = 4$

Fig. 2.12 Comparison of the velocity profiles (y-component: v) around a pair of rotors between the present model and CFD (without interaction effects, U_∞ = 10 m/s)

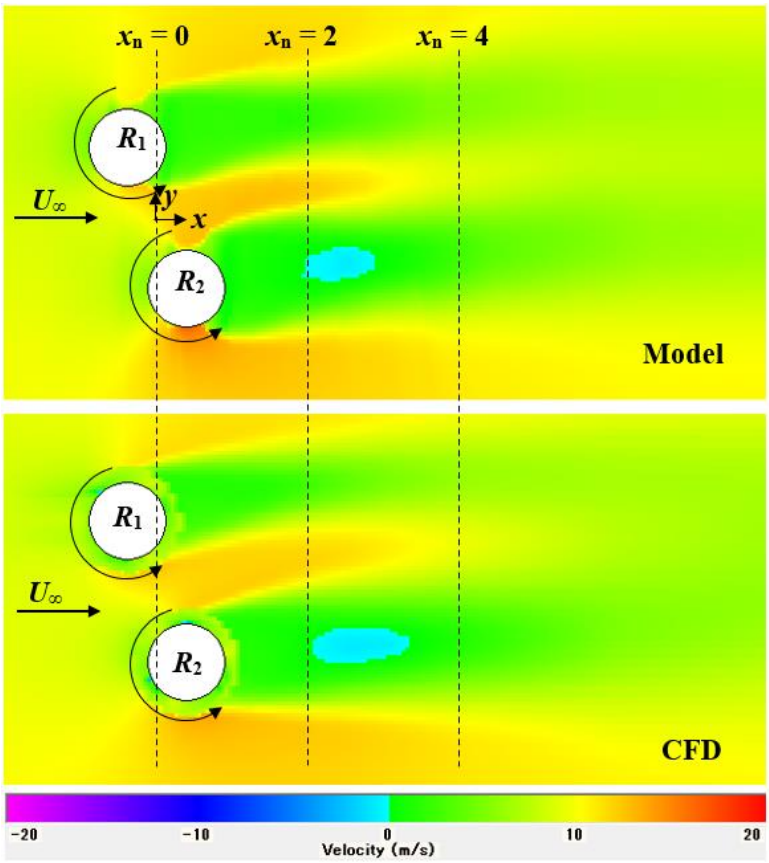

Fig. 2.13 Distributions of the flow velocity (x-component: u) around a pair of rotors (with interaction effects, U_∞ = 10 m/s)

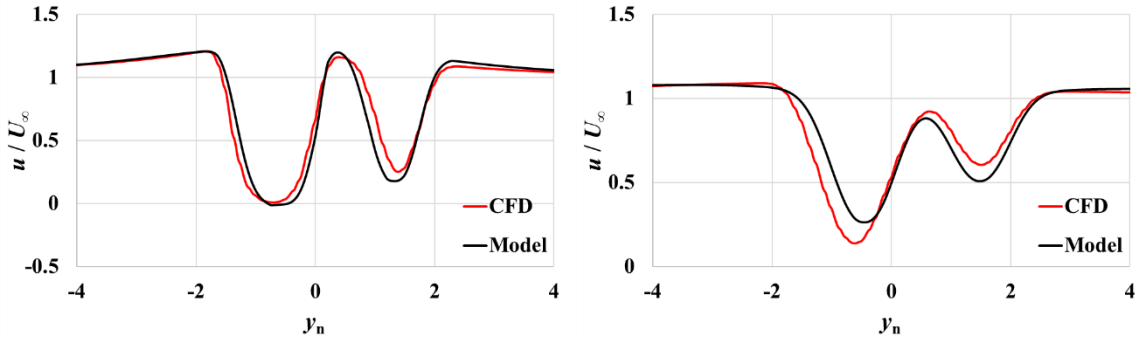

(a) $x_n = 2$ (b) $x_n = 4$

Fig. 2.14 Comparison of the velocity profiles (x-component: u) around a pair of rotors between the present model and CFD (with interaction effects, U_∞ = 10 m/s)

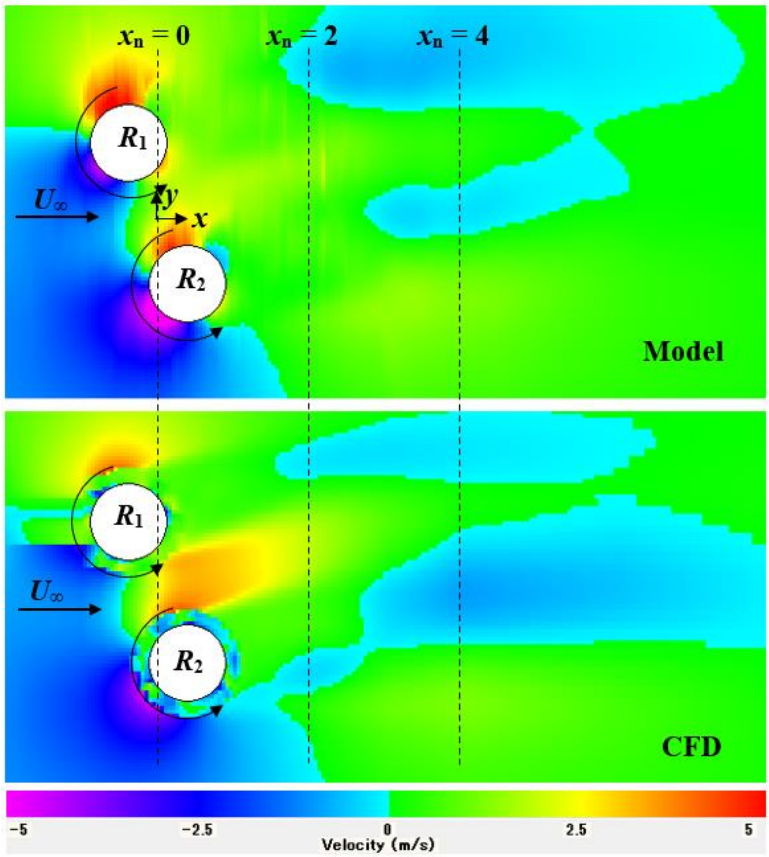

Fig. 2.15 Distributions of the flow velocity (y-component: v) around a pair of rotors (with interaction effects, U_∞ = 10 m/s)

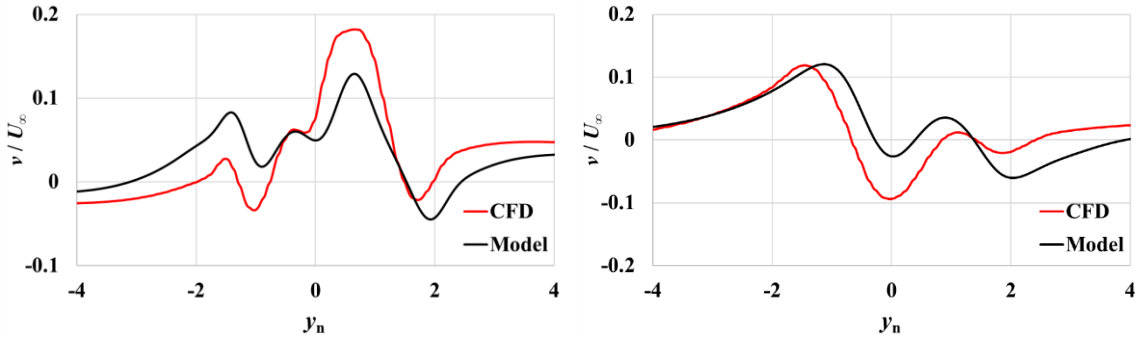

(a) $x_n = 2$ (b) $x_n = 4$

Fig. 2.16 Comparison of the velocity profiles (y-component: v) around a pair of rotors between the present model and CFD (with interaction effects, U_∞ = 10 m/s)

2.3 Method to find out an appropriate state of a VAWT cluster

In section 2.2, it was shown that the proposed wake model including the interaction effects caused by the induced velocity can mimic the CFD-created flow field if adequate initial value set of circulations and blockages are given. However, to simulate the VAWT wind farm or cluster, it is necessary to determine the adequate set of input values. In this section, the method to find out an appropriate state of a VAWT cluster, or to determine the appropriate input values of circulations and blockages of the rotors in the VAWT cluster.

2.3.1 Momentum conservation

In the 2D-CFD analysis which the presents wake model mimics, the mass conservation and the momentum conservation are satisfied. In this study, the momentum conservation in the *x*-direction is used to determine an appropriate state of a VAWT cluster as a result of preparatory investigations. Figure 2.17 shows a schematic image of a control volume (CV) used for the calculation of the flow field around an isolated single rotor, as an example. In Fig. 2.17, the relevant forces acting on the fluid in the CV and the momentum flows in relation to the momentum conservation in the *x*-direction are illustrated.

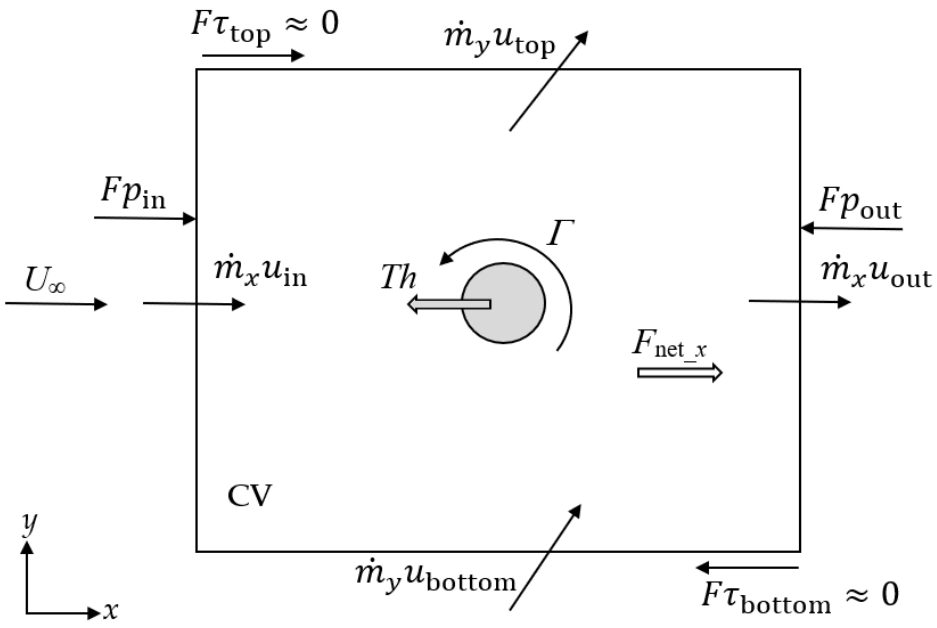

Fig. 2.17 Schematic image showing the momentum flows and relevant forces in the *x*-direction of the control volume (CV) in the case of an isolated single rotor

The prepared data of an isolated single rotor, regardless of CFD data or experimental data, must satisfy the Newton's equation of motion like Eq. (2.25) regarding the *x*-direction. The left-hand side of Eq. (2.25) is the total force acting on the fluid in the *x* direction (main flow direction) and the right-hand side shows the variation in the momentum in the *x* direction per unit time. The variation in the momentum $\Delta(\dot{m}u_x)$ is calculated from the flow velocity at the boundaries of CV by Eq. (2.26), in which the mass flow rate $\dot{m}_x$ and $\dot{m}_y$ are expressed by $\rho u dy$ and $\rho v dx$, respectively. Here, ρ is the air density; dx and dy are small boundary elements. The total force $F_{\mathrm{net\_}x}$ is given by Eq. (2.27), in which the pressure forces Fp_{in} and Fp_{out} acting on the inlet and outlet boundaries are considered and are calculated by the integration along each boundary. The Fp in Eq. (2.27) shows the total pressure force in the

x-direction and means the pressure loss. The forces ($F_{\_\tau\_\text{top}}$, $F_{\_\tau\_\text{bottom}}$) caused by shear stress on the top and bottom boundaries are neglected in this study. From Eqs. (2.25) and (2.27), the relation of Eq. (2.28) is obtained for an isolated single rotor. In the method proposed here, the pressure loss *Fp* has to be prepared as a function of the upstream speed or the corresponding circulation of a single rotor for an applied CV. Note that the pressure loss *Fp* cannot be calculated from the model flow field obtained by using Eq. (2.4) and Eq. (2.16).

$$F_{\text{net\_}x} = \Delta(\dot{m}u_x) \tag{2.25}$$

$$\Delta(\dot{m}u_x) = -\int \dot{m}_x u_{in} + \int \dot{m}_x u_{out} - \int \dot{m}_y u_{bottom} + \int \dot{m}_y u_{top} \tag{2.26}$$

$$F_{\text{net\_}x} = -Th + \int p_{\text{in}} dy - \int p_{\text{out}} dy = -Th + Fp_{\text{in}} - Fp_{\text{out}} = -Th + Fp \tag{2.27}$$

$$\Delta(\dot{m}u_x) = -Th + Fp \tag{2.28}$$

To apply the momentum balance given by Eq. (2.28) to VAWT cluster, an evaluation function *Err* is defined by Eq. (2.29),

$$Err = \Delta(\dot{m}u_x) + \sum_k Th_k - \sum_k fp_k\, Fp_k \tag{2.29}$$

where Th_k and Fp_k are the thrust force and pressure loss caused by the k-th rotor under the condition of an isolated single rotor, respectively. Th_k and Fp_k are calculated using the input

value of circulation (Γ_k) based on the prepared information for an isolated single rotor. fp_k is the correction function introduced to express the interaction caused by the superposition of wakes between the *k*-th rotor and other rotors and is defined by Eq. (2.30), in which I_j is a function expressing the interaction strength (or intensity) from the *j*-th rotor to the *k*-th rotor.

$$fp_k = 1 - \sum_{j \neq k} I_j \tag{2.30}$$

In this method, the blockage μ_k of each rotor is related to the circulation Γ_k through the relation obtained from the isolated single rotor performance which will be explained in Chapter 3. The effects of the blockages, as well as the circulations, on the flow field are included in the variation of the momentum $\Delta(\dot{m}u_x)$ and are reflected on the momentum conservation in the *x*-direction

2.3.2 Categorization of rotor pair layouts

Before proceeding the detailed description of the interaction functions I_j, the categorization of the layout of a paired rotor is explained in this section. There are four typical layouts of two 2D-VAWT rotors as shown in Fig. 2.18; i.e., the co-rotating (CO), counter-down (CD), counter-up (CU), and tandem (TD). The three layouts of CO, CD, and CU are the side-by-side arrangements. On the other hand, the layouts of TD include two kinds of arrangements, co-rotating or inverse rotating, of two rotors in line parallel to the main flow. An arbitrary rotor pair selected in the calculation process has a different layout from the

typical aforementioned layouts. However, in this study, an arbitrary rotor pair is categorized roughly into the four gropes, i.e., CO-like, CD-like, CU-like, and TD-like layouts.

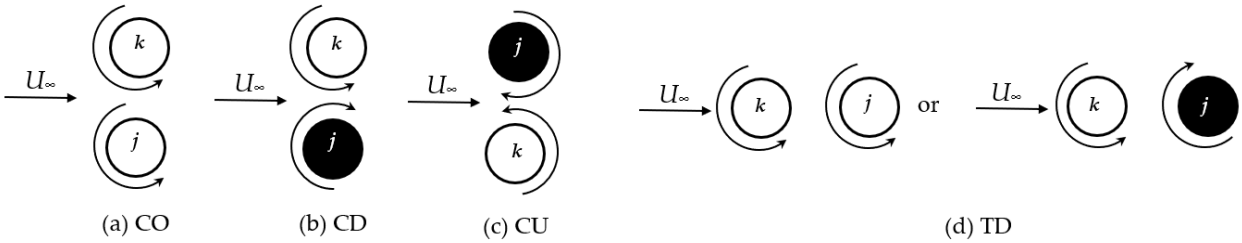

Fig. 2.18 Four categories of the layouts between the selected two rotors: (a) co-rotating (CO); (b) counter-down (CD); (c) counter-up (CU); (d) tandem (TD)

2.3.3 Interaction function

In this method, the interaction function I_j is defined separately for each category of the selected two-rotor layout as shown in Eq. (2.31) to Eq. (2.34). φ_j is defined as the angle between the direction seeing from the *k*-th rotor to the *j*-th rotor and the upwind direction as shown in Fig. 2.19. r_{jk} is the distance between the centers of the two rotors. A constant angle γ_1 divides the CV into two zones, i.e., the wake zone (in grey) and the out of wake zone (in white). If the *j*-th rotor (counterpart to the *k*-th rotor) exists in the wake zone, Eq. (2.34) is used to calculate of the interaction function I_j as the TD-like layout. When the counterpart rotor exists in the out of wake zone, the equation used for the calculation of the interaction function I_j is determined as one of three Eq. (2.31) to Eq. (2.33) according to the corresponding layout category of the two rotors. The fitting parameters of α_1, α_2, α_3, and α_4

are introduced so as to obtain a sufficient correspondence between the results of rotor power prediction using the model and the CFD analysis, in the specific four conditions of paired rotors, i.e., CO, CD, CU, and TD layouts.

$$I_j = \alpha_1 \frac{|\Gamma_j|}{\Gamma_{SI}} |\sin\varphi_j| \left(\frac{D}{r_{jk}}\right)^2 \quad ; \text{for CO-like} \tag{2.31}$$

$$I_j = \alpha_2 \frac{\Gamma_j}{\Gamma_{SI}} \sin\varphi_j \left(\frac{D}{r_{jk}}\right)^2 \quad ; \text{for CD-like} \tag{2.32}$$

$$I_j = \alpha_3 \frac{\Gamma_j}{\Gamma_{SI}} \sin\varphi_j \left(\frac{D}{r_{jk}}\right)^2 \quad ; \text{for CU-like} \tag{2.33}$$

$$I_j = \alpha_4 \frac{|\Gamma_j|}{\Gamma_{SI}} \cos\varphi_j \left(\frac{D}{r_{jk}}\right)^2 \quad ; \text{for TD-like} \tag{2.34}$$

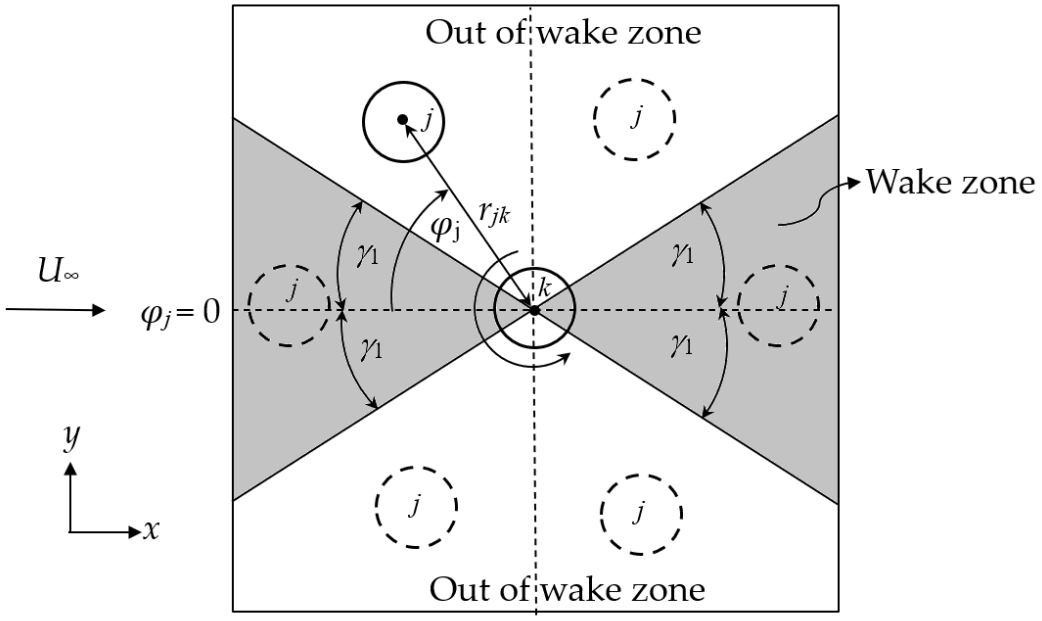

Fig. 2.19 Definitions of the angle φ_j of the selected two rotors and the wake zone.

2.3.4 Procedure to find out an appropriate state

The flow chart of the method is shown in Fig. 2.20. Before starting the calculation, the relations, such as between the circulation and rotor output, and the fitting parameters must be prepared from the information of an isolated single rotor and four specific conditions (i.e., CO, CD, CU, and TD layouts) of two rotors. At first, the calculation conditions such as the upstream wind speed (U_∞), the positions of the rotors, and the rotational directions are input. Then, the process of searching for a reasonable combination of circulations is initiated starting from the lowest value of the circulation in a given searching range for each rotor. With a given combination of circulations, the potential flow is calculated first and it is modified by the proposed wake model to include the effects of the velocity deficits. With the flow field (u_w, v_w) obtained, the momentum changes in the x-direction per unit of time $\Delta(\dot{m}u_x)$ is calculated from the four boundary conditions. The thrust force Th_k and the (isolated single rotor) pressure loss Fp_k are calculated using the given circulation value for each rotor. Using the interaction function I_j given by one of Eqs. (2.31)–(2.34), the correction function fp_k, which expresses the effects of the inter-rotor interaction, is obtained for each rotor by Eq. (2.30). Then, the momentum balance Err is evaluated by Eq. (2.29). The "*error*" of momentum balance is defined in Eq. (2.35) in the present study. The denominator in Eq. (2.35) is the momentum per unit time entering into the CV from the inlet boundary.

$$error = \frac{\sqrt{Err^2}}{\int \dot{m}_x u_\mathrm{in}} \tag{2.35}$$

The above calculation is repeated by changing the combination of circulations with the interval of $\Delta\Gamma$ throughout all the searching ranges. After the round robin, a combination of circulation Γ_k which gives the smallest "*error*" is obtained. In the present study, the similar searching process (sub-searching) is repeated twice by narrowing the searching ranges as $(\Gamma_k - \Delta\Gamma) \leq \Gamma_{k\_i} \leq (\Gamma_k + \Delta\Gamma)$. Finally, for the smallest "*error*" condition, the power output of each rotor can be obtained.

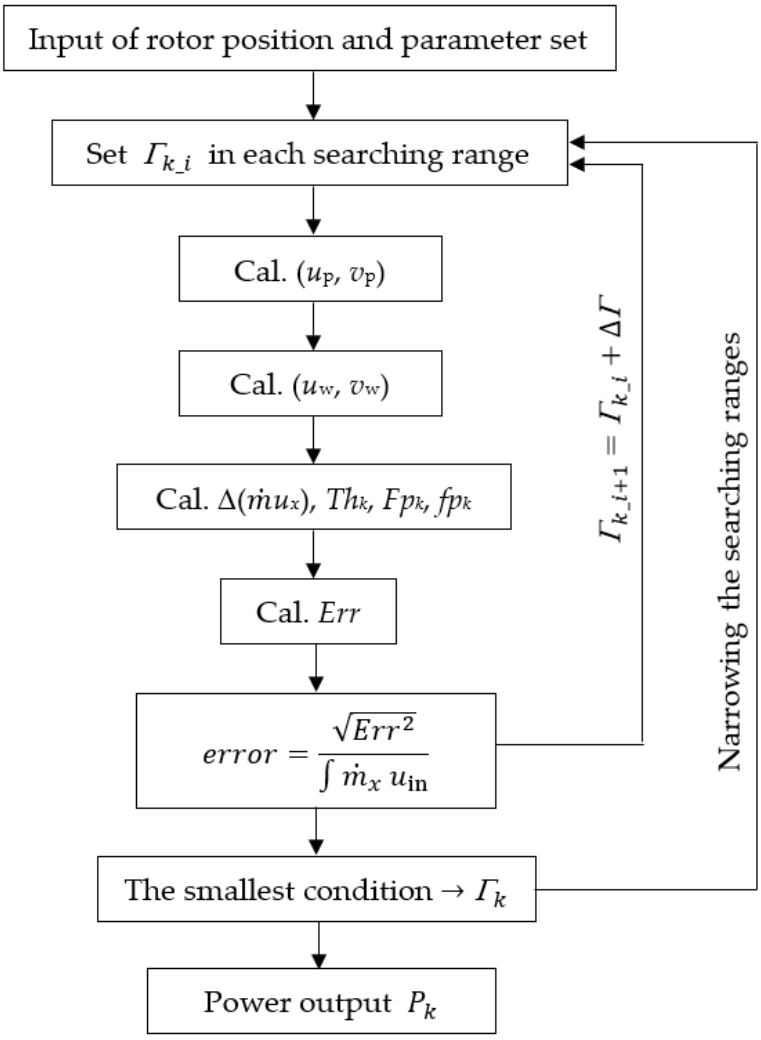

Fig. 2.20 The flow chart of the method

2.3.5 Selection of the searching range of circulation

An example of a small rotor pair in CO layout is considered in this section to explain the selection of the searching range to obtain the adequate circulations. The values of α_1, α_2, α_3, and α_4 in Eqs. (2.31)–(2.34) are determined as 0.2304, 0.19, −0.2853, and 1.07, respectively, from the preliminary calculations of the specific four layouts of paired rotors. The CV is defined as $20D \times 20D \times 0.868D$. The thickness of the CV given by $0.868D$ corresponds to the rotor height of the target rotor of this example.

Figures 2.21a and 2.22a show the averaged distributions of the *x*- and *y*-component velocities calculated by the CFD analysis around two rotors rotating in the counterclockwise (CCW) direction. The circulation of the upper rotor (rotor-*k*) is 0.334 m^2/s, which was obtained by the integration of flow field along a circle path at r/D = 0.75 (e.p.). The circulation of the lower rotor (rotor-*j*) is 0.345 m^2/s. The details of the rotor shape are not shown but are replaced by circles in white in Figs. 2.21a and 2.22a. The black solid lines around the rotors are path lines which are calculated by assuming several artificial particles.

Figures 2.21b and 2.22b are the resultant flow field obtained by the proposed method using an in-house code, in which the circulation of each rotor was changed step by step in a round robin over a wide searching range from $0.1\Gamma_{SI}$ to $1.1\Gamma_{SI}$. Here, Γ_{SI} is the circulation of an isolated single rotor obtained from the CFD analysis and the value is 0.326 m^2/s in this example. The obtained circulations of two rotors in Figs. 2.21b or 2.22b are Γ_k = 0.072 m^2/s and Γ_j = 0.037 m^2/s, respectively, and they are different from the CFD results in Figs. 2.21a or 2.22a. To illustrate the variation in the error of momentum balance graphically, a new

indicator (1 – *error*) is defined, which approaches 1 when the error becomes small. The distribution of the values of (1 – *error*) obtained in the searching process that resulted in the condition of Fig. 2.21b is shown in Fig. 2.23, which includes 625 results corresponding to the combinations of circulation values (Γ_j, Γ_k) with the interval of (1.1 - 0.1) Γ_{SI}/25. Figure 2.23 shows that there are a lot of combinations of circulation, i.e., false solutions, which might give a small error, if a wide searching range of circulation is used inappropriately.

In the parallel layouts (CO, CD, and CU), it is expected that two rotors have large circulations close to the value of Γ_{SI}. Therefore, the searching range can be narrowed. Figure 2.21c and 2.22c are the flow field obtained using a searching range limited from $0.95\Gamma_{SI}$ to $1.1\Gamma_{SI}$ for each rotor in the CO layout. The circulation combination giving the smallest error, shown in Fig. 2.21c, are Γ_k = 0.337 m^2/s and Γ_j = 0.349 m^2/s, respectively. Figure 2.24 is the distribution of the 625 values of (1 – *error*) obtained in the searching process with the limited range from $0.95\,\Gamma_{SI}$ to $1.1\,\Gamma_{SI}$ for each rotor. The results obtained with an appropriately limited searching ranges can approach the CFD results.

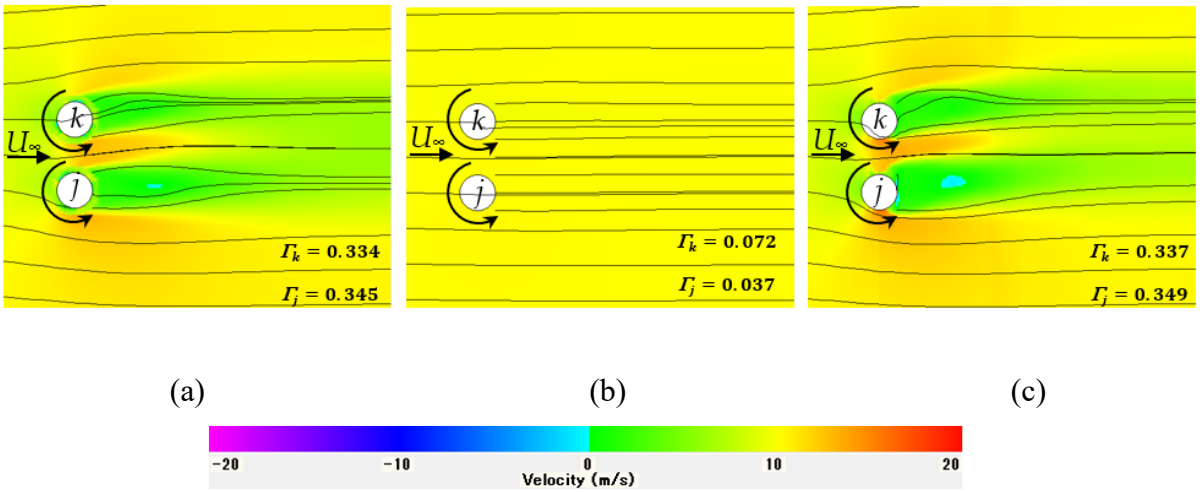

Fig. 2.21 The distribution of the *x*-component velocity around two rotors in the CO layout: (a) CFD; (b) model with a wide searching range; (c) model with a narrow searching range

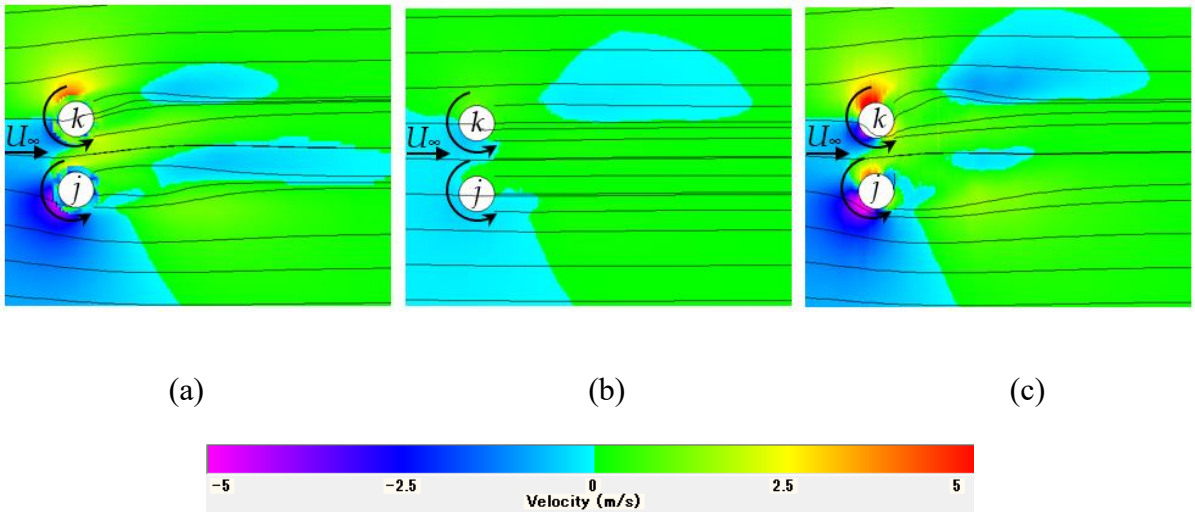

Fig. 2.22 The distribution of the *y*-component velocity around two rotors in the CO layout: (a) CFD; (b) model with a wide searching range; (c) model with a narrow searching range

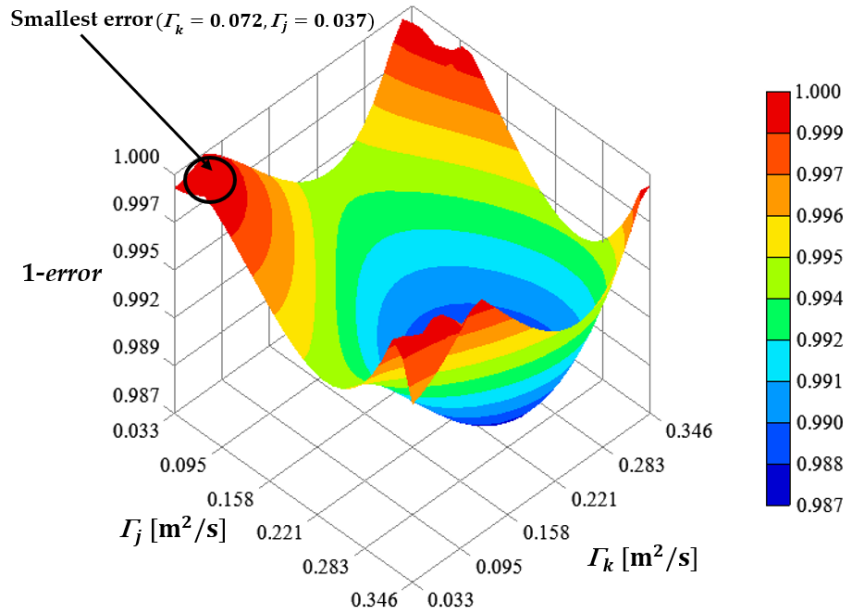

Fig. 2.23 Three-dimensional chart showing the distribution of the value of 1– *error* in the model calculation of two rotors in the CO layout with the wide searching range from $0.1\Gamma_{SI}$ to $1.1\Gamma_{SI}$

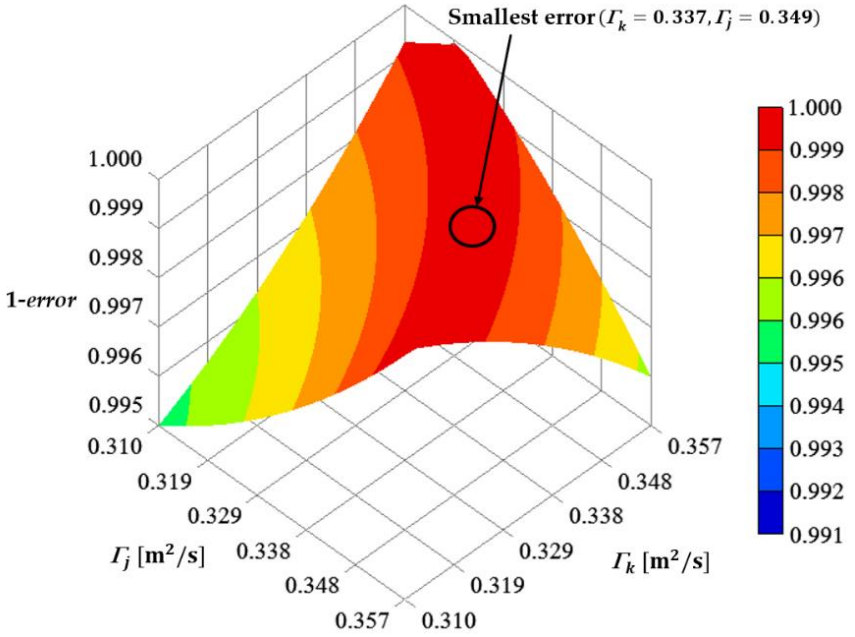

Fig. 2.24 Three-dimensional chart showing the distribution of the value of 1– *error* in the model calculation of two rotors in the CO layout with the wide searching range from $0.95\Gamma_{SI}$ to $1.1\Gamma_{SI}$

Incorrect results are also obtained when the rotor at issue exists in the wake of other rotors if the wide searching range of circulation is applied. To predict an appropriate rotor state close to the CFD result, this study proposes the following procedure to limit the searching range of circulation of each rotor in a VAWT cluster.

In the procedure, a circular interaction region of the radius R_{int} is defined around a rotor (k) at issue. Let's assume that there are N_{int} rotors in the region. Only the rotors (j) included in the interaction region are considered and are used to decide the searching range of circulation of the rotor (k).

First of all, the angle φ_j defined in Fig. 2.19 is checked for the all rotors in the interaction region. If the absolute value of one of the angles is less than a constant angle γ_2, the searching range expressed by Eq. (2.36) is applied. Note that the angle γ_2 is different from the angle γ_1, and γ_2 is less than γ_1. The interaction region is determined to be a circle of $R_{\text{int}} = 10D$ in this specific calculation; therefore, the maximum of the inter-rotor distance r_{jk} is $10D$ in Eq. (2.36) in this study.

$$0.3\Gamma_{\text{SI}} \leq \Gamma_k < \left(0.075\frac{r_{jk}}{D} + 0.35\right)\Gamma_{\text{SI}} \quad ; \quad \text{for} \quad |\varphi_j| < \gamma_2 \tag{2.36}$$

In the second step of the procedure, the average distance d_j between the center of the j-th rotor and the stream-wise center line through the k-th rotor at issue is calculated with all the counterpart rotors of the k-th rotor in the interaction region using Eq. (2.37).

$$\overline{d_J} = \frac{\sum_{j \neq k} |d_j|}{N_{\text{int}} - 1} \tag{2.37}$$

In the third step of the procedure, the search range of the circulation Γ_k of the *k*-th rotor is determined as one of Eq. (2.38) to Eq. (2.40) according to the averaged lateral distance $\overline{d_J}$. Figure 2.25 shows schematically the definition of the angle γ_2 and three zones determining the search range of circulation of *k*-th rotor. The delimiting lateral distances are determined as $d_1 = 0.9D$ and $d_2 = 1.5D$ in this study.

$$0.85\Gamma_{\text{SI}} \leq \Gamma_k < 1.0\Gamma_{\text{SI}} \quad ; \quad \text{for} \quad 0 \leq \overline{d_J} < d_1 \tag{2.38}$$

$$0.9\Gamma_{\text{SI}} \leq \Gamma_k < 1.0\Gamma_{\text{SI}} \quad ; \quad \text{for} \quad d_1 \leq \overline{d_J} < d_2 \tag{2.39}$$

$$0.95\Gamma_{\text{SI}} \leq \Gamma_k < 1.1\Gamma_{\text{SI}} \quad ; \quad \text{for} \quad \overline{d_J} \geq d_2 \tag{2.40}$$

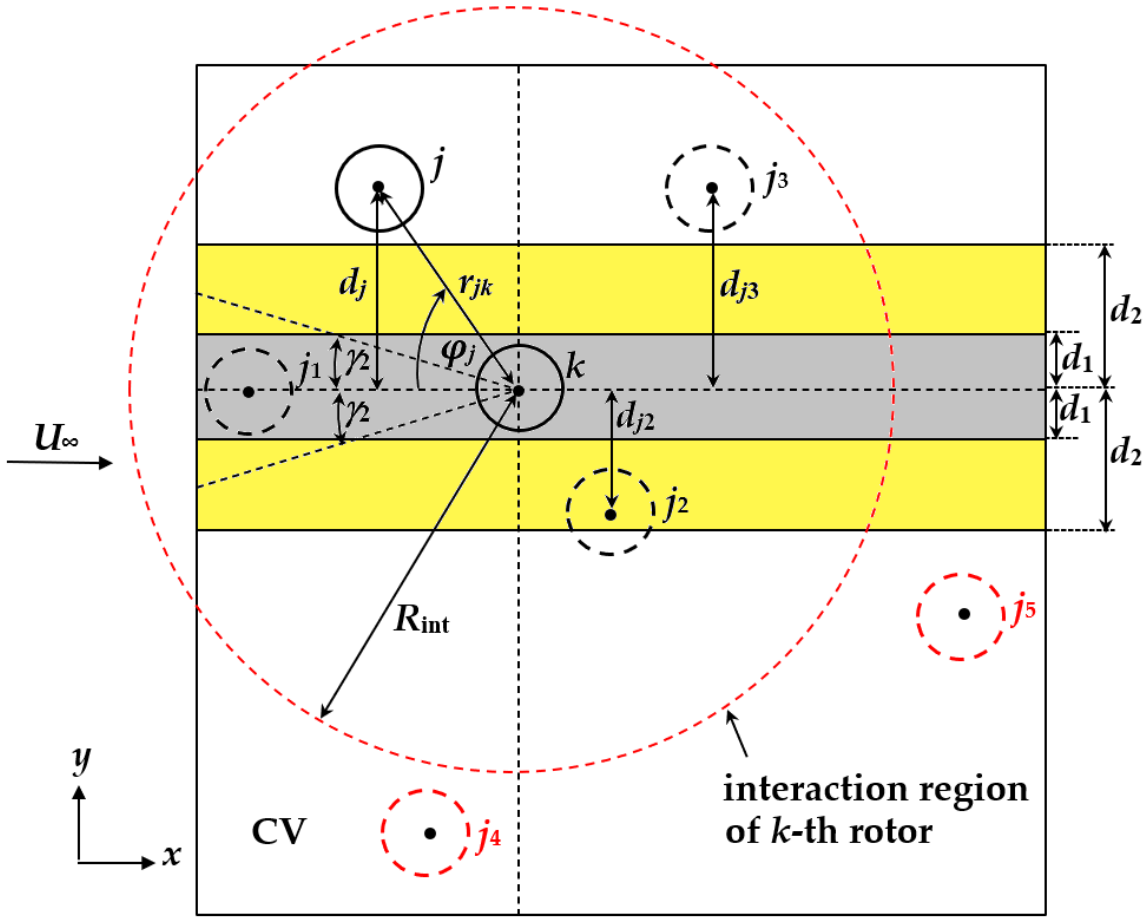

Fig. 2.25 Definition of the angle γ_2 and three zones (in grey, yellow, and white) determining the searching range of circulation of k-th rotor

References

[1] Whittlesey, R. W.; Liska S.; Dabiri, J. O. Fish schooling as a basis for vertical axis wind turbine farm design. *Bioinspiration & Biomimetics* 2010, 174, 1–59.

[2] Shapiro, C. R.; Starke, G. M.; Meneveau, C.; Gayme, D. F. A wake modeling paradigm for wind farm design and control. *Energies* 2019, 12, 2956.

[3] Hara, Y.; Jodai, Y.; Okinaga, T.; Furukawa, M. Numerical analysis of the dynamic interaction between two closely spaced vertical-axis wind turbines. *Energies* 2021, 14, 2286.

[4] Okinaga, T.; Hara, Y.; Yoshino, K.; Jodai, Y. Numerical simulation considering the variation in rotational speed of three closely spaced vertical-axis wind turbines. *In Proceedings of JWEA 43rd Wind Energy Utilization Symposium*, Tokyo, Japan, 18–19 November 2021.

Chapter 3

CFD analysis

3.1 Introduction

The wake model in this study is designed to mimic the flow field calculated by the computational fluid dynamics (CFD) and the results of CFD are also used to validate the accuracy of the model. This chapter describes the details of the CFD analysis used in this study, covering the target rotor, the governing equations, the computational mesh, and the boundary conditions. This chapter also explains the relations obtained by the CFD between the target rotor performance and the circulation, as well as the behavior of some important parameters used in the method described in Chapter 2.

3.2 Numerical method

3.2.1 Basic equations

The CFD analysis used in this study is two dimensional. The basic equations are the continuity equation shown in Eq. (3.1) and the unsteady incompressible Reynolds averaged Navier-Stokes (RANS) equations shown in Eqs. (3.2) and (3.3).

$$\mathrm{div}\,\boldsymbol{U} = 0 \tag{3.1}$$

$$\frac{\partial U}{\partial t} + \mathrm{div}(U\boldsymbol{U}) = -\frac{1}{\rho}\frac{\partial P}{\partial x} + \nu\,\mathrm{div}(\mathrm{grad}U) + \frac{1}{\rho}\mathrm{div}(-\rho\overline{u'\boldsymbol{u}'}) \tag{3.2}$$

$$\frac{\partial V}{\partial t} + \mathrm{div}(V\boldsymbol{U}) = -\frac{1}{\rho}\frac{\partial P}{\partial y} + \nu\,\mathrm{div}(\mathrm{grad}V) + \frac{1}{\rho}\mathrm{div}(-\rho\overline{v'\boldsymbol{u}'}) \tag{3.3}$$

In Eqs. (3.1)–(3.3), $\boldsymbol{U} = (U, V)$ is the two-dimensional averaged velocity vector, and $\boldsymbol{u}' = (u', v')$ is the turbulent velocity vector. $-\rho\overline{u'\boldsymbol{u}'}$ and $-\rho\overline{v'\boldsymbol{u}'}$ show the Reynolds stress. P is the averaged pressure, ρ is the air density, and ν is kinematic viscosity.

The SST k–ω is used as the turbulence model [1]. The CFD analysis in this study uses the dynamic fluid/body interaction (DFBI) model [2] to simulate the change in the rotational speed of each rotor. Therefore, the moment of inertia (I) of each rotor with unit height is input into the CFD solver to solve the equation of motion about each rotor (see Eq. (3.4)). Q_R and Q_L in Eq. (3.4) are the rotor torque and load torque, respectively. As the CFD solver, the STAR-CCM+ is utilized in this study.

$$I\frac{d\omega}{dt} = Q_R - Q_L \tag{3.4}$$

3.2.2 Rotor configuration

In this study, the wind turbine rotor is assumed to be the three-bladed two-dimensional rotor used in Hara et al. [2] (see Fig. 3.1). The rotor diameter is D = 0.05 m, the chord length is c = 0.02 m and blade cross section: NACA 0018. The moment of inertia is set to be I = 1.284 $.10^{-4}$ kgm^2 for a rotor with a unit height in CFD analysis. The wind turbine rotors are assumed to be controlled according to the ideal load torque curve (Q_L =3.71×10^{-9} ω^2 (Nm)) shown in Fig. 3.2. Note that the torque curves shown in Fig. 3.2 are converted to the equivalent values to the experimental rotor with the height of 43.4 mm [2]. As described here, the proposed method postulates that the rotor operating conditions are known for the several wind speed conditions.

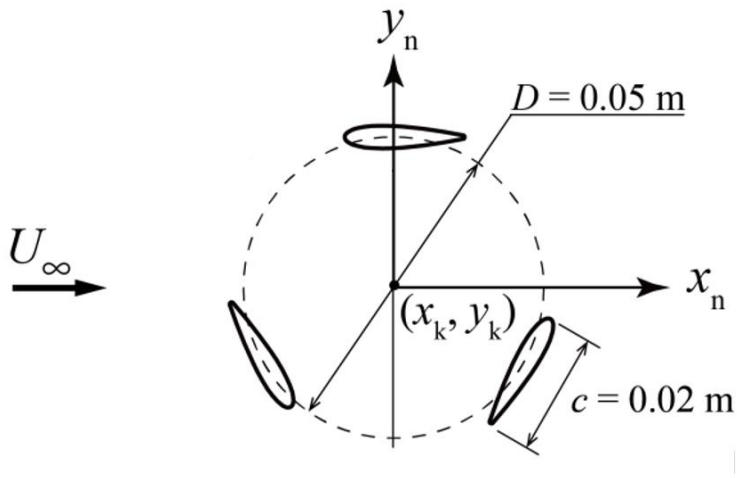

Fig. 3.1 Two-dimensional rotor (Hara et al. [2])

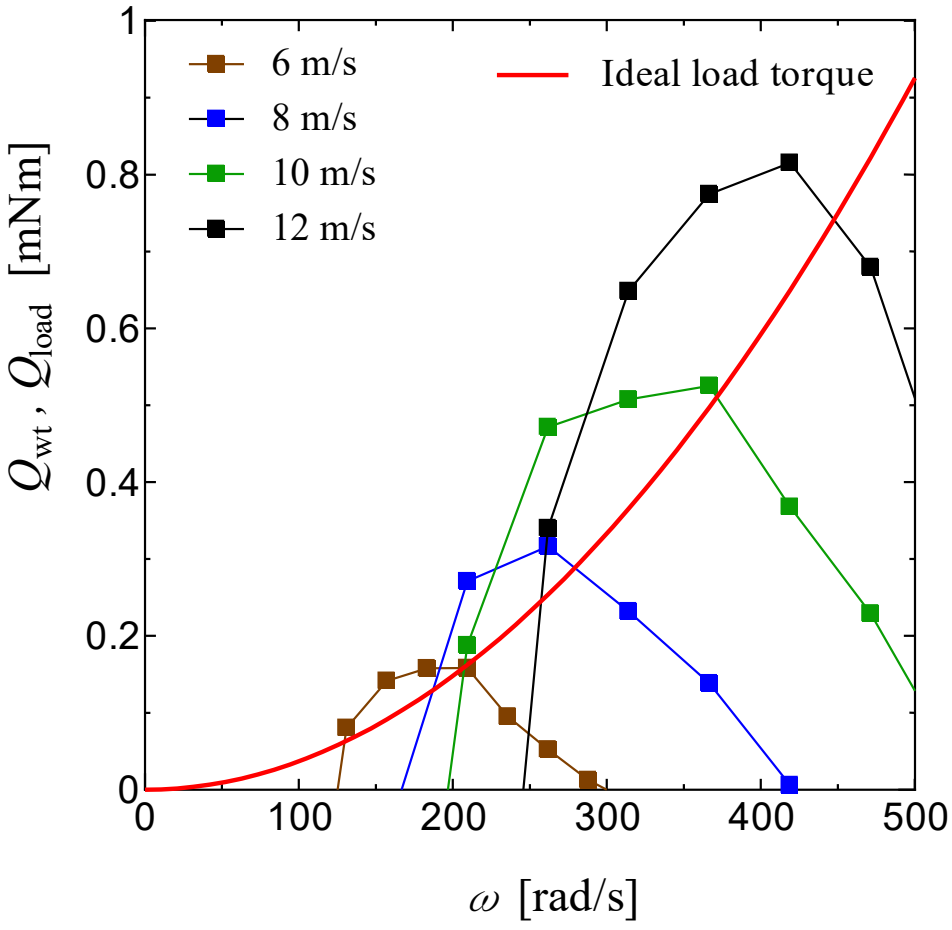

Fig. 3.2 Rotor torque curves and ideal load torque curve of a two-dimensional rotor equivalent to the experimental rotor with the height of 43.4 mm. (Hara et al. [2])

3.2.3 Computation mesh

The computation meshes used in the CFD analysis in this study for a single rotor, a pair of rotors and three rotors are shown in Fig. 3.3. The size of the whole domain is $80D \times 100D$. The center of the upstream rotor is located at $40D$ from the inlet boundary. Figure 3.4 shows the mesh around a single rotor (Fig. 3.4a), a pair of rotors (Fig. 3.4b) and three rotors (Fig. 3.4c). The distance between the centers of the adjacent rotors is equal to $2D$ in the case of a pair of rotors and three rotors (i.e., inter-rotor $gap = 1D$). The total number of cells is 198,839 in the case of a single rotor, 285,895 in the case of a pair of rotors and 372,641 in the case of three rotors. Figures 3.5a and 3.5b show the whole domains of the parallel and tandem layouts, respectively. The size of the whole domain is $80D \times 100D$. The center of each four-rotor array is located at $40D$ from the inlet boundary. Figures 3.5c and 3.5d show the mesh around the rotors of the parallel and tandem layouts, respectively. The distance between the centers of the adjacent rotors is equal to $4D$ (i.e., inter-rotor $gap = 3D$). Figures 3.5e and 3.5f show the details of the mesh created around a rotor and a blade, respectively. These mesh sizes are the same as that used for the CFD analysis of one-, two-, and three-rotor arrangements. The total number of cells is 593,880 in the case of the four-rotor parallel layout and 473,725 in the case of the four-rotor tandem layout.

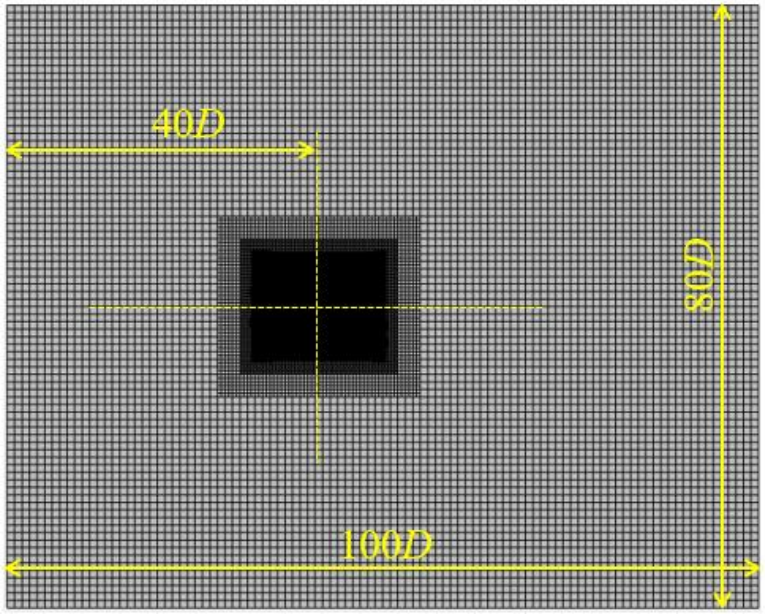

Fig. 3.3 Computation meshes used in the CFD analysis in this study, whole domain of a single rotor, a pair of rotors and three rotors

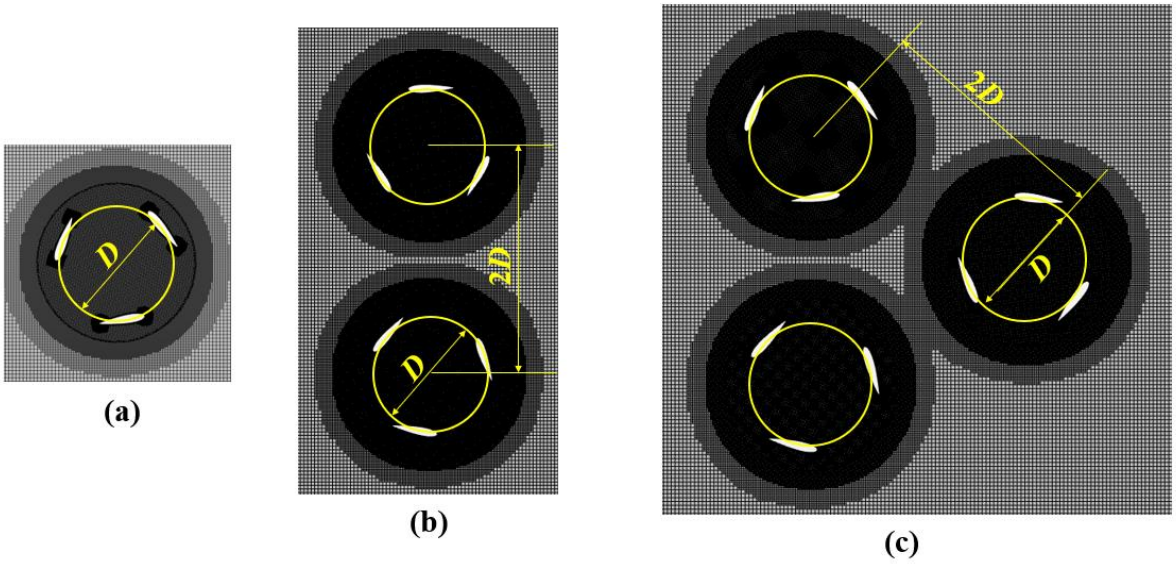

Fig. 3.4 Mesh around the rotor: (a) a single rotor; (b) a pair of rotors; (c) three rotors

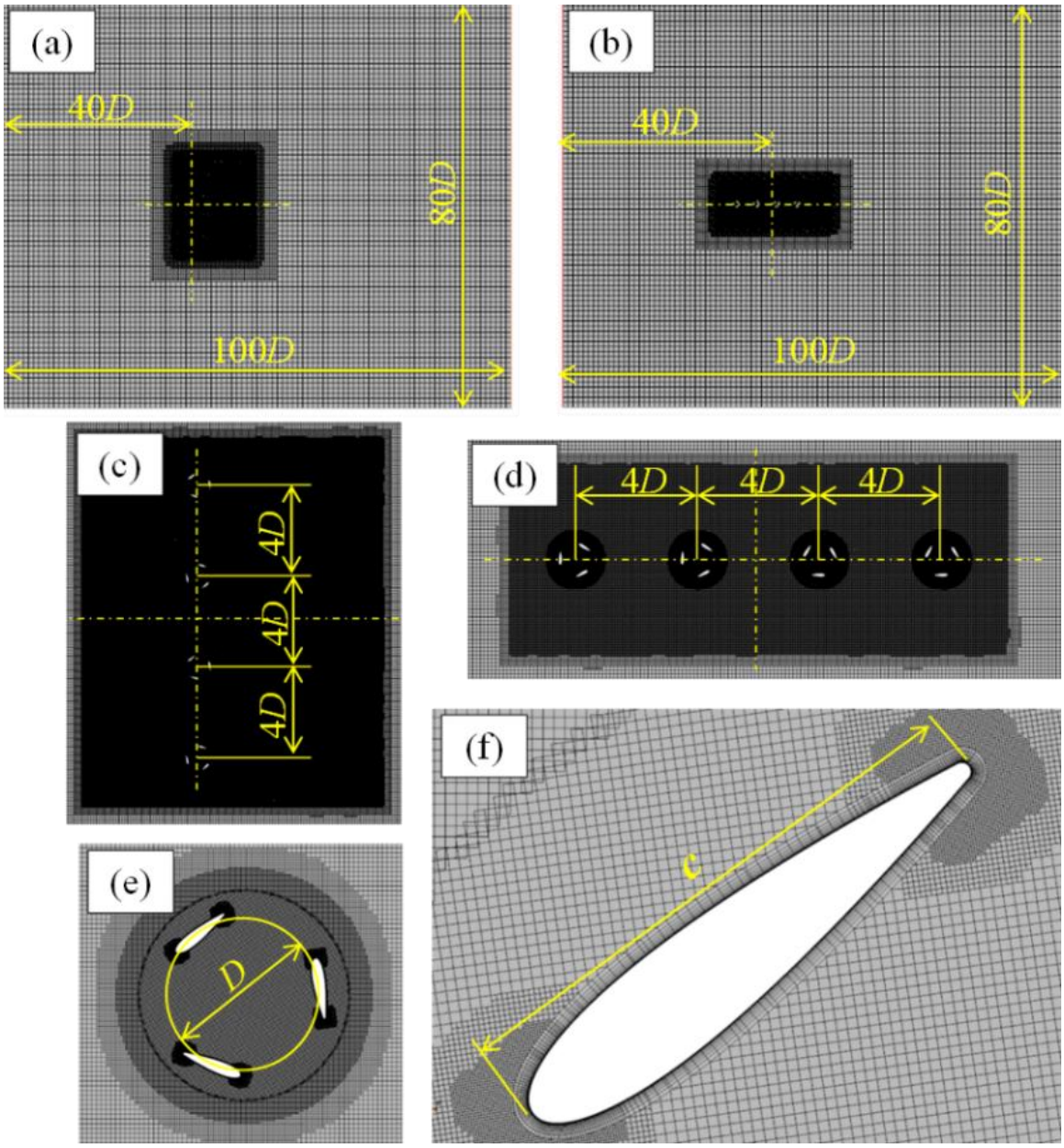

Fig. 3.5 Computation meshes for the CFD analysis of four-rotor layouts: (a) whole domain of the parallel layout; (b) whole domain of the tandem layout; (c) the mesh around the 4 rotors in the parallel array; (d) the mesh around the 4 rotors in the tandem array; (e) the mesh around a rotor; (f) the mesh around a blade

3.3 CFD results analysis

3.3.1 Velocity distribution

The wake model in this study requires the CFD analysis of an isolated single rotor of the target wind turbine to prepare the referenced mean velocity distributions. The reference CFD data for the 5 states of the upstream wind speed U_∞ of 4, 6, 8, 10, and 12 m/s have been prepared in this study. In the CFD calculation, the rotor rotates in counterclockwise. Figure 3.6 shows the averaged distribution of the x-component (u) of the flow velocity around a single rotor at U_∞ = 10 m/s. The flow distribution in Fig. 3.6 shows the creation of the wake behind the rotor and the acceleration regions near the rotor. On the other hand, Fig. 3.7 shows the averaged distribution of the y-component (v) of the flow velocity around the single rotor at U_∞ = 10 m/s. The flow distribution in Fig. 3.7 shows the effects of circulation around the rotor.

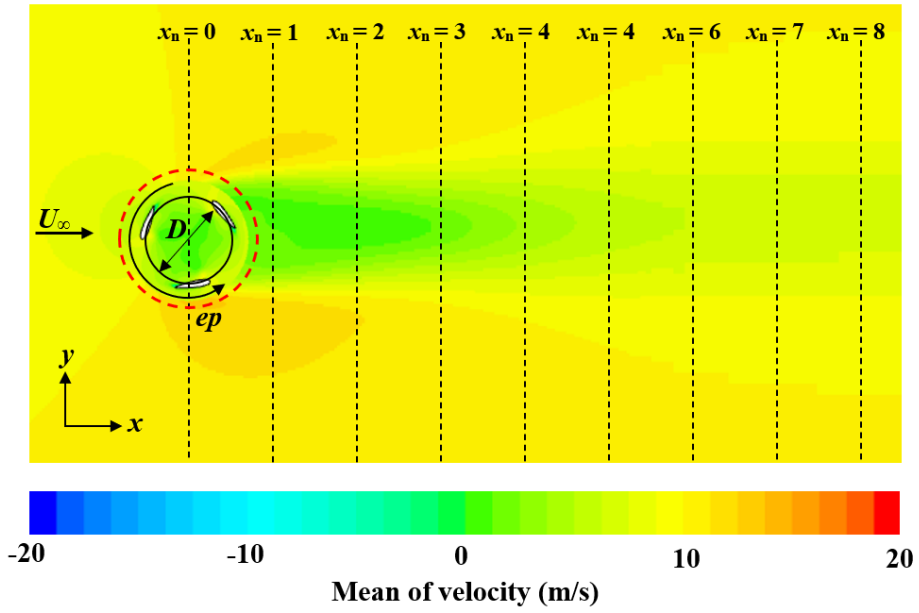

Fig. 3.6 Distribution of the x-component: u of the averaged flow velocity around a single rotor calculated by CFD at U_∞ = 10 m/s

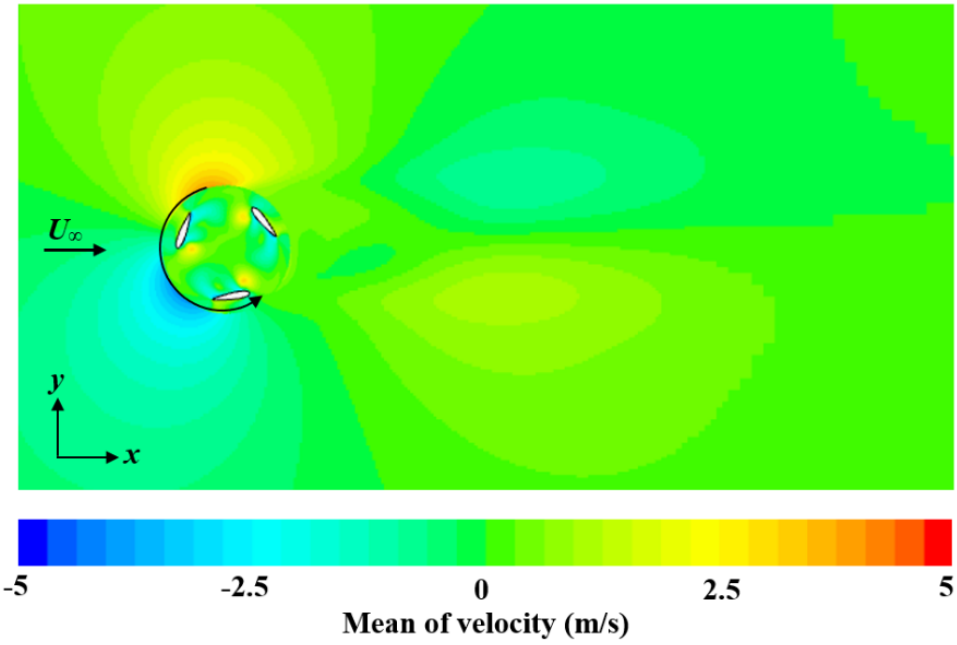

Fig. 3.7 Distribution of the y-component: v of the averaged flow velocity around a single rotor calculated by CFD at U_∞ = 10 m/s

3.3.2 Velocity profile and velocity deficit

Figures 3.8 and 3.9 show the normalized velocity profiles of the x-component in the wake of an isolated single rotor for the 5 states of the upstream wind speed U_∞ of 4, 6, 8, 10, and 12 m/s at $x_n = 0.75$ and $x_n = 2$. From Figs. 3.8 and 3.9, it is clear that the normalized velocity profiles in the main flow component are almost the same for any wind speed. Figure 3.10 shows the variation of the velocity profiles of the x-component of the averaged flow behind a single rotor in the range from $x_n = 1$ to $x_n = 10$, which shows the upward shift of the profiles, i.e., the wake shift. Figures 3.11 and 3.12 show the normalized velocity profiles of the y-component in the wake of an isolated single rotor for the 5 states of the upstream wind speed U_∞ of 4, 6, 8, 10, and 12 m/s at $x_n = 0.75$ and $x_n = 2$. Although the profiles of the cross-flow component have somewhat difference at the different upstream wind speeds, they have the almost the same trend and can be approximated by the averaged profile shown in red dotted curve in Figs. 3.11 or 3.12.

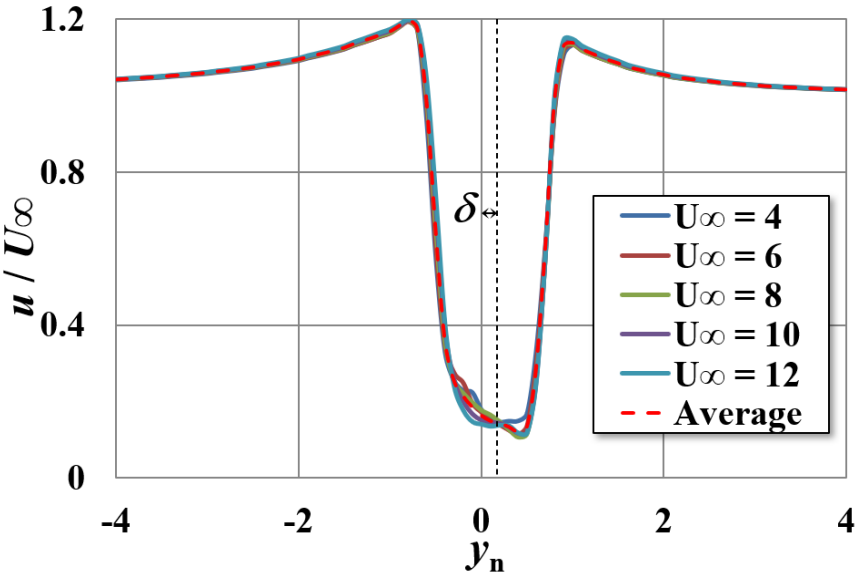

Fig. 3.8 Normalized profile of the x-component (u) of the averaged flow of a single rotor at $x_n = 0.75$ for U_∞ of 4, 6, 8, 10, and 12 m/s. A red dotted curve shows the averaged profile

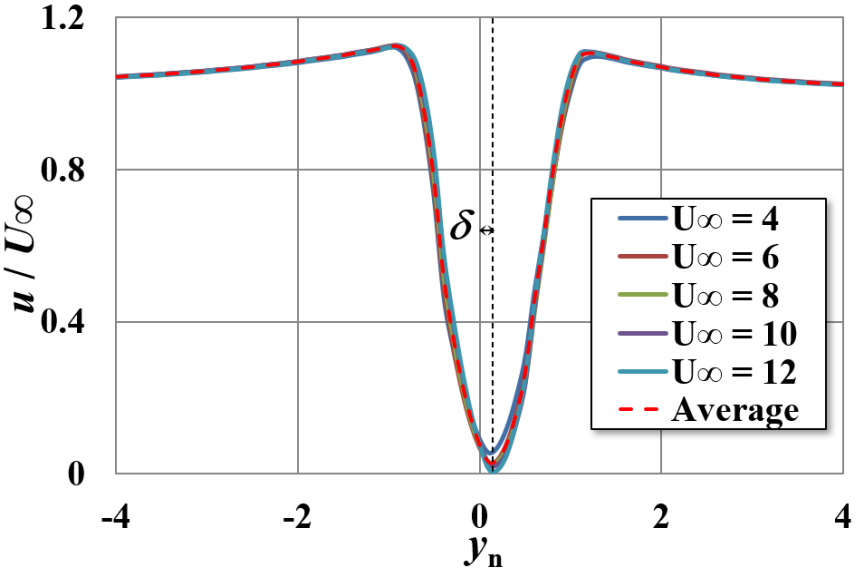

Fig. 3.9 Normalized profile of the x-component (u) of the averaged flow of a single rotor at $x_n = 2.0$ for U_∞ of 4, 6, 8, 10, and 12 m/s. A red dotted curve shows the averaged profile

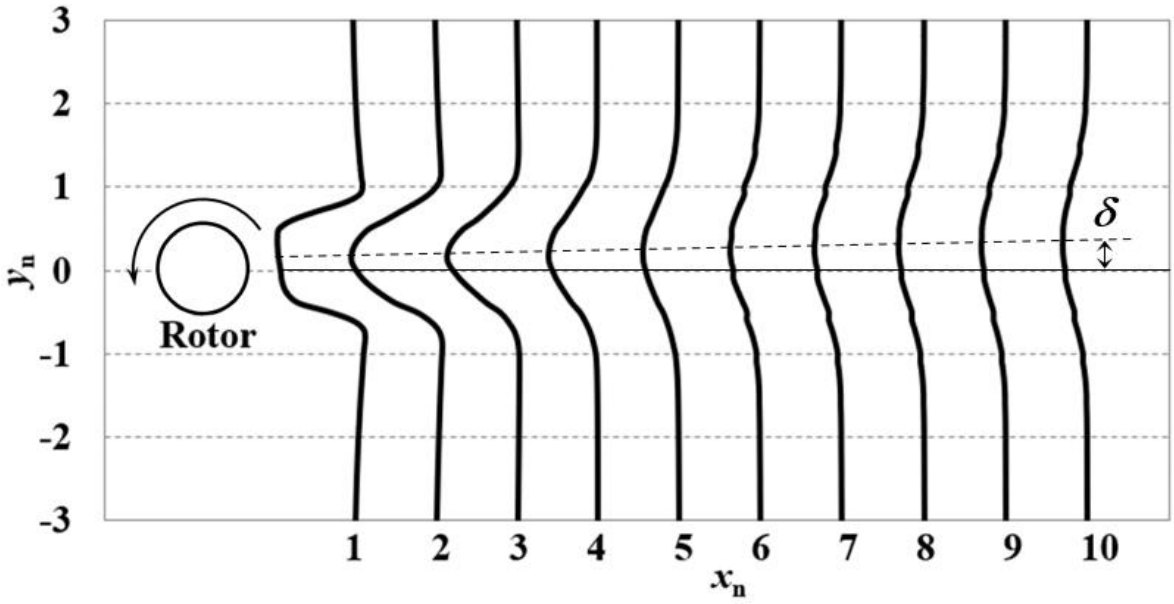

Fig. 3.10 Variation of the velocity profile in the wake of a single rotor

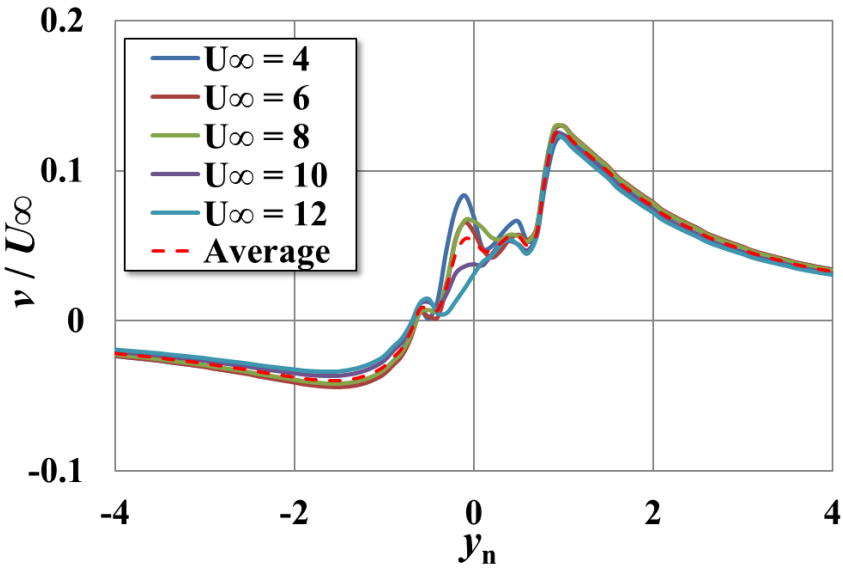

Fig. 3.11 Normalized profile of the y-component (v) of the averaged flow of a single rotor at $x_n = 0.75$ for U_∞ of 4, 6, 8, 10, and 12 m/s. A red dotted curve shows the averaged profile

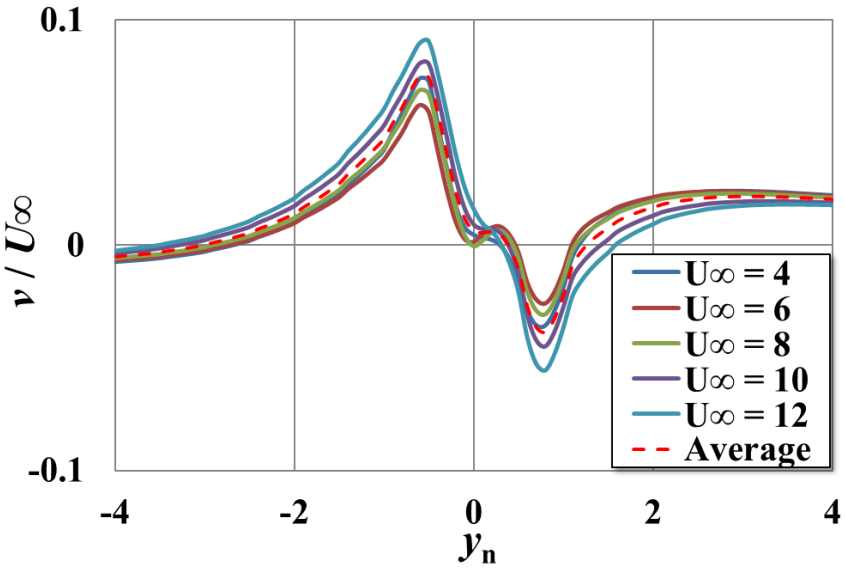

Fig. 3.12 Normalized profile of the y-component (v) of the averaged flow of a single rotor at $x_n = 2.0$ for U_∞ of 4, 6, 8, 10, and 12 m/s. A red dotted curve shows the averaged profile

3.3.3 Circulation

The circulation (Γ) around a rotor can be calculated by integrating the flow field using Eq. (3.5). Figure 3.13 shows the variations in the circulation calculated around a single rotor in the five states of the upstream wind speed U_∞ of 4, 6, 8, 10, and 12 m/s. The circulation in Fig. 3.13 is obtained by integrating the flow velocity simulated by CFD along a circle path whose center is located at the center of a rotor changing the radius r of the circle path. Although the circulation varies according to the integration path, the value takes the maximum at a position close to the rotor but outside the rotational region set in CFD analysis for all the wind speed cases.

$$\Gamma_r = \oint_r \boldsymbol{u} \cdot d\boldsymbol{r} \tag{3.5}$$

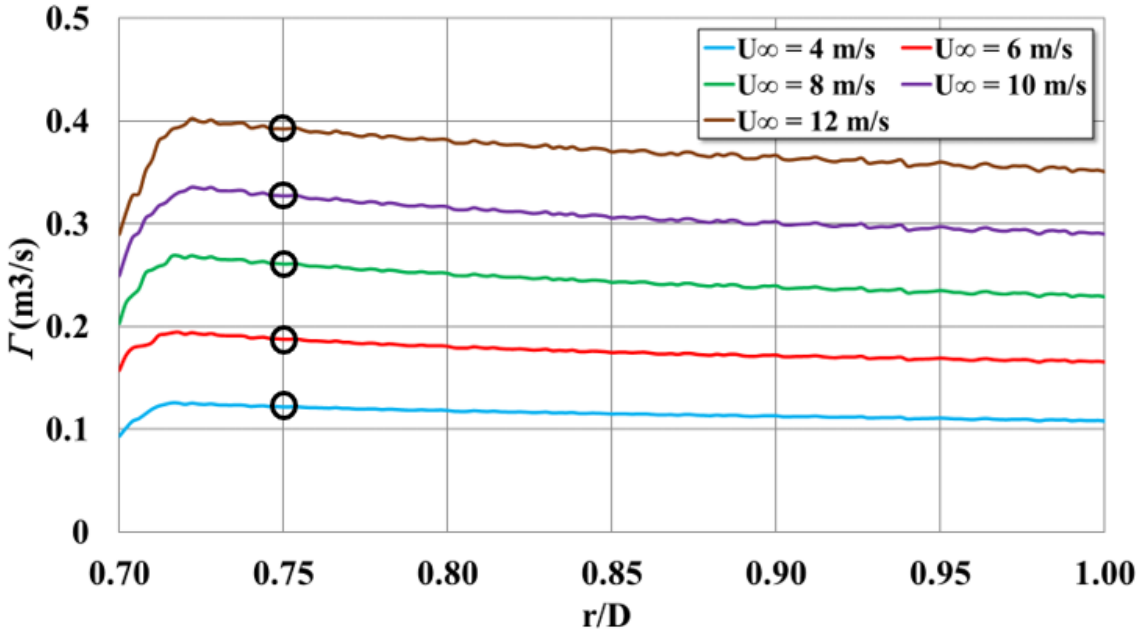

Fig. 3.13 Circulation of a single rotor

The specific radius (r_{ep}/D) which is equal to 0.75 is defined as the evaluation position (e.p.) in this study. A dotted circle in red shown in Fig. 3.6 is the integration path with the specific radius, i.e., the evaluation position of the circulation. The values of the circulation Γ_{ep} at the evaluation position (shown by the black circles in Fig.3.13) are tabulated in Table 3.1. Figure 3.14 shows a graph of Γ_{ep} listed in Table 3.1 against the upstream speed U_∞, which gives the liner relation shown in Eq. (3.6) between Γ_{ep} and U_∞.

Table 3.1. The circulation of the rotor at the evaluation position (Γ_{ep}) in the cases of an isolated single rotor in the five different upstream wind speeds (U_∞) obtained by CFD

U_∞ (m/s)	Γ_{ep}(m^2/s)
4	0.1214
6	0.1875
8	0.2604
10	0.3264
12	0.3915

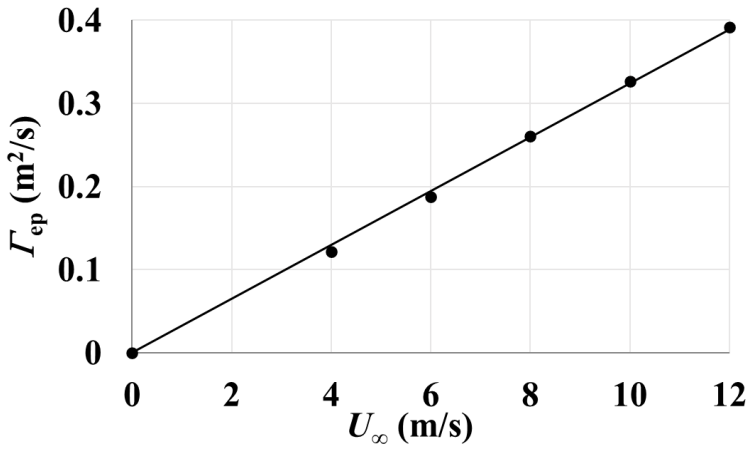

Fig. 3.14 Relation between upstream wind speed and circulation at evaluation position

$$\Gamma_{ep} = 0.0324 U_\infty \tag{3.6}$$

In this study, the circulation of a rotor (Γ) referred in the model calculation is defined to be equivalent to the circulation at the evaluation position (Γ_{ep}) calculated by CFD. The circulation Γ_{ep} of an isolated single rotor at the upstream wind speed U_∞ = 10 m/s is defined as the reference value of the rotor circulation (Γ_{ref}), which is equal to 0.3264 m^2/s in the target rotor used in this study.

3.3.4. Approximation of wake shift of a single rotor

The wake shift was illustrated in Fig. 3.10. Figure 3.15 shows the detailed variations of the minimum speed location, or maximum velocity deficit position, in the wake in the main stream direction at different upstream wind speeds. The wake shift δ is normalized by the rotor diameter D in Fig. 3.15 and the horizontal axis is the normalized x coordinate ($x_{\mathrm{n}} = (x - x_k)/D$). The averaged variation of the normalized wake shift is drawn by a dashed curve in red in Fig. 3.15 and shown by black circles in Fig. 3.16.

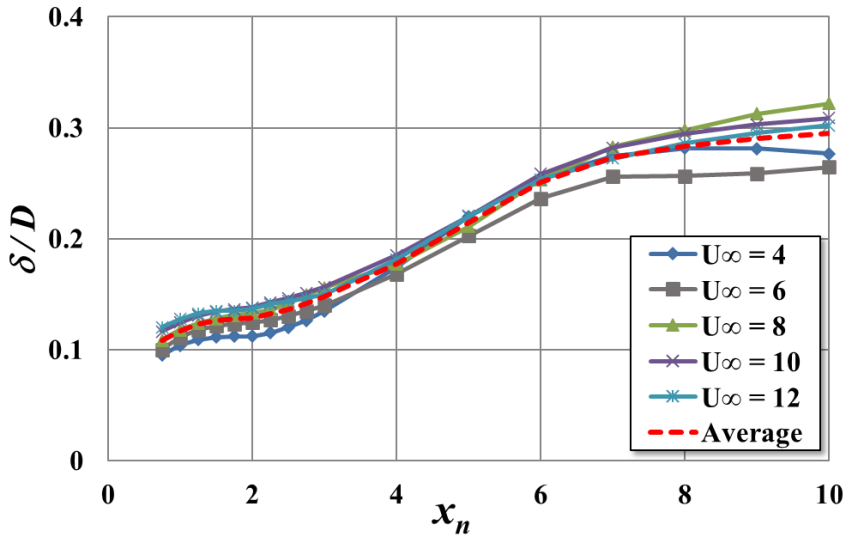

Fig. 3.15 Wake shift of the averaged flow of a single rotor

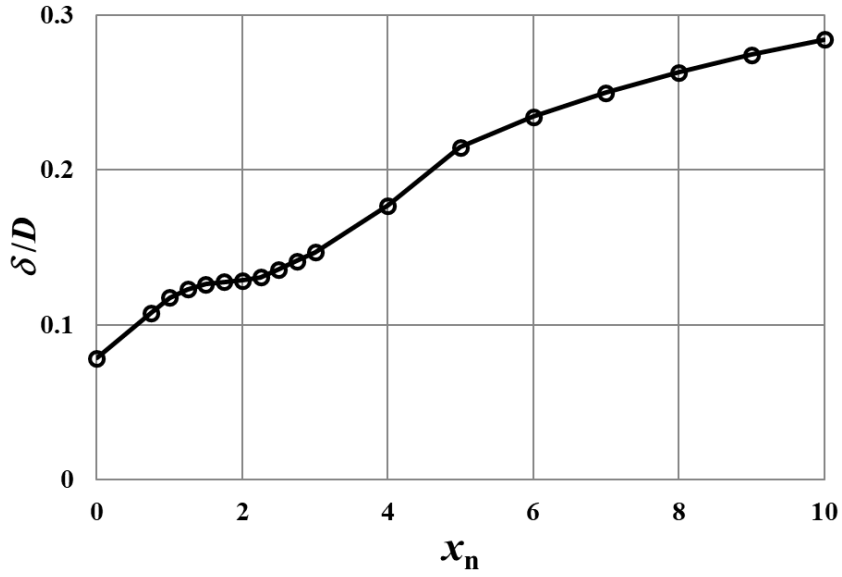

Fig. 3.16 Average wake shift of the averaged flow of a single rotor

The averaged wake shift, which is defined asδ_{SI}, shown in Fig. 3.16 can be approximated by polynomials of the normalized coordinate x_{n} by dividing the wake region into some parts as shown in Eq. (3.7) to Eq. (3.11).

$$\delta_{\mathrm{SI}} = 0 \qquad \text{for } \{x_{\mathrm{n}} < 0\} \tag{3.7}$$

$$\delta_{\mathrm{SI}} = D(0.039x_{\mathrm{n}} + 0.0785) \qquad \text{for } \{0 \le x_{\mathrm{n}} < 0.75\} \tag{3.8}$$

$$\delta_{\mathrm{SI}} = D(0.0149{x_{\mathrm{n}}}^3 - 0.0773{x_{\mathrm{n}}}^2 + 0.1396x_{\mathrm{n}} + 0.04) \qquad \text{for } \{0.75 \le x_{\mathrm{n}} < 1.75\} \tag{3.9}$$

$$\delta_{\mathrm{SI}} = D(-0.0012{x_{\mathrm{n}}}^3 + 0.017{x_{\mathrm{n}}}^2 - 0.0453x_{\mathrm{n}} + 0.1609) \qquad \text{for } \{1.75 \le x_{\mathrm{n}} < 5.0\} \tag{3.10}$$

$$\delta_{\mathrm{SI}} = D(0.1002\ln\ x_{\mathrm{n}} + 0.0542) \qquad \text{for } \{5.0 \le x_{\mathrm{n}}\} \tag{3.11}$$

3.3.5 Thrust force and rotor conditions

The thrust force and rotor conditions obtained by the CFD analysis of an isolated single rotor for each upstream wind speed are converted to those of the equivalent experimental rotor with a height of 43.4 mm in this study. The converted values of the thrust force (Th), output power (P), rotor torque (Q), and angular velocity (ω) of a single rotor in each wind speed are tabulated in Table 3.2.

Table 3.2. The converted values of thrust force and rotor conditions obtained by 2D-CFD into those of the equivalent experiment rotor in an isolated operation in different wind speeds (U_∞)

U_∞ (m/s)	Th(mN)	P(mW)	Q(mNm)	ω(rad/s)
4	23.15	7.99	0.06	192.71
6	51.87	31.88	0.15	206.16
8	89.34	83.76	0.29	284.92
10	141.37	177.62	0.49	363.60
12	191.40	322.17	0.72	445.09

3.3.6 Estimation equations of the state of a wind turbine in a wind farm

The linear relation between the circulation (Γ_{ep}) and the upstream wind speed (U_∞) is given by Eq. (3.6) for an isolated single rotor. Therefore, the circulation Γ_{SI} of a single rotor in an arbitrary wind condition can also be expressed by Eq. (3.12), where U_{∞_ref} is the reference wind speed and is 10 m/s in this study

$$\Gamma_{\mathrm{SI}} = \Gamma_{\mathrm{ref}} \frac{U_\infty}{U_{\infty\_\mathrm{ref}}} \tag{3.12}$$

The state of a rotor in a wind farm is assumed to be estimated by the same relations that are obtained by CFD for an isolated single rotor as the functions of the circulation.

That is, with the relation between U_∞ and Th shown in Table 3.2 and the linearity between U_∞ and Γ_{SI} in Eq. (3.12), the thrust force (mN) of a 2D-rotor with a circulation Γ is given by Eq. (3.13).

$$Th = Th_{\mathrm{ref}}\left(\frac{\Gamma}{\Gamma_{\mathrm{ref}}}\right)^2 \tag{3.14}$$

Since the blockage effect can be assumed to be proportional to the thrust force, μ (m^3/s) of a 2D-rotor in a VAWT cluster is expressed by Eq. (3.14).

$$\mu = \mu_{\mathrm{ref}}\left(\frac{\Gamma}{\Gamma_{\mathrm{ref}}}\right)^2 \tag{3.13}$$

In the same manner, from the relations in Table 3.2, the estimation equations of power P (mW), torque Q (mNm), and angular velocity ω (rad/s) of a rotor with a circulation Γ are given by Eqs. (3.15), (3.16), and (3.17), respectively

$$P = P_{\mathrm{ref}}\left(\frac{\Gamma}{\Gamma_{\mathrm{ref}}}\right)^3 \tag{3.15}$$

$$Q = Q_{\mathrm{ref}}\left(\frac{\Gamma}{\Gamma_{\mathrm{ref}}}\right)^2 \tag{3.16}$$

$$\omega = \omega_{\mathrm{ref}}\frac{\Gamma}{\Gamma_{\mathrm{ref}}} \tag{3.17}$$

In Eqs. (3.13)–(3.17), the reference values, which correspond to the values at the reference wind speed U_{∞_ref} = 10 m/s in this study, are Th_{ref} = 141.37 mN, μ_{ref} = 0.0015 m^3/s, P_{ref} = 177.62 mW, Q_{ref} = 0.49 mNm and ω_{ref} = 363.60 rad/s.

The x-direction pressure loss Fp described in section 2.3.1 depends on the volume of the control volume (CV) in addition to the circulation Γ and is obtained by CFD results for an isolated single rotor. Fp can be expressed as a cubic function of Γ as shown in Eq. (3.18) if a specific CV is defined.

$$Fp = Fp_{\mathrm{ref}}\left(\frac{\Gamma}{\Gamma_{\mathrm{ref}}}\right)^3 \tag{3.18}$$

The reference values of the pressure loss are given as Fp_{ref} = 229.61 mN for the CV of $20D \times 20D \times 0.868D$ and Fp_{ref} = 347.95 mN for the CV of $40D \times 40D \times 0.868D$, respectively.

References

[1] Menter F. R. Two-equation eddy-viscosity turbulence models for engineering applications. *AIAA Journal* 1994, 32, 8, 1598–1605.

[2] Hara, Y.; Jodai, Y.; Okinaga, T.; Furukawa, M. Numerical analysis of the dynamic interaction between two closely spaced vertical-axis wind turbines. *Energies* 2021, 14, 2286.

Chapter 4

Results and discussions

4.1 Introduction

The method described in chapter 2 is validated in this Chapter by applying it to the several layouts consisting of the same small 2D-rotors as used in the section 2.3.5. At first, in Section 4.2, the power dependency of the isolated single rotor on the wind speed is compared between the model calculation and the CFD. Then, in Section 4.3, the power dependency of the paired rotors on the 16 wind directions is compared between the present method and the CFD analysis. After that, as the more complicated layouts, the power dependency of the three-rotor cluster on the 12 wind directions is investigated in Section 4.4. Finally, to show the applicability of the proposed method to VAWT wind farms, the power prediction in the four-rotor layouts arranged in line are tried in Section 4.5.

4.2 An isolated single rotor

Table 4.1 shows the comparison between the CFD analysis [1] and the model simulation using the present method based on the momentum balance in the cases of an isolated single rotor in the five different upstream wind speeds (U_∞). Although the original CFD analysis was conducted using a wide calculation domain of $40D \times 50D$, the square region of $20D \times 20D$ enclosing the single rotor is extracted as the CV, which is the same size as that of the model simulation, in order to acquire the dependence of the pressure loss Fp on the

circulation of the isolated single rotor. The output power shown in the unit of "mW" is equivalent to that of the small rotor, the size of which is 50 mm in diameter × 43.4 mm in height. The parameters necessary to rebuild the flow field calculated by the CFD are obtained at the reference wind speed of U_∞ =10 m/s, as described in Chapter 3. Therefore, the smallest percentage difference (*%Error*) between the model and CFD results is obtained in the case of U_∞ =10 m/s. The output power predicted for a single rotor in other wind speed agrees well with the CFD result; this means the method using the momentum conservation works well in the case of an isolated single rotor in an arbitrary wind speed.

Table 4.1 Comparison between the predicted power output of an isolated single rotor by the present method and the CFD results [1]

U_∞ (m/s)	P_Model (mW)	P_CFD (mW)	*% Error*
4	8.14	7.99	1.88
6	32.87	31.88	3.11
8	85.50	83.76	2.08
10	177.62	177.62	0.0
12	314.23	322.17	-2.46

4.3 Paired rotors

Figures 4.1 and 4.2 show the definition of relative wind direction (θ) to a rotor pair. The layouts of the two rotors are categorized into two kinds in terms of the relative rotational direction. The configuration in Fig. 4.1 is defined as the co-rotation (CO), in which the two rotors rotate in the same direction. The CO configuration includes the typical CO and TD

layouts shown in Fig. 2.18. On the other hand, the configuration in Fig. 4.2 is defined as the inverse-rotation (IR), in which the two rotors rotate mutually in the opposite directions. The IR configuration includes the typical layouts of CD, CU, and TD. The dashed lines in red in Figs 4.1 and 4.2 correspond to the boundaries of the wake zone defined by the angle γ_1 in Fig. 2.19. The angle γ_1 is set at 30° in this study.

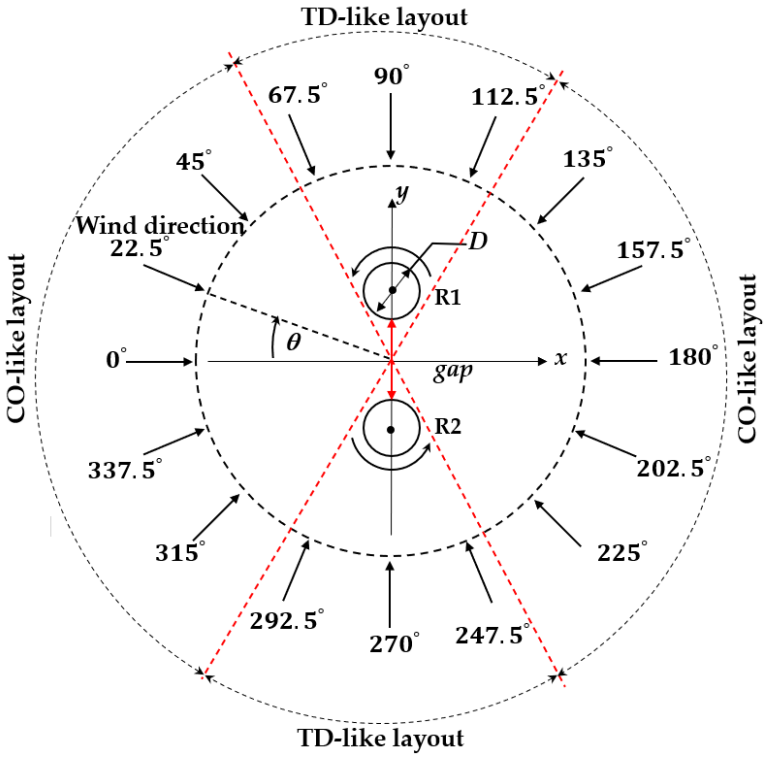

Fig. 4.1 Definition of 16 wind directions in the co-rotation (CO) configuration of paired rotors

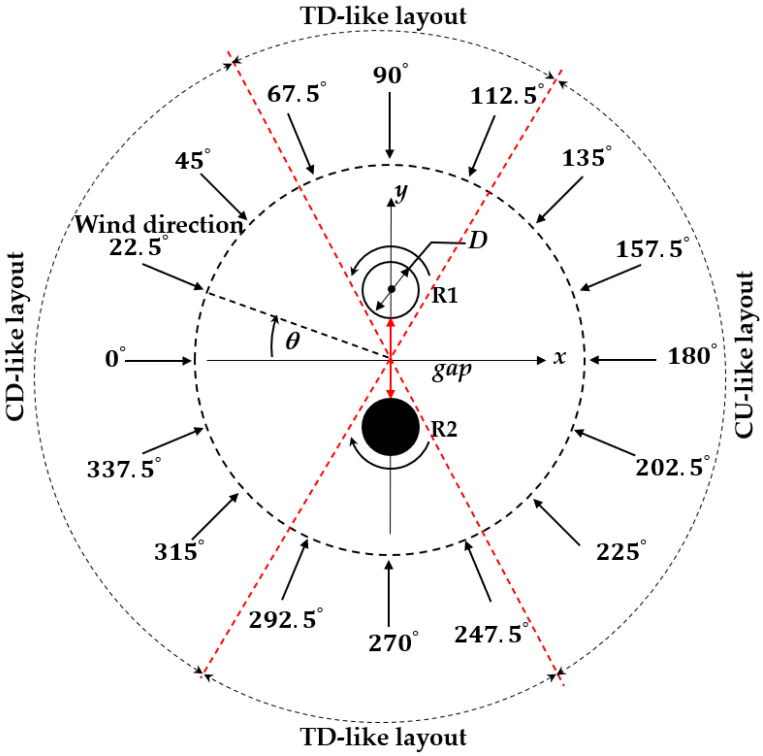

Fig. 4.2 Definition of 16 wind directions in the inverse-rotation (IR) configuration of paired rotors

The power outputs of the upper (Rotor 1: R1) and lower (Rotor 2: R2) rotors in Fig. 4.1 or Fig. 4.2 and the averaged power of both rotors were predicted in each of the 16 wind directions using the present method under the condition of the upstream speed U_∞ of 10 m/s. The results in the case the inter-rotor distance (*gap*) is equal to the rotor diameter are shown in Figs. 4.3a–c for the CO and Figs. 4.4a–c for the IR configurations. Each of the predicted rotor power is normalized by the power of the isolated single rotor (SI) and compared with the normalized CFD results in Figs. 4.3 and 4.4. The conditions of θ = 0° and 180° in Fig. 4.3c are the same CO layout and their output powers were adjusted to agree to the CFD results to get the adequate value of the parameter α_1. The conditions of θ = 0° and 180° in

Fig. 4.4c corresponds to the CD and CU layouts, respectively, and the values of the parameters α_2 and α_3 were adjusted so as to agree to the CFD results. Similarly, the conditions of θ = 90° and 270° in Figs. 4.3c and 4.4c correspond to either of the two TD layouts shown in Fig. 2.18d, and the parameter α_4 can be determined by fitting the resultant circulation obtained by the model simulation to that of the CFD analysis in one of the four TD conditions. The actual values of α_1, α_2, α_3, and α_4 were already shown in Sec. 2.3.5. Although the difference between the model simulation and the CFD analysis is somewhat large in a few wind directions as shown in Figs. 4.3 and 4.4, the method can predict the power of a rotor pair with the gap = 1.0*D* very well.

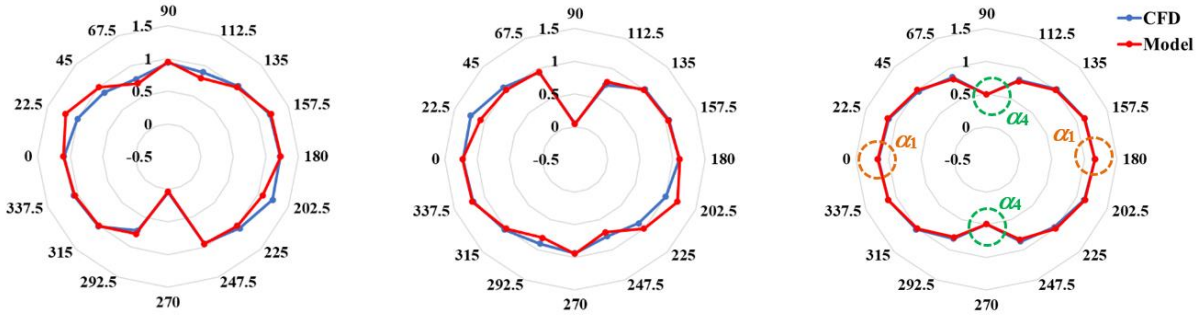

(a) (b) (c)

Fig. 4.3 Distributions of normalized rotor powers in the CO configuration in the case of *gap* = 1.0*D*: (a) Rotor 1; (b) Rotor 2; (c) average

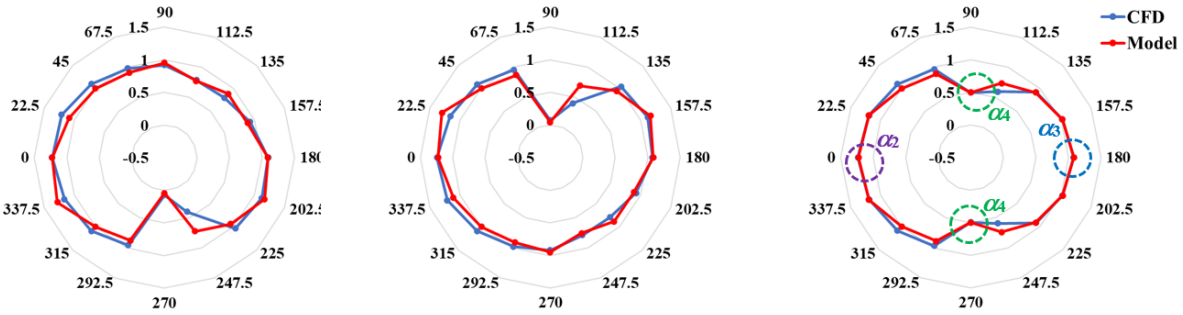

(a) (b) (c)

Fig. 4.4 Distributions of normalized rotor powers in the IR configuration in the case of *gap* = 1.0*D*: (a) Rotor 1; (b) Rotor 2; (c) average

Figures 4.5 and 4.6 are the results of the rotor power distribution of the paired rotors with the gap = 0.5*D*. The model simulation seems to underestimate the rotor powers compared to the CFD analysis in many wind directions. This fact may suggest the necessity to modify the interaction functions I_j defined in Eqs. (2.31)–(2.34) in the case of short inter-rotor distance.

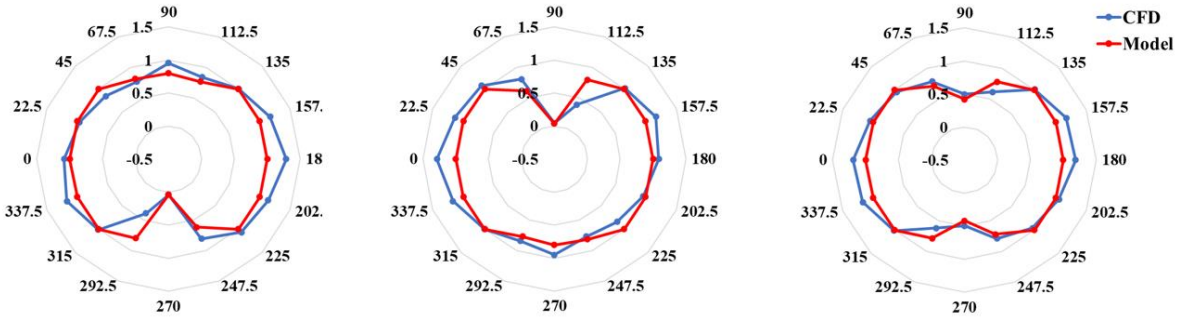

(a) (b) (c)

Fig. 4.5 Distributions of normalized rotor powers in the CO configuration in the case of *gap* = 0.5*D*: (a) Rotor 1; (b) Rotor 2; (c) average

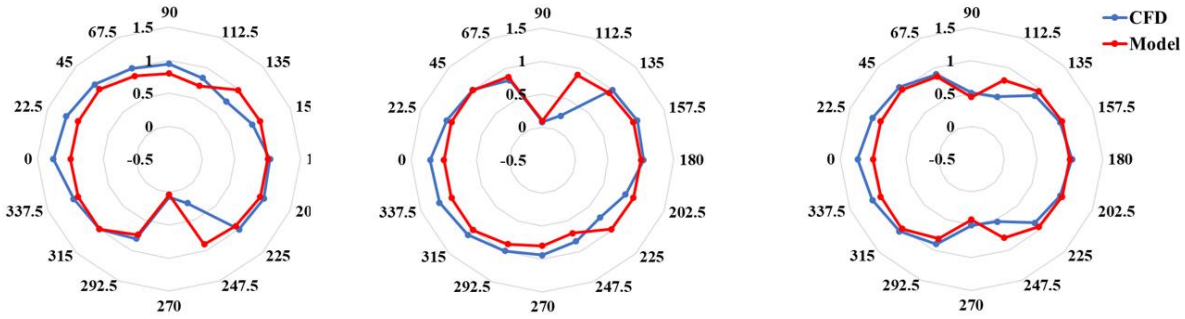

(a) (b) (c)

Fig. 4.6 Distributions of normalized rotor powers in the IR configuration in the case of *gap* = 0.5*D*: (a) Rotor 1; (b) Rotor 2; (c) average

Figures 4.7 and 4.8 show the results in the case of *gap* = 2.0*D*. Except for a few directions, the model and CFD predictions agree well. This shows that the interaction functions I_j defined in Eqs. (2.31)–(2.34) are effective in the long inter-rotor distance cases of paired rotors.

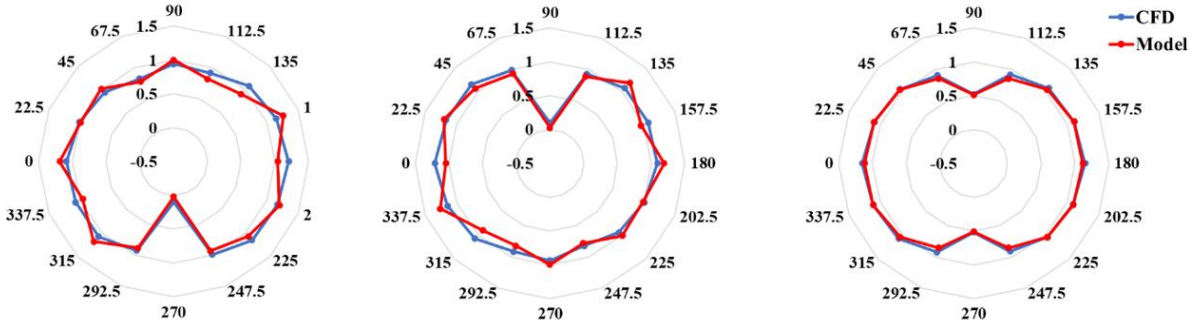

(a) (b) (c)

Fig. 4.7 Distributions of normalized rotor powers in the CO configuration in the case of *gap* = 2.0*D*: (a) Rotor 1; (b) Rotor 2; (c) average

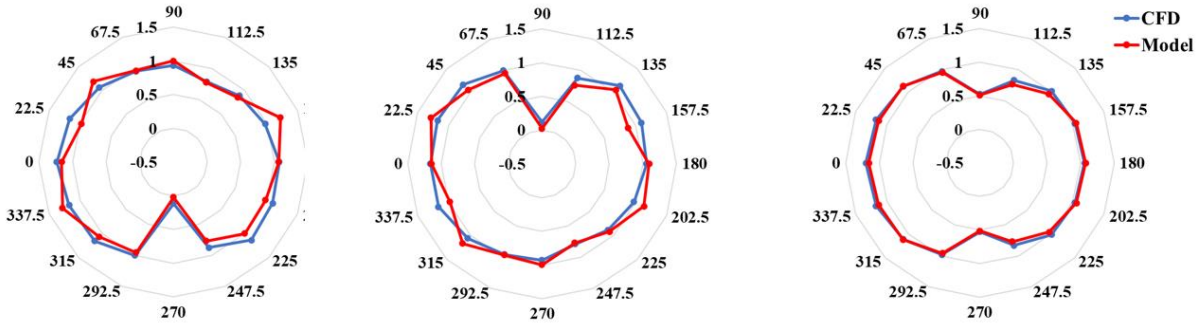

(a) (b) (c)

Fig. 4.8 Distributions of normalized rotor powers in the IR configuration in the case of *gap* = 2.0*D*: (a) Rotor 1; (b) Rotor 2; (c) average

Although the further improvements may be needed in the present method, it is worth noting that the prediction of the power of paired rotors in a specific wind direction can be performed by the method in about 40 minutes, which is about 500 times shorter than the CFD analysis using the DFBI model (typically about 2 weeks with 8 core PC).

4.4 Three-rotor cluster

The three-rotor cluster is also categorized into the CO and IR configurations. Figures 4.9 and 4.10 show the definition of the 12 wind directions in each of the two configurations in the cases of three-rotor clusters which are arranged like a triangular shape with an inter-rotor space of gap = 1.0*D*. Under the condition of the upstream wind speed U_∞ of 10 m/s, the prediction of the averaged output power of the rotor clusters was carried out. All the parameters and necessary relations such as the pressure loss function are the same as those used in the case of paired rotors except for the division of the searching range of circulation.

The number of divisions of the searching range was set as 10 in the three-rotor case instead of 25 used in paired rotors case to save the calculation time. Therefore, the error in the prediction is anticipated to be a little worse.

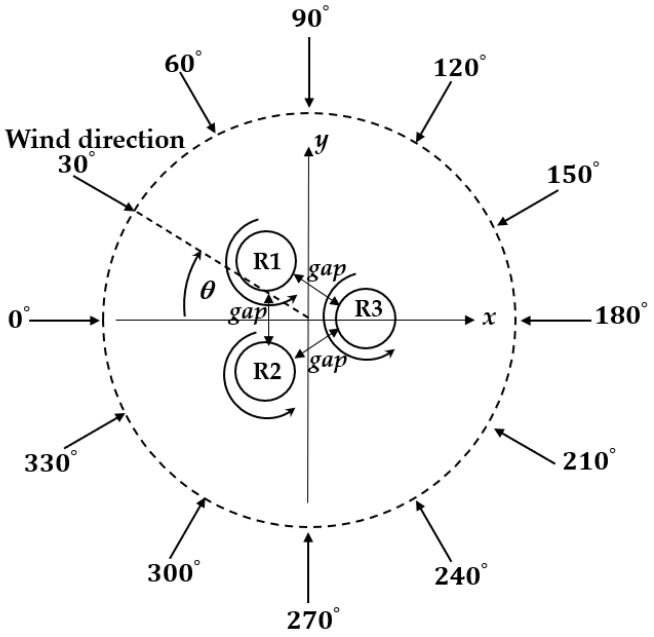

Fig. 4.9 Definition of 12 wind directions in the co-rotation (CO) configuration of three-rotor cluster

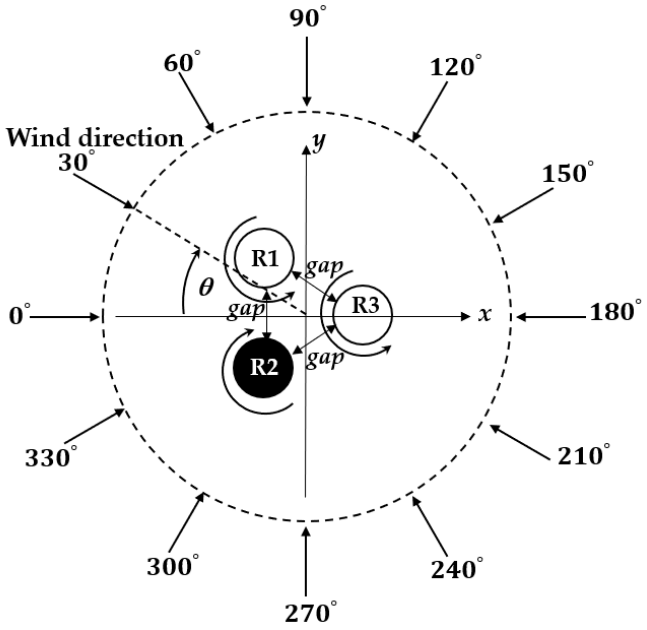

Fig. 4.10 Definition of 12 wind directions in the inverse-rotation (IR) configuration of three-rotor cluster

Figures 4.11 and 4.12 are the prediction results of the averaged power of the three-rotor cluster. The averaged power is normalized by the single rotor power in Figs. 4.11 and 4.12, in which the red symbols show the results of model simulation and the blue symbols show the CFD analysis reported in Ref. [2]. The model calculation underestimates the averaged power of the rotor clusters. However, the dependence on the wind direction is well simulated and the model simulation gives the same trend as the CFD analysis.

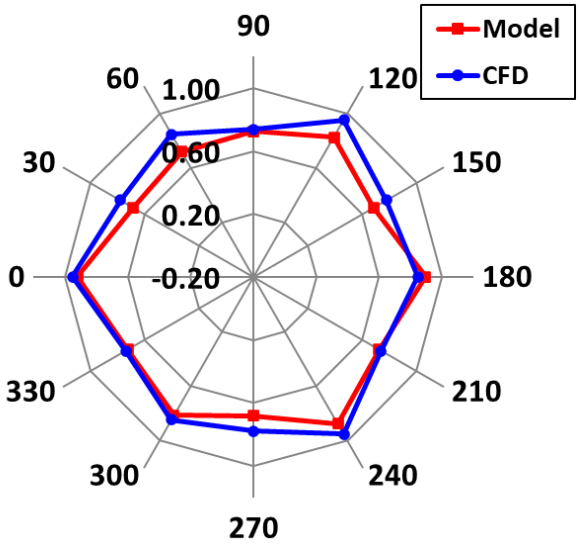

Fig. 4.11 Distributions of averaged power of three rotors in the CO configuration shown in Fig. 4.9

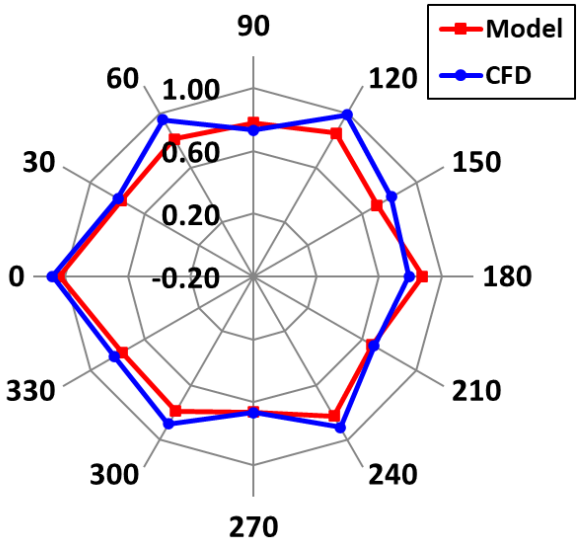

Fig. 4.12 Distributions of averaged power of three rotors in the IR configuration shown in Fig. 4.10

4.5 Four-rotor cluster

In order to show the applicability of the proposed method to VAWT wind farms, four-rotor layouts arranged in line with an inter-rotor space of 3.0D are selected as the targets of the output power prediction in this section. To cover a large number of rotors, the CV is set to be a large size of 40D × 40D × 0.868D. As the size of the CV is changed, the function expressing the pressure loss Fp of the CV has to be newly prepared from the CFD flow field of the isolated single rotor; i.e., the reference value Fp_{ref} in Eq. (3.18) in chapter 3 is changed from 229.61 to 347.95 mN in the prediction of the four-rotor clusters. The upstream wind speed is assumed to be 10 m/s in the present prediction of the four-rotor clusters and the number of divisions of the searching range of the circulation of each rotor is set as 8. In this case, the calculation time is about 50 times longer than the calculation time in a two-rotor case with 25 divisions because the subdivision process is executed twice in the actual calculation using the in-house code as shown in Fig. 2.20.

Figures 4.13–4.16 show the results of the power prediction and the distributions of x- and y-direction velocity components in two kinds of four-rotor layouts, i.e., parallel and tandem, respectively. The fitting parameters α_1, α_2, α_3, and α_4 are set to be the same values as those used in the paired rotors (see Section 2.3.5). The model predicts the decrease in the rotor power in the order of R1, R2, R3, and R4 in the parallel array of four rotors. Similarly, in the tandem array of four rotors, the output power decreases in the same order.

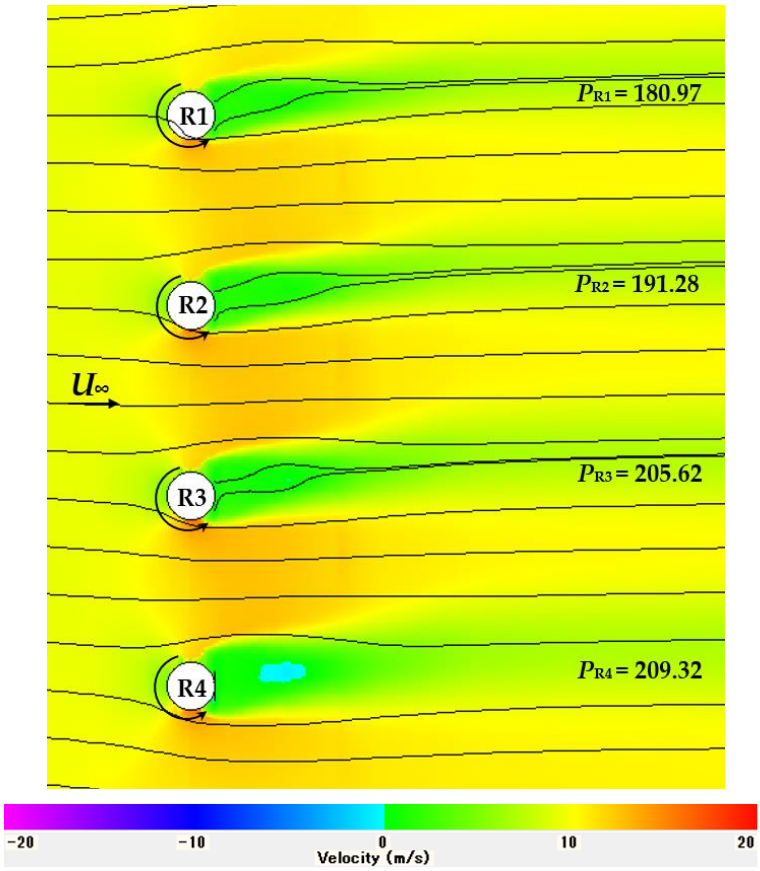

Fig. 4.13 Prediction of the distributions of *x*-direction velocity components around four-rotor parallel layouts (U_∞ = 10 m/s, inter-rotor space (*gap*) = 3.0*D*)

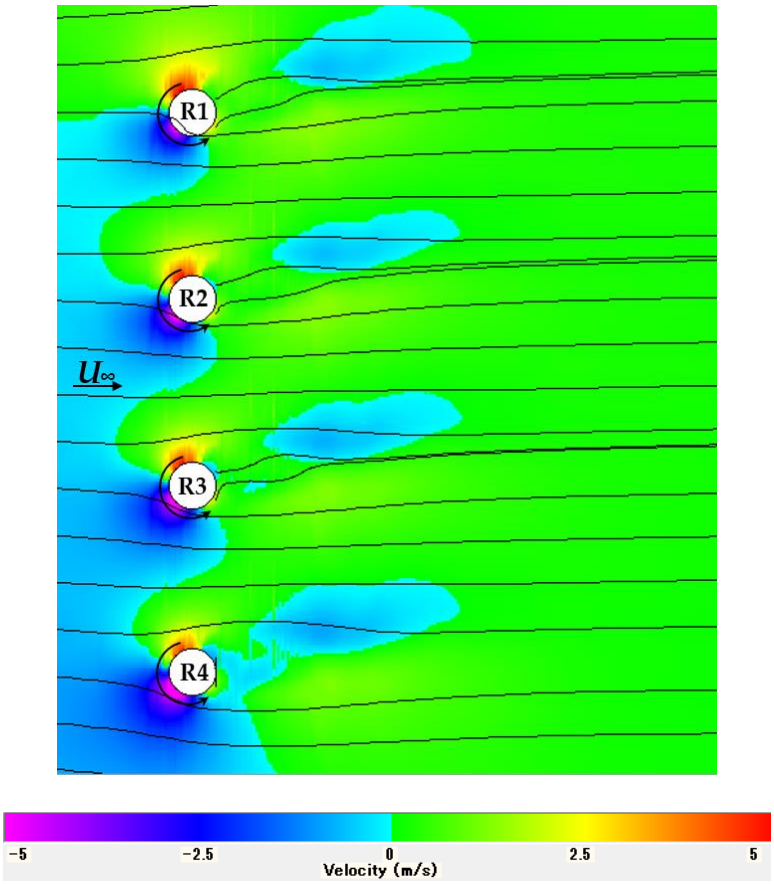

Fig. 4.14 Prediction of the distributions of *y*-direction velocity components around four-rotor parallel layouts (U_∞ = 10 m/s, inter-rotor space (*gap*) = 3.0*D*)

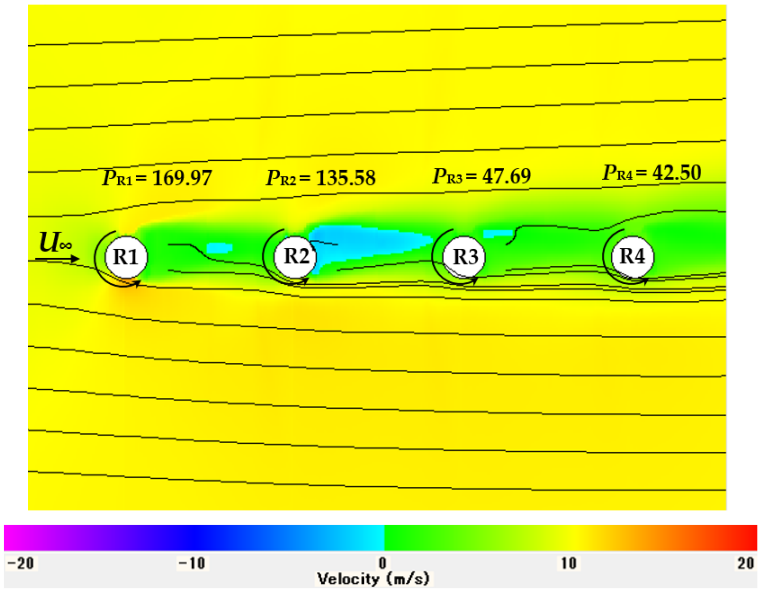

Fig. 4.15 Prediction of the distributions of *x*-direction velocity components around four-rotor tandem layouts (U_∞ = 10 m/s, inter-rotor space (*gap*) = 3.0*D*)

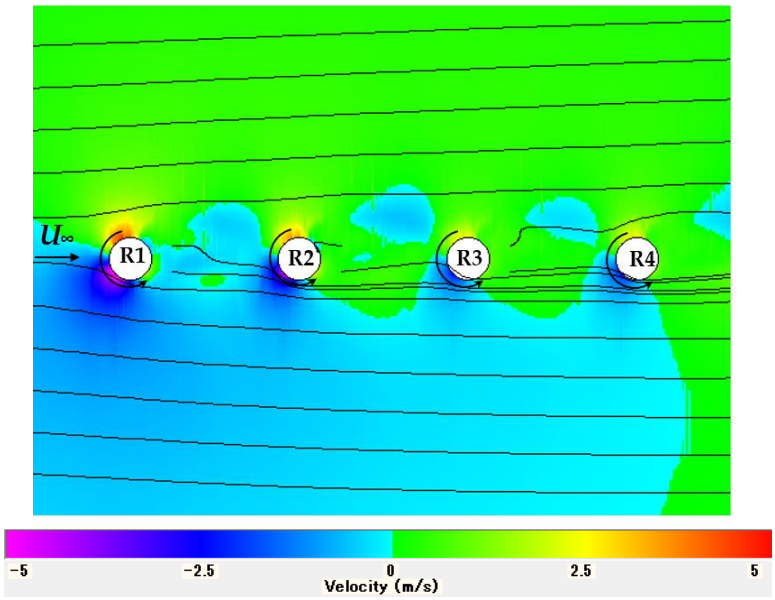

Fig. 4.16 Prediction of the distributions of *y*-direction velocity components around four-rotor tandem layouts (U_∞ = 10 m/s, inter-rotor space (*gap*) = 3.0*D*)

In this study, the CFD analysis of the two kinds of four-rotor layouts was carried out by using the DFBI model. The details of the meshes created for the four-rotor layouts in the present study are shown in Fig. 3.5. The upstream wind speed U_∞ is set at 10 m/s in the CFD analysis, too.

Figures 4.17 and 4.19 show the distributions of x-component of unsteady velocity obtained by the CFD for the parallel and tandem layouts, respectively. Figures 4.18 and 4.20 illustrate the unsteady flow field shown by the y-component velocity for the two layouts of four rotors. The conditions shown in Figs. 4.17–4.20 correspond to the states at 4 s from the beginning of each simulation. The time history of the angular velocity of each rotor is shown in Figs. 4.21 and 4.22 for the parallel and tandem layouts, respectively. The calculation using the DFBI model was conducted until 4 s for each layout when the convergence was almost attained. In the last 0.5 s, the angular velocity was averaged to be used to evaluate the power output of each rotor. In the calculations shown in 4.21 and 4.22, the initial angular velocity is 360 rad/s for all rotors in the parallel layout. On the other hand, in the tandem case, the initial values are set at 366, 250, 200, and 180 rad/s for R1, R2, R3, and R4, respectively. The CFD analysis was conducted by a high-performance PC with 28 cores; it took about 1 week for each calculation of two layouts.

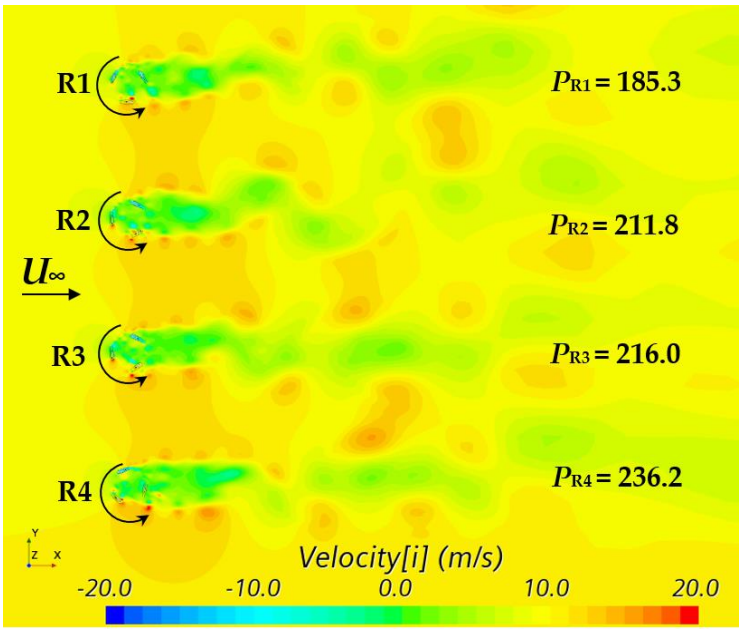

Fig. 4.17 Unsteady flow field (*x*-component) around the four-rotor parallel layout simulated by CFD using the DFBI model (U_∞ = 10 m/s, inter-rotor space (*gap*) = 3.0*D*)

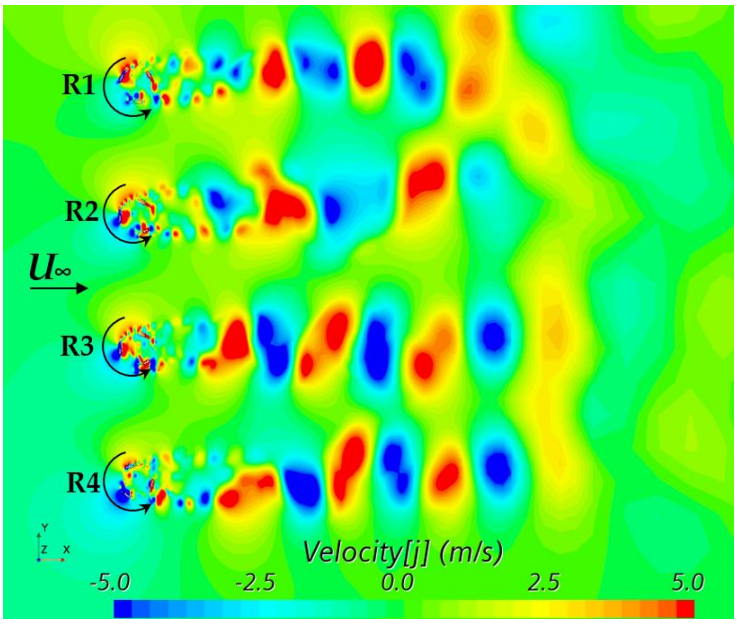

Fig. 4.18 Unsteady flow field (*y*-component) around the four-rotor parallel layout simulated by CFD using the DFBI model (U_∞ = 10 m/s, inter-rotor space (*gap*) = 3.0*D*)

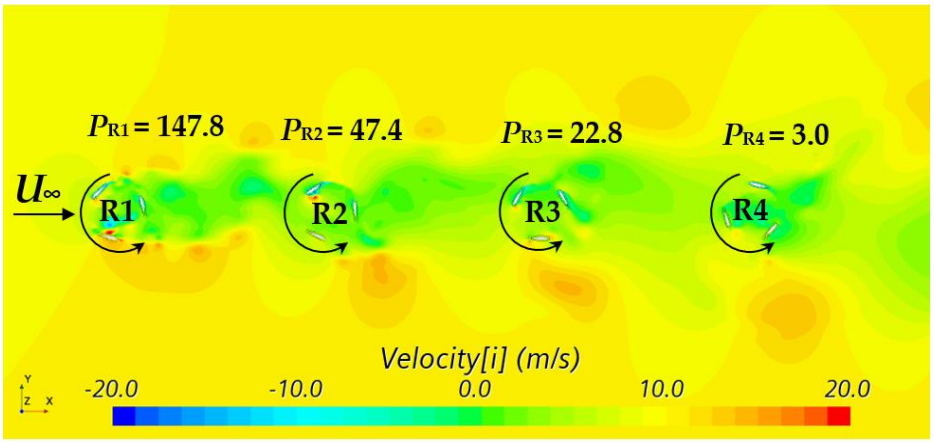

Fig. 4.19 Unsteady flow field (*x*-component) around the four-rotor tandem layout simulated by CFD using the DFBI model (U_∞ = 10 m/s, inter-rotor space (*gap*) = 3.0*D*)

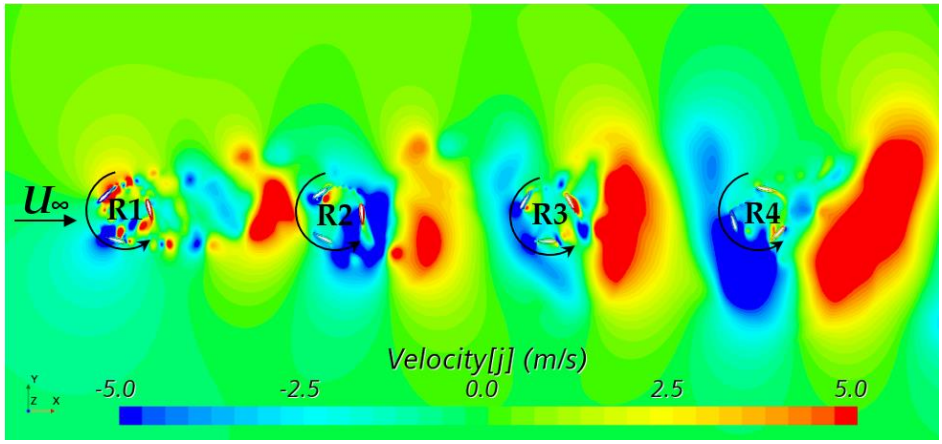

Fig. 4.20 Unsteady flow field (*y*-component) around the four-rotor tandem layout simulated by CFD using the DFBI model (U_∞ = 10 m/s, inter-rotor space (*gap*) = 3.0*D*)

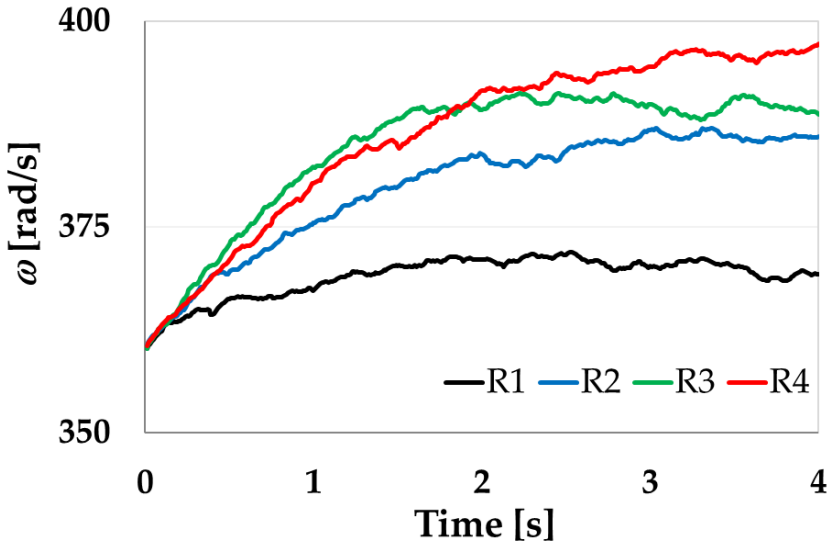

Fig. 4.21 CFD results of the time history of the angular velocity of each rotor in parallel layout four rotors

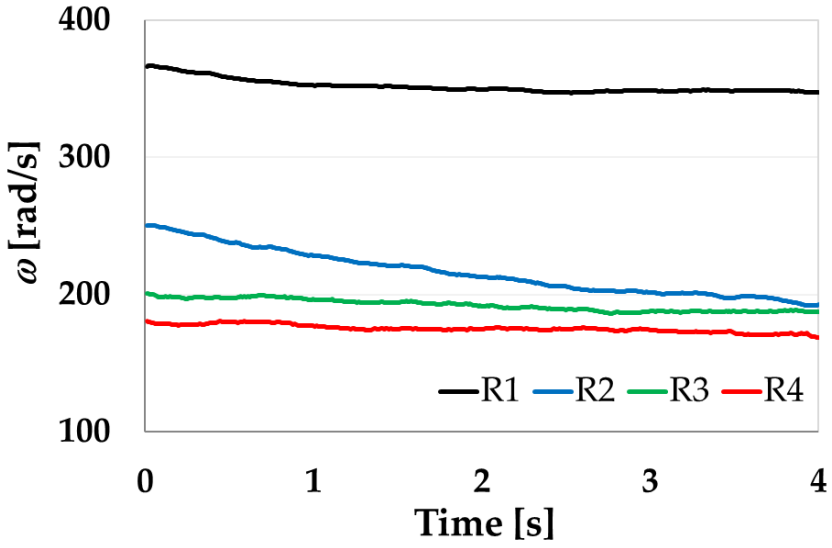

Fig. 4.22 CFD results of the time history of the angular velocity of each rotor in tandem layout four rotors

Table 4.2 shows the comparison of each rotor power in the parallel or tandem layouts between the present model and CFD analysis. The percentage error of the rotor power (*Err.P*) is defined by Eq. (4.1) in this study. P_{Model} is the rotor power predicted by the proposed model using Eq. (3.15) and the P_{CFD} is the CFD result of the rotor power which is obtained by multiplying the averaged angular velocity and the averaged rotor torque during the last 0.5 s. The P_{ref} is the output power of an isolated single rotor.

$$Err.P = \frac{P_{\mathrm{Model}} - P_{\mathrm{CFD}}}{P_{\mathrm{ref}}} \times 100 \tag{4.1}$$

Table 4.2 Comparison of each rotor power in the parallel or tandem layouts between the present model and the CFD analysis

Layout	Parallel				Tandem			
Rotor	R1	R2	R3	R4	R1	R2	R3	R4
Power (model) (mW)	181.0	191.3	205.6	209.3	170.0	135.6	47.7	42.5
Power (CFD) (mW)	185.3	211.8	216.0	236.2	147.8	47.4	22.8	3.0
Err.P (%)	−2.4	−11.5	−5.8	−15.1	12.5	49.5	14.0	22.2

The comparison shown in Table 4.2 does not give satisfactory results. In particular, the difference between the model and CFD is large in the tandem layout of four rotors. One of the reasons for the disagreement is the small number of initial divisions of the searching range used for the model prediction. To improve the results by avoiding the false conditions, an advanced method like the genetic algorithm (GA) should be used to give the possible combinations of circulations at random. Further improvement in the model of the interaction among rotors also is necessary. Nevertheless, the present model can predict the same trend in the rotor power in the parallel and tandem layouts of four rotors as that of the CFD analysis.

References

[1] Hara, Y.; Jodai, Y.; Okinaga, T.; Furukawa, M. Numerical analysis of the dynamic interaction between two closely spaced vertical-axis wind turbines. *Energies* 2021, 14, 2286.

[2] Okinaga, T.; Hara, Y.; Yoshino, K.; Jodai, Y. Numerical simulation considering the variation in rotational speed of three closely spaced vertical-axis wind turbines. *In Proceedings of JWEA 43rd Wind Energy Utilization Symposium*, Tokyo, Japan, 18–19 November 2021.

[3] Buranarote, J.; Hara, Y.; Furukawa, M.; Jodai, Y. Method to Predict Outputs of Two-Dimensional VAWT Rotors by Using Wake Model Mimicking the CFD-Created Flow Field. *Energies* 2022, 15, 5200.

Chapter 5

Summary and Recommendations

5.1 Summary

The main objective of this thesis was to propose a method to predict the outputs of two-dimensional (2-D) VAWT rotors (or VAWT cluster) in a short time, for the purpose of the future exploration of an optimal arrangement of VAWT rotors which can increase the total power of a wind farm. Therefore, this study basically adopted the potential-flow-based method proposed by Whittlesey et al. (2010), which can predict the flow field around VAWT rotors in a short time. To express the wake flow behind VAWT rotors precisely, a new wake model was proposed, which mimics the flow field created by the computational fluid dynamics (CFD). In the CFD analysis of this study, the Dynamic Fluid / Body Interaction (DFBI) model that can change the rotational speed of VAWT rotors according to the flow condition was applied to simulate the realized power of each rotor. In this study, the unsteady incompressible Reynolds averaged Navier-Stokes (RANS) equations were solved and the unsteady flow field was averaged to give the flow field equivalent to that was simulated by the present model. The averaged flow field data were utilized to obtain the wake function representing velocity deficit.

The proposed wake model was based on the super-Gaussian function proposed by Shapiro et al. (2019), which can reproduce the wake profile transformation from a top-hat shape to the Gaussian shape. This study modified the super-Gaussian function to include the

acceleration regions and wake shift which are observed in the wake of a VAWT. The modified wake model was named ultra-super-Gaussian function. The fitting parameters to mimic the CFD results were determined for an isolated single rotor, which was assumed to be a small two-dimensional rotor equivalent to the cross section of an experimental rotor used in the wind tunnel tests conducted by Jodai et al. (2021). Although Whittlesey et al. (2010) did not consider the modification of the *y*-component of the flow velocity, this study modified the cross-flow component (*y*-component) to mimic the details of the flow field in accordance with CFD. As the correction functions of the *y*-component, the four Gaussian-type functions and the four resonant-type functions were introduced and the fitting parameters were also determined to mimic the CFD profiles.

The proposed wake model introduced the Biot-Savart law to mimic the flow behavior caused by the circulations of the rotors and to improve the variations in the wake shift and the width owing to the interaction between the rotors.

This study proposed a new method to predict the appropriate flow filed and rotor powers using the conservation of *x*-direction momentum in a control volume (CV). In this method, for a given combination of the circulations of rotors, the flow field around the VAWT cluster and the net momentum change in the *x*-direction was calculated using the boundary flow states. The thrust force and the net pressure force (or pressure loss) of each rotor were calculated using the relations obtained by CFD of an isolated single rotor. The pressure loss was modified by introducing the interaction functions which indicates the strength of the superposition of the wakes of a selected paired rotors according the layouts: co-rotating

(CO)-like, counter-down (CD)-like, counter-up (CU)-like, and tandem (TD)-like. Therefore, the present method needed the CFD simulations of four specific paired rotors in the CO, CD, CU, and TD layouts in addition to the CFD of an isolated single rotor. The present momentum balance method calculated all the combinations (i.e., round robin) of circulations of rotors in the given searching ranges. After the sub-searching processes, a combination of circulations which gave the minimum difference between the momentum change and the total net force was obtained as the final result. Since there is a possibility to yield a false result if the searching range is not adequate, this study proposed a procedure to limit the searching range according to the layout of other rotors enclosing a rotor at issue in the calculation process.

The proposed method was applied to the prediction of the wind-direction dependence of the power of paired rotors in the co-rotating (CO) and inverse-rotating (IR) configurations and was compared with the CFD analysis. Although the results in the case of the short inter-rotor gap ($0.5D$) suggested the necessity to improve the interaction functions, the results in the case of the inter-rotor gap longer than $1.0D$ showed the proposed method successfully worked. The prediction of the wind-direction dependence of the power of three-rotor clusters in the CO and IR configurations was carried out and showed the good agreements in trend of the averaged power distribution between the present model and CFD. The application to the four-rotor clusters in line at the parallel or tandem layouts did not give satisfactory results in quantity but showed the same tendency of the rotor powers for both layouts.

Although further improvements are necessary, this study proposed a method to predict the flow field and the rotor powers of a VAWT cluster in incomparably shorter time than the CFD with the DFBI model.

5.2 Recommendations

The first recommendation for the improvement is to increase the accuracy of the interaction model to simulate the flow distribution in the wake of a rotor pair in both *x*- and *y*-direction. Second, the interaction function I_j should be improved to be able to predict the outputs at different gaps better. Third, further improvements in the limiting of the searching range of circulation are necessary. To apply this method to the problem of finding the optimal layout of rotors in a VAWT wind farm, it is inevitable to introduce other optimization method such as the genetic algorithm (GA) instead of the round robin.

Achievements

Journal Publication:

Buranarote J., Hara Y., Furukawa M. and Jodai Y., Method to predict outputs of two-dimensional VAWT rotors by using wake model mimicking the CFD-created flow field, Energies 2022, 15, 5200.

International Conference:

Buranarote, J.; Hara, Y.; Jodai, Y.; Furukawa, M. A wake model simulating the velocity profile of a two-dimensional vertical axis wind turbine. In Proceedings of the 7th International Conference on Jets, Wakes and Separated Flows, ICJWSF–2022, Tokyo, Japan, 15–17 March 2022.

National Conference:

Buranarote, J.; Hara, Y.; Jodai, Y. Proposal of a model simulating the velocity profile of the wake of a two-dimensional vertical axis wind turbine. In Proceedings of the JSFM Annual General Meeting, Yamaguchi, Japan, 18–20 September 2020.

Buranarote, J.; Hara, Y.; Jodai, Y. Construction of a model simulating exactly the velocity profile around a two-dimensional vertical axis wind turbine. In Proceedings of the JSME 59th Chugoku-Shikoku Branch Meeting, Okayama, Japan, 5 March 2021.

Acknowledgments

I would like to sincerely thank the most important person for the success regarding my Ph.D., my supervisor, Professor Yutaka Hara. He guided me from the very beginning starting with recommending relevant research, coding from scratch, giving tips for research presentations, helping me with research writing including English conversations, and many more.

I would like to thank the Thai government for the scholarship and Kasetsart University for giving me this opportunity to study as well as I would like thank all my colleagues at the Faculty of Engineering Sriracha for all the advice, concern, and encouragement.

I would like to thank my first supervisor at Tottori University, Professor Takeharu Sakai. He was the first person who accepted me to study Ph.D. and recommend this particular research that is suitable for me.

I would like to thank Professor Masaru Furukawa and Professor Yoshifumi Jodai for the useful advice, checks, and recommendations and their valuable contribution to this research.

This research was supported by JSPS KAKENHI Grant Number JP 18K05013, the International Platform for Dryland Research and Education (IPDRE), Tottori University, and the 2021 Special Joint Project of the Faculty of Engineering, Tottori University. I would like to express my cordial gratitude to them.

I would like to thank the Advanced Mechanical and Electronic System Research Center (AMES) for supporting the article processing charge.

I would like to thank Professor Ryoji Waka for his advice on living in Japan, introducing a good kindergarten for my daughter, teaching Japanese to my wife, and recommending places to visit in Tottori.

I would like to thank all the staff of the International Affairs Division (IAD) for support, and for the advice on important documents and activities that proved to be very useful for living in Japan.

I would like to thank Mr.Tomoyuki Okinaga for helping me with the CFD simulation.

Thanks to all our fellow renewable energy lab members from 2019 to the present for their friendship and assistance.

Gratitude to my family members for being with me all throughout my living in Japan. Thank you, mom and sister, for everything. Thanks to all my relatives and friends, in Thailand.